Advances in Meteorology

Aerosol and Trace Gas Monitoring for Climate Change Studies

Lead Guest Editor: Salman Tariq
Guest Editors: Selahattin Incecik, Anu Heikkilä, Zia ul-Haq, and María Aránzazu Revuelta

Aerosol and Trace Gas Monitoring for Climate Change Studies

Advances in Meteorology

Aerosol and Trace Gas Monitoring for Climate Change Studies

Lead Guest Editor: Salman Tariq
Guest Editors: Selahattin Incecik, Anu Heikkilä, Zia ul-Haq, and María Aránzazu Revuelta

Contents

Hindawi
Advances in Meteorology
Volume 2020, Article ID 3691421, 10 pages
https://doi.org/10.1155/2020/3691421

Research Article

Potential Evapotranspiration Reduction and Its Influence on Crop Yield in the North China Plain in 1961–2014

Wanlin Dong,[1,2] **Chao Li**,[3] **Qi Hu**,[4] **Feifei Pan**,[5] **Jyoti Bhandari**,[2] **and Zhigang Sun**[2,6]

[1]*China Meteorological Administration Training Centre, Beijing 100081, China*
[2]*Key Laboratory of Ecosystem Network Observation and Modeling, Institute of Geographic Sciences and Natural Resources Research, Chinese Academy of Sciences, Beijing 100101, China*
[3]*Mentougou Meteorological Service, Beijing 102308, China*
[4]*College of Resources and Environmental Sciences, China Agricultural University, Beijing 100193, China*
[5]*Department of Geography, University of North Texas, Denton, TX 76203, USA*
[6]*College of Resources and Environment, University of Chinese Academy of Sciences, Beijing 100190, China*

Correspondence should be addressed to Zhigang Sun; sun.zhigang@igsnrr.ac.cn

Received 10 June 2019; Accepted 23 December 2019; Published 16 March 2020

Guest Editor: Salman Tariq

Climate change has caused uneven changes in hydrological processes (precipitation and evapotranspiration) on a space-temporal scale, which would influence climate types, eventually impact agricultural production. Based on data from 61 meteorological stations from 1961 to 2014 in the North China Plain (NCP), the spatiotemporal characteristics of climate variables, such as humidity index, precipitation, and potential evapotranspiration (ET_0), were analyzed. The sensitivity coefficients and contribution rates were applied to ET_0. The NCP has experienced a semiarid to humid climate from north to south due to the significant decline of ET_0 (−13.8 mm decade^{-1}). In the study region, 71.0% of the sites showed a "pan evaporation paradox" phenomenon. Relative humidity had the most negative influence on ET_0, while wind speed, sunshine hours, and air temperature had a positive effect on ET_0. Wind speed and sunshine hours contributed the most to the spatiotemporal variation of ET_0, followed by relative humidity and air temperature. Overall, the key climate factor impacting ET_0 was wind speed decline in the NCP, particularly in Beijing and Tianjin. The crop yield in Shandong and Henan provinces was higher than that in the other regions with a higher humidity index. The lower the humidity index in Hebei province, the lower the crop yield. Therefore, potential water shortages and water conflict should be considered in the future because of spatiotemporal humidity variations in the NCP.

1. Introduction

Hydrological processes and crop water requirements have been modified by climate change on local, regional, and global scales [1, 2]. The modification of climate change has coincided with surface air temperature increase.

In the hydrological cycle, actual evapotranspiration (ET) and potential evapotranspiration (ET_0) played important roles [3], particularly in soil evaporation and crop transpiration, eventually impact crop productivity. ET is measured as the quantity of water evaporating from an area under existing atmospheric conditions [4]. ET is controlled by two processes occurring simultaneously: evaporation from the soil and transpiration from the leaf surface [5]. ET_0 is calculated as the maximum quantity of water that can be lost as water vapor in a given climate, by a continuous, extensive stretch of vegetation covering the ground when there is no shortage of water [6]. ET_0 is determined by the meteorological conditions and the surface type [7]. Because ET_0 is computed from precipitation, temperature, relative humidity, wind speed, and sunshine hours [8–10], any change in these variables is likely to change the ET_0. Furthermore, these changes created more benign or stressful conditions for ET_0 [11, 12]. ET_0 had a significant impact on the availability of water resources [13], consequently influencing agricultural productivity. Plant growth planning

often requires information on ET_0 [14, 15] to estimate crop transpiration. Therefore, the study of ET_0 under climate change has become an interesting research issue to scientists around the world. Also, it is important to identify the changes in ET_0 on a regional scale.

The humidity index (K), change in precipitation, and ET_0 were applied to estimate dry-wet variations. Previous research studies on climate type only considered the influence of temperature and precipitation [16, 17] without including the influence of relative humidity, solar radiation, wind speed, and sunshine hours. Therefore, to understand the changing characteristics of climate variations, it is important to integrate water resource management. Furthermore, K can be applied to predict model scenarios that would persist in critical agricultural areas. Therefore, assessing ET_0 and K distribution would explain the relationships between climate change and hydrological processes. This would lead to reasonable water regulation and management to maintain the ecohydrological system.

In the NCP, summer maize (*Zea mays* L.) represents 33% of the national grain yield, while winter wheat represents 50% of the national grain yield [18]. Increasing temperature and decreasing precipitation are likely to reduce the yields of several primary crops over the next two decades [19]. Water shortage would be aggravated in the main grain production belt of North China [20, 21]. Bergamaschi et al. [22] indicated that crop yields would reduce by 10–20% up to 2050 because of warming and drying. Hence, understanding the hydrological distribution in these regions is critical for managing agricultural water resources and adjusting the planting pattern.

At present, there are few studies on the spatiotemporal variations in climate type by integrating the input (precipitation) and output (evapotranspiration) of atmospheric water vapor in the NCP. Therefore, the objectives of this study were to (1) quantify the changes in spatial and temporal variations in ET_0 and K in the NCP from 1961 to 2014, (2) quantitatively explain the reasons for the changes in ET_0 by analyzing the sensitivity coefficients and contribution rates, and (3) analyse the relationship between ET_0 and the crop yield. The results might be useful to agricultural planning and layout.

2. Materials and Methods

2.1. Study Area and Data. The study area, located in the NCP (31–43°N and 110–123°E), has a warm, temperate monsoon climate. The precipitation changes significantly in summer. The main crops are summer maize and winter wheat. The mean annual temperature and average annual precipitation were 13.0°C and 586 mm, respectively [23]. The soil has a silt-loam texture in the cultivated layer in general. This study was based in Beijing, Tianjin, Hebei province, Henan province, and Shandong province.

In this study, daily meteorological data from January 1961 to December 2014 were obtained from 60 stations in the NCP (Table 1). These data contained daily mean, minimum and maximum temperature, sunshine hours, wind speed, precipitation, and relative humidity provided by the National Climatic Centre of China Meteorological Administration (http://cdc.cma.gov.cn). The wind speed at 10 m height was converted to wind speed at 2 m height using the wind profile relationship introduced in Allen et al. [24], as shown in equation (1). The observed dataset has been subjected to strict quality and homogenization control. The geographical location of the stations is shown in Figure 1.

$$u_2 = u_z \frac{4.87}{\mathrm{In}\,(67.8z - 5.42)}, \tag{1}$$

where u_2 is the wind speed at 2 m above the ground surface ($\mathrm{m{\cdot}s^{-1}}$), u_z is the wind speed at z m above the surface ($\mathrm{m{\cdot}s^{-1}}$), and z is the height of measurement above the ground surface (m).

2.2. Data Analyses

2.2.1. Estimation of Humidity Index (K). Humidity index is the ratio of precipitation to potential evapotranspiration and is calculated by

$$K = \frac{P}{\mathrm{ET}_0}, \tag{2}$$

where P is the daily precipitation ($\mathrm{mm{\cdot}d^{-1}}$) and ET_0 is the daily potential evapotranspiration ($\mathrm{mm{\cdot}d^{-1}}$). The classification of climate region based on humidity index is listed in Table 2 [25].

ET_0 is calculated by the Penman–Monteith formula [24]:

$$\mathrm{ET}_0 = \frac{0.408\left(R_n - \mathrm{G}\right) + \gamma 900/T + 273U_2\left(e_s - \mathrm{e_a}\right)}{\Delta + \gamma\left(1 + 0.34U_2\right)}, \tag{3}$$

where R_n is the net radiation at the surface, $\mathrm{MJ{\cdot}m^{-2}{\cdot}d^{-1}}$, G is soil heat flux density, $\mathrm{MJ{\cdot}m^{-2}{\cdot}d^{-1}}$, $\gamma$is the psychrometric constant, kPa $^\circ\mathrm{C}^{-1}$, T is the mean daily air temperature, °C, U_2 is the wind speed at a height of 2 m, $\mathrm{m{\cdot}s^{-1}}$, e_s is the saturation vapor pressure, kPa, e_a is the actual vapor pressure, kPa, and Δ is the slope of the saturated water-vapor pressure curve, kPa $^\circ\mathrm{C}^{-1}$. The computation of all data required for calculating ET_0 followed the method and procedure given in Chapter 3 of FAO-56 [24].

2.2.2. Sensitivity Analysis and Sensitivity Coefficient. Sensitivity analysis of the ET_0 equation is an effective way to analyze the effect of meteorological factors on ET_0 [26]. Previous studies showed the usage of nondimensional relative sensitivity coefficients to explain climate variables influence on ET_0 [27]:

$$S_{V_i} = \lim_{\Delta V_i \longrightarrow 0} = \left(\frac{\left(\Delta \mathrm{ET}_0/\mathrm{ET}_0\right)}{\left(\Delta V_i/V\right)}\right) = \frac{\partial \mathrm{ET}_0}{\partial V_i}\frac{V_i}{\mathrm{ET}_0}, \tag{4}$$

where S_{Vi} is the sensitivity coefficient of the ith climate variable, ET_0 is the potential evapotranspiration, $\mathrm{mm{\cdot}d^{-1}}$, ΔET_0 is the daily change of ET_0, V_i is the ith climate variable, and ΔV_i is the change of V_i. A positive/negative S_{Vi} of a variable indicated that ET_0 would increase/decrease as climate variables. The greater the S_{Vi}, the greater effect of the climate factor on ET_0.

Table 1: Geographic characteristic information of each meteorological station in the study.

No.	Province	Site	Latitude (°)	Longitude (°)	Elevation (m)
1	Beijing	Huairou	40.72	116.55	487.9
2		Miyun	40.38	116.87	71.8
3		Beijing	39.80	116.47	31.3
4	Hebei	Zhangbei	41.15	114.70	1393.3
5		Weixian	39.83	114.57	909.5
6		Shijiazhuang	38.03	114.42	81.0
7		Xingtai	37.07	114.50	77.3
8		Fengning	41.22	116.63	661.2
9		Weichang	41.93	117.75	842.8
10		Zhangjiakou	40.78	114.88	724.2
11		Huailai	40.40	115.50	536.8
12		Chengde	40.98	117.95	385.9
13		Zunhua	40.20	117.95	54.9
14		Qinglong	40.40	118.95	227.5
15		Qinhuangdao	39.85	119.52	2.4
16		Langfang	39.12	116.38	9.0
17		Tangshan	39.67	118.15	27.8
18		Leting	39.43	118.88	10.5
19		Baoding	38.85	115.52	17.2
20		Raoyang	38.23	115.73	19.0
21		Huanghua	38.37	117.35	6.6
22		Nangong	37.37	115.38	27.4
23	Henan	Anyang	36.05	114.40	62.9
24		Xinxiang	35.32	113.88	73.2
25		Sanmengxia	34.80	111.20	409.9
26		Lushi	34.05	111.03	568.8
27		Mengjin	34.82	112.43	333.3
28		Luanchuang	33.78	111.60	750.3
29		Zhengzhou	34.72	113.65	110.4
30		Xuchang	34.03	113.87	66.8
31		Kaifeng	34.78	114.30	73.7
32		Xixia	33.30	111.50	250.3
33		Nanyang	33.03	112.58	129.2
34		Baofeng	33.88	113.05	136.4
35		Xihua	33.78	114.52	52.6
36		Nanyang	32.61	113.67	153.0
37		Zhumadian	33.00	114.02	82.7
38		Xinyang	32.13	114.05	114.5
39		Shangqiu	34.45	115.67	50.1
40		Gushi	32.17	115.62	42.9
41	Shandong	Huiminxian	37.48	117.53	11.7
42		Gaoqing	37.12	117.88	122.3
43		Changdao	37.93	120.72	39.7
44		Longkou	37.62	120.32	4.8
45		Chengshantou	37.40	122.68	47.7
46		Chaoyang	36.23	115.67	37.8
47		Jinan	36.60	117.05	170.3
48		Qiyuan	36.18	118.15	305.1
49		Yantai	37.23	120.49	48.6
50		Weifang	36.75	119.18	22.2
51		Qingdao	36.07	120.33	76.0
52		Haiyang	36.77	121.18	40.9
53		Gunzhou	35.57	116.85	51.7
54		Feixian	35.25	117.95	121.2
55		Juxian	35.58	118.83	107.4
56		Rizhao	35.43	119.53	36.9
57		Linyi	34.96	118.51	36.2
58	Tianjin	Jixian	40.17	117.45	5.1
59		Tianjin	39.08	117.07	2.5
60		Tanggu	39.05	117.72	4.8

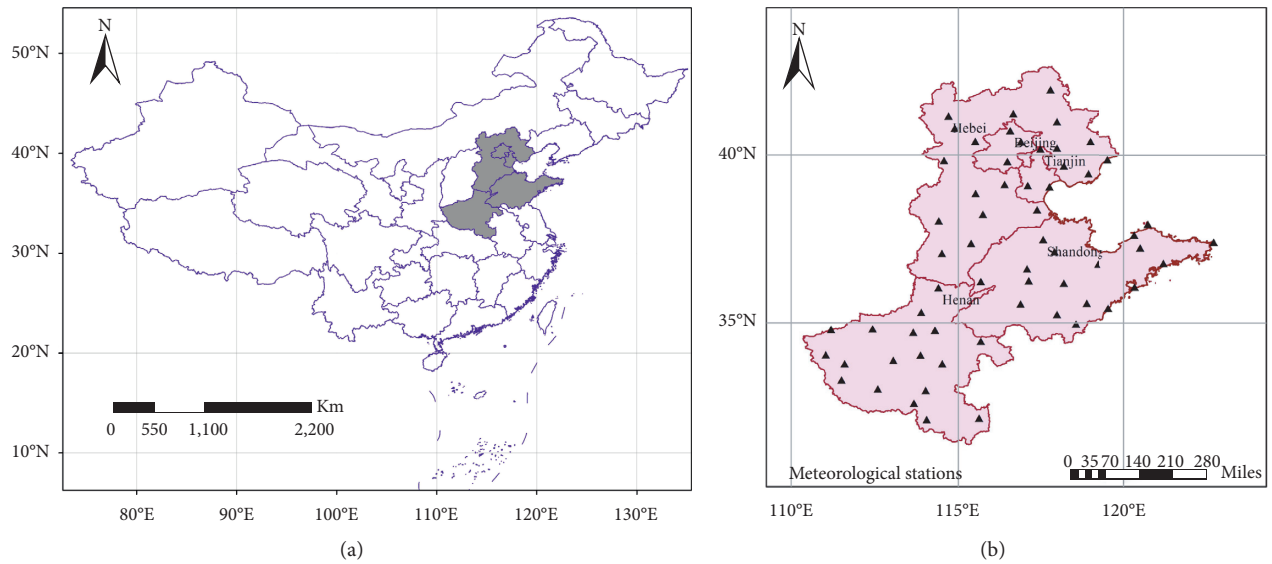

Figure 1: Distribution of meteorological stations in China (a) and the study area (b).

Table 2: Humidity index (K).

Humidity index	Climate region
$K < 0.03$	Extremely arid climate region
$0.03K < 0.2$	Arid climate region
$0.2K < 0.5$	Semiarid climate region
$0.5K < 1.0$	Semihumid climate region
$K > 1.0$	Humid climate region

2.2.3. Calculation of Attribution Rate. The attribution rate G_{vi} is used to link the climate variable to ET_0:

$$G_{vi} = S_{vi} \times R_{vi}, \tag{5}$$

where G_{vi} is the contribution of the ith climate variable to ET_0, S_{vi} is the sensitivity coefficient, and R_{vi} is the relative change rate for the ith climate variation, which was given by equation (5). The meaning of G_{vi} is the same as S_{vi}.

In this study, S_{vi} and G_{vi} for daily air temperature, solar radiation, relative humidity, and wind speed were estimated to quantify the contribution of each factor to the variation of ET_0.

$$R_{Vi} = \frac{\Delta Vi}{\overline{V}i} = \frac{n \times \text{Trend}_{Vi}}{\overline{V}i}, \tag{6}$$

where Trend_{Vi} is the climate tendency rate for the ith climate variation and is calculated by equation (6), $\overline{V_i}$ is the mean value for the climate variation, and n is the time in years. In this study, $n = 54$.

2.2.4. Climate Trend. Climate tendency rate (Trend_{Vi}) was calculated by the least square method:

$$X_i = at + b, \quad (t = 1, 2, 3 \ldots n), \tag{7}$$

where X_i is the ith climate variation, t is the time in years, a is the regression coefficient, $10{\times}a$ is the climate tendency rate, and b is the constant parameter.

3. Results

3.1. Annual and Spatial Variation and Tendency of Humidity Index. The humidity index (K) showed an upward trend from north to south, changing from 0.34 to 1.20 (Figure 2(a)), which indicated that the climate of the region varied from semiarid to humid from north to south. The climate in Northwest and mid-west Hebei was semiarid, while that in South Henan was humid, with K above 1. The other regions had semihumid climate, with K ranging from 0.5 to 1.0.

The tendency rate of K was -0.005 decade^{-1} ($P = 0.63$), which showed a slight drying trend from south to north (Figure 2(b)). Thirty-five percent of the sites (total = 60) mainly distributed in southern NCP had a tendency rate of K above 0, which indicated that these regions were wet. The other sites with a tendency rate of K below 0, especially East Shandong and North Hebei, were dry with a tendency rate of K below -0.01 decade^{-1}.

3.2. Interdecadal Changes in Precipitation and ET_0. The tendency rate of precipitation was -12.4 mm decade^{-1}, which indicated a downward trend of precipitation. The abrupt decline in precipitation tendency rate was mainly observed in Southeast Hebei and Southeast Shandong (Figure 3(a)). Only 10.0% of all the sites had a tendency rate of precipitation over 0.

The ET_0 tendency rate was -13.5 mm decade^{-1} (Figure 3(b)), which showed a downward trend from 1961 to 2014. The ET_0 tendency rate was significant at the 0.05 level in 71.0% of the sites, especially in mid-east Hebei and mid-south Shandong.

3.3. Sensitivity Coefficient of Temperature (S_T), Relative Humidity (S_{RH}), Sunshine Hours (S_{SH}), and Wind Speed (S_{WS}) to ET_0 on Annual and Spatial Scales. S_T varied from 0 to 0.15

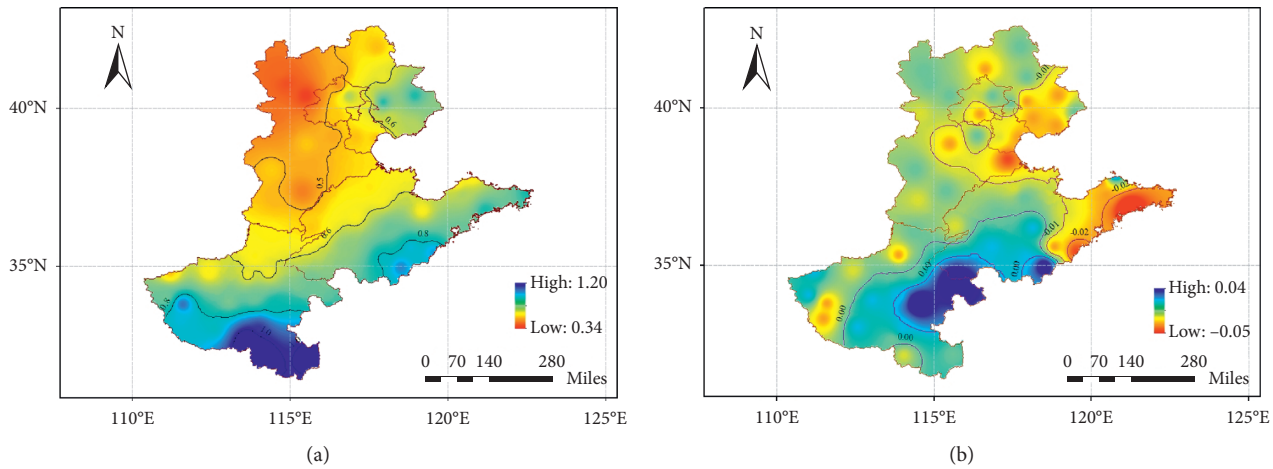

Figure 2: Spatial distribution of humidity index (a) and the tendency rate of humidity index (b) from 1961 to 2014.

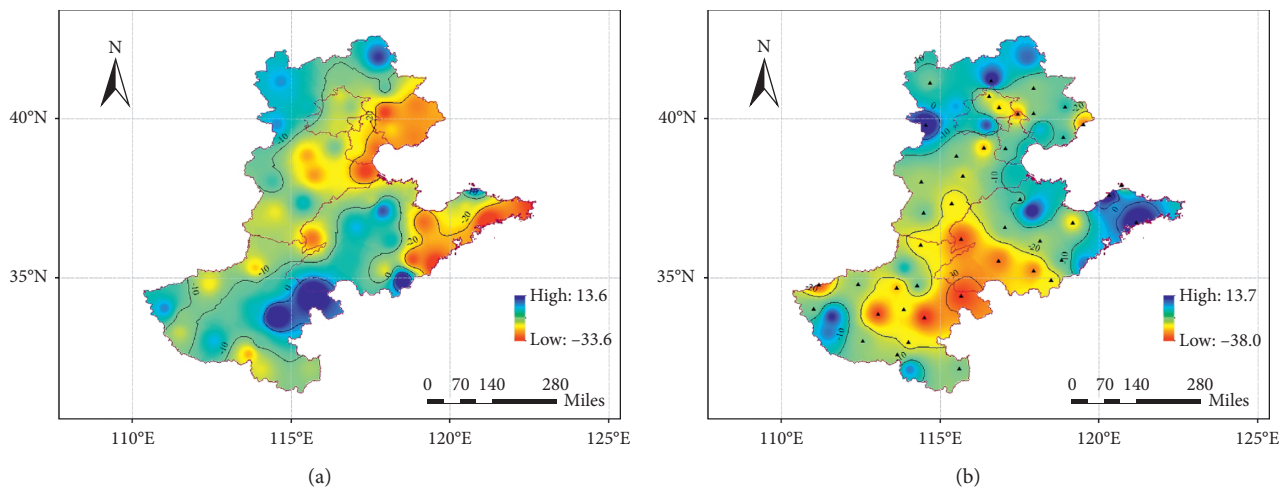

Figure 3: Spatial distribution of precipitation (a) and ET_0 (b) tendency rate from 1961 to 2014.

(Figure 4(a)), which meant that ET_0 increased with temperature. S_T in the southeast was higher, especially in the Henan province, while it peaked in the mid-region, such as North Shandong, Beijing, Tianjin, and North Hebei. S_{RH} varied from−0.70 to−0.19 (Figure 4(b)), which indicated that ET_0 decreased as the relative humidity increased. The spatial distribution of S_{RH} showed a downward trend from south to east. The S_{RH} was higher in East Shandong, with an absolute value above 0.5. In South Hebei and Beijing, the absolute value of S_{RH} was below 0.4. The S_{SH} in all regions was above 0, with a mean value of 0.18 (Figure 4(c)). The S_{SH} showed an upward trend from north to south. S_{WS} ranged from 0.10 to 0.31 (Figure 4(d)) and showed a downward trend from north to south. The S_{WS} in the northern part of the region, e.g., North Hebei, Beijing, and Tianjin, was above 0.21, while in South Henan, it was below 0.18.

3.4. Climate Factor Attribution Rate to ET_0 on Annual and Spatial Scales. G_{vi} was applied in this study to indicate the relative change in ET_0 resulting from each meteorological factor. The attribution rate of air temperature to ET_0 (G_{vT}) ranged from−0.5% to 4.0% (Figure 5(a)). G_{vT} in the northern and eastern parts of the NCP was over 1%, while it was less than 1% in the other regions. The attribution rate of relative humidity to ET_0 (G_{vRH}) ranged from−4.7% to 10.1% (Figure 5(b)). G_{vRH} in North Hebei and Southwest Shangdong was below 0. The attribution rate of sunshine hours to ET_0 (G_{vSH}) ranged from−8.4% to 0.2% (Figure 5(c)). G_{vSH} was above 0 in only one site. The spatial distribution of G_{vSH} showed a downward trend from north to south. The attribution rate of wind speed to ET_0 (G_{vWS}) ranged from−19.1% to 4.9% (Figure 5(d)). The highest absolute value of G_{vWS} was in Beijing and Tianjin.

The attribution rate of air temperature and relative humidity to ET_0 was positive, which indicated that ET_0 increased with an increase in these two climate factors. However, the mechanisms of G_{vT} and G_{vRH} were different. G_{vT} was positive when the sensitivity coefficient was positive and the tendency rate (0.24°C decade^{-1}) of air temperature increased (Figure 6(a)). G_{vRH} was positive when the sensitivity coefficient was negative and the tendency rate

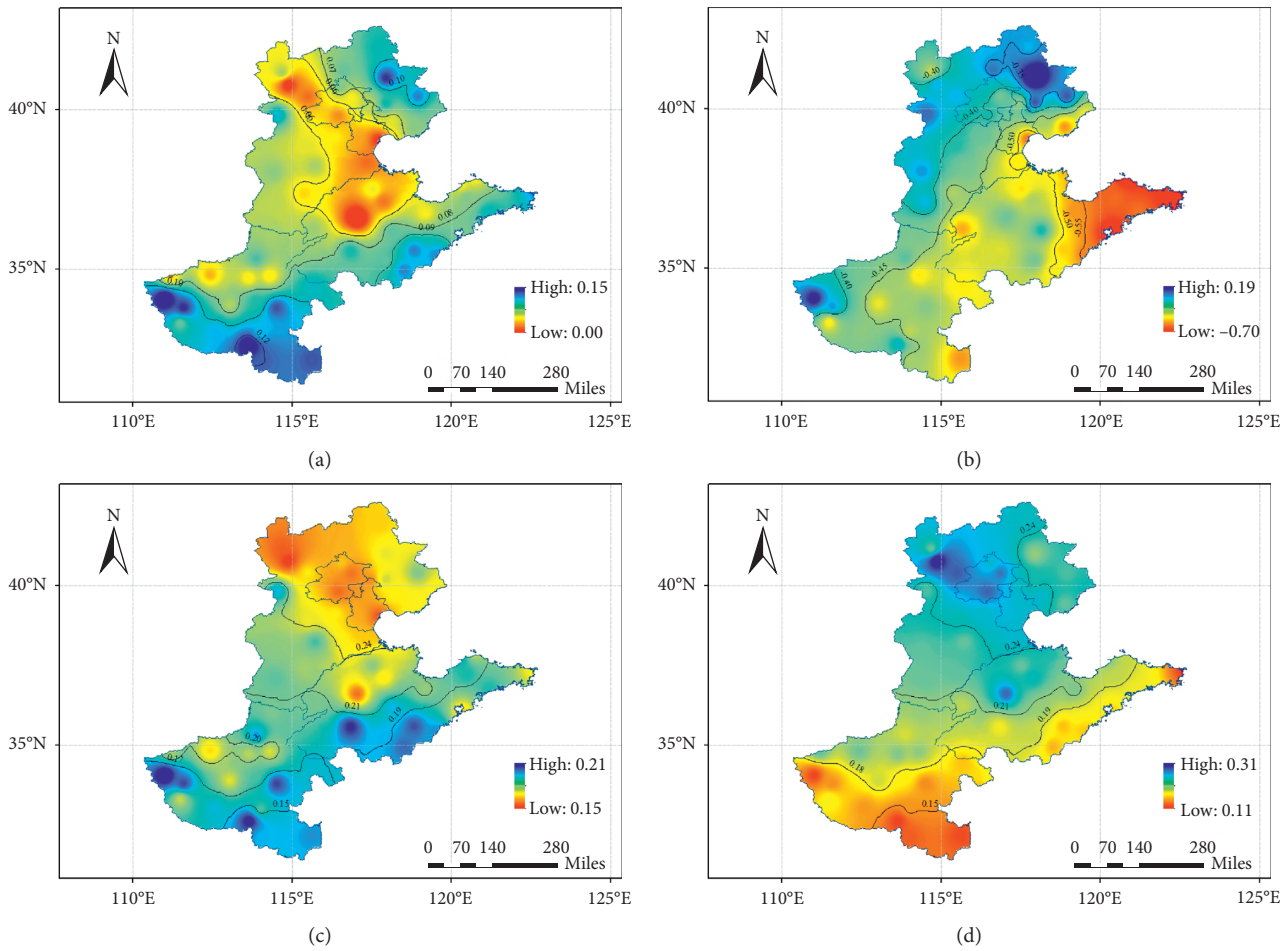

Figure 4: Spatial distribution of sensitivity coefficient of the main meteorological factors affecting ET_0 from 1961 to 2014. (a) Temperature. (b) Relative humidity. (c) Sunshine hours. (d) Wind speed.

(0.44 decade^{-1}) of relative humidity decreased (Figure 6(c)). The attribution rate of sunshine hours and wind speed was negative, which indicated that the change in the two climate factors decreased ET_0. The attribution rate of climate factor to ET_0 was in the following order: wind speed > sunshine hour > relative humidity > air temperature.

4. Discussion

The change in climate types was due to the sensitivity to various meteorological variables and their attribution to ET_0 in the NCP. ET_0 was most sensitive to relative humidity, which had a negative effect. This was consistent with the study by Hu et al. [28] in Northeast China. The factor that impacted ET_0 significantly varied depending on the location. Huo et al. [3] indicated that ET_0 was very sensitive to 2 m wind speed and relative humidity in Northwest China. In southern Spain, ET_0 was sensitive to air temperature and radiation in the warmer season and to 2 m wind speed in cooler seasons [29]. In Australia, temperature was found to be the most important factor for ET_0, but the second-most important factors differed between dry and humid catchments [30]. Yang et al. [31] showed that the sensitivity of ET_0 to climate factors varied from low elevations to high elevations. The sensitivity of ET_0 to climate factors is regional variation because climate conditions and climate factors differ with regional variation [30, 31]. In this study, wind speed reduction was the main reason for the decline in ET_0 from 1961 to 2014. However, the climate tendency rate was low and resulted in a relatively low attribution rate.

In general, warm climates led to an increase in evaporation and evapotranspiration. However, the observation of pan evaporation rate has been declined in most parts of the world in the past several decades [8, 9, 32, 33], which is called the pan evaporation paradox phenomenon [34]. Also, those only considered the influence of air temperature on ET_0, without considering other meteorological factors, e.g., wind speed, relative humidity, and sunshine hours. It revealed significant increasing trends in ET_0 ($P = 0.1$) during 1961–1990 over the entire West African region [35]. Although the air temperature significantly increased at the rate of 0.24°C decade^{-1}, the effect of decrease in wind speed and sunshine hours was greater than that of the increase in air temperature, which led to a significant decline of ET_0 in the NCP. This pattern of variations is in agreement with the findings of Dinpashoh et al. [36] in North-West Iran where most of the stations selected (86% of the sites) also showed increasing trends in ET_0 between 1997 and 2016. However, Hou et al. [37] revealed that temperature was the key variable

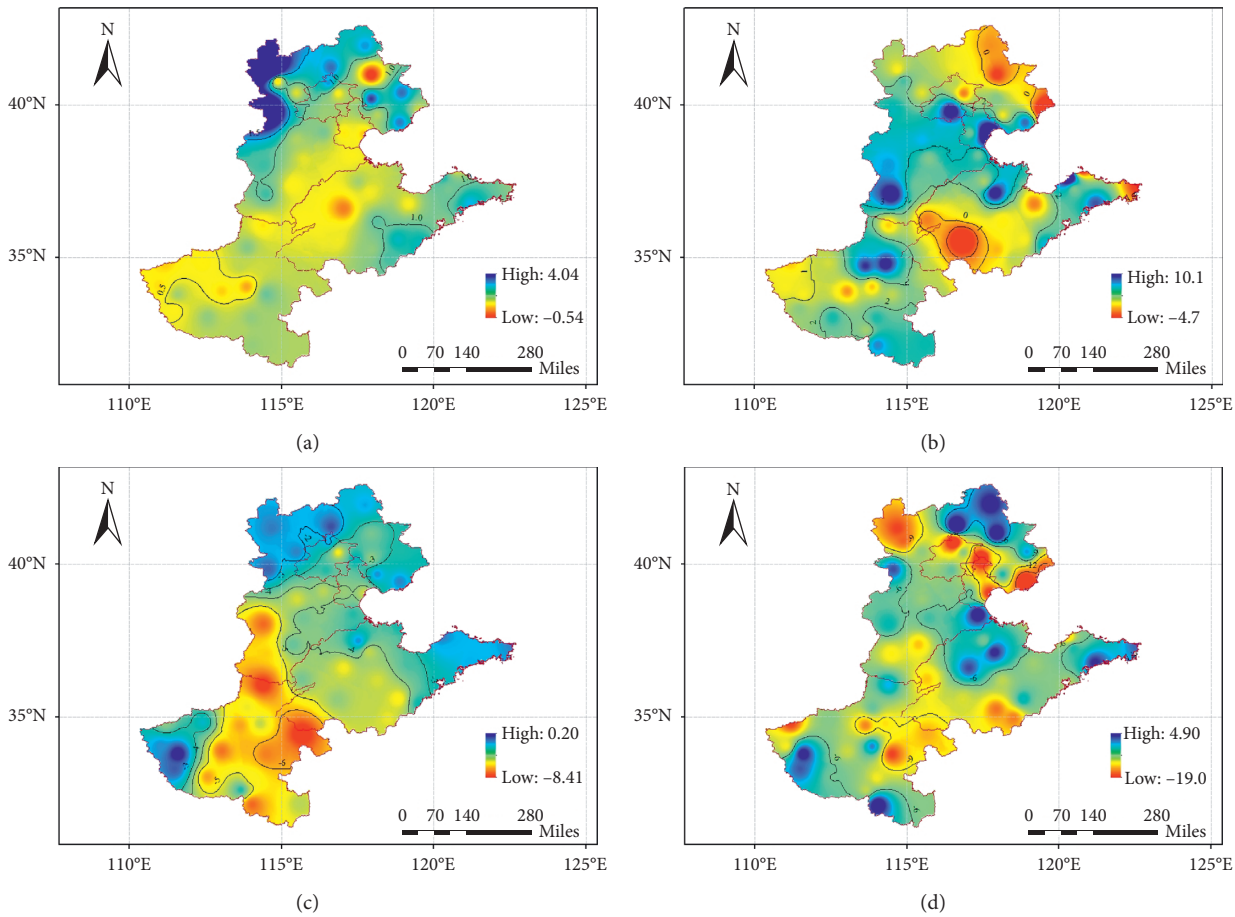

Figure 5: Spatial distribution of attribution rate to ET_0 of the main meteorological elements from 1961 to 2014. (a) Temperature. (b) Relative humidity. (c) Sunshine hours. (d) Wind speed.

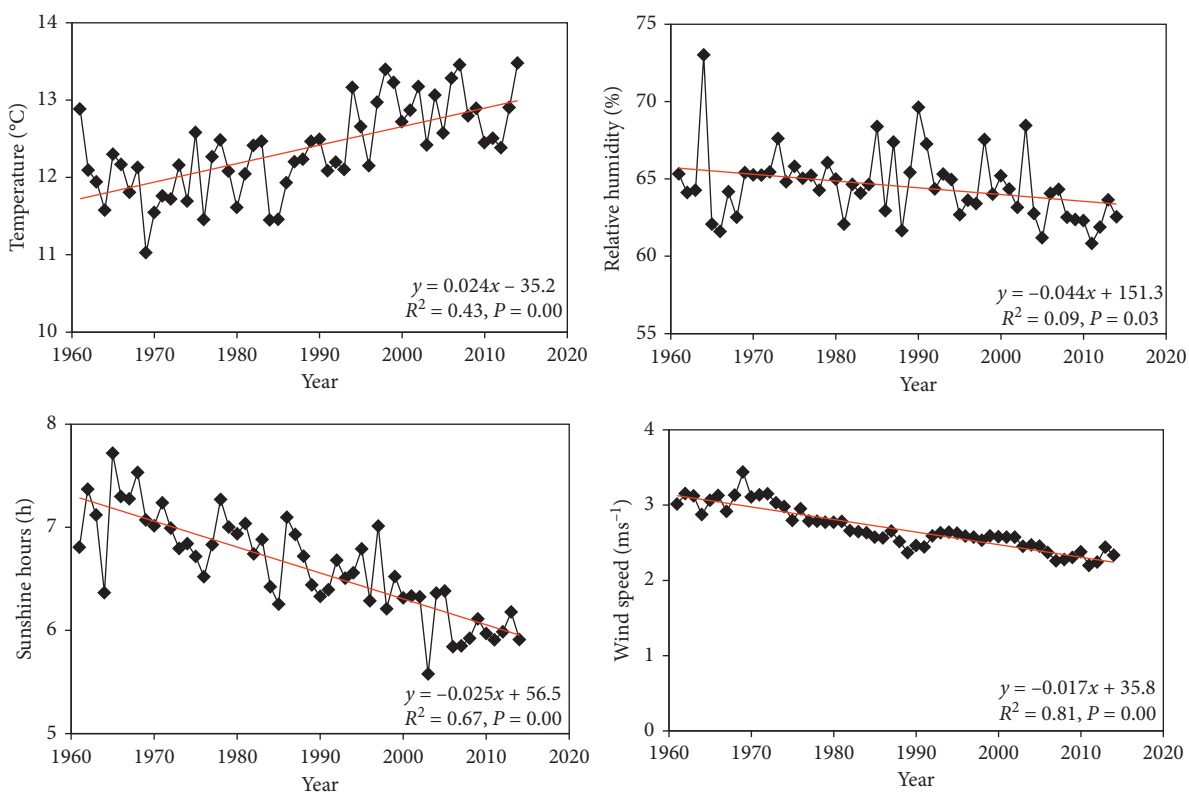

Figure 6: Tendency rate of temperature (a), relative humidity (b), sunshine hours (c), and wind speed (d) from 1961 to 2014 in the NCP.

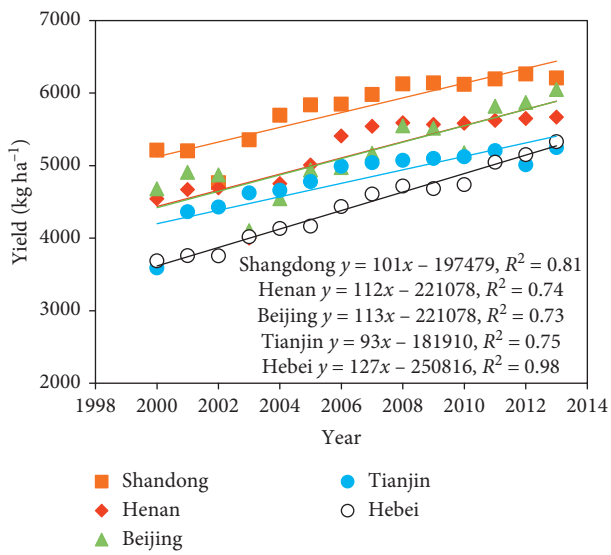

Figure 7: Crop yield from 2000 to 2013.

Table 3: The annual humidity index (K) from 1961 to 2014 in each region.

Sites	Shandong	Henan	Beijing	Tianjin	Hebei
K-value	0.70	0.77	0.54	0.54	0.53

contributing to increasing ET_0 due to its sensitivity to ET_0 and the significant increase trend.

Agriculture accounts for at least 90% of the total water use in the arid and semiarid regions [38]. An important way to alleviate water stress is to improve agricultural water management. Comprehensively understanding an agro-hydrological process lays a foundation for minimizing agricultural water use. In the presence of a shallow water table, groundwater provides an important source for crop water use in arid and semiarid regions [39, 40], which impact crop productive. Climate type depended on the rate of change of precipitation and ET_0. The important issue involves the evaluation of drought impacts on agriculture. Crop yields and drought occurrence statistics are closely related [42, 42], but consistency analysis of drought trends derived from humidity index and agricultural drought survey is sparse. Crop yield increased significantly ($P \leq 0.001$) in the study area (Figure 7), in accordance with K in each area. The crop yield was greater in Shandong and Henan province, with a K of 0.70 and 0.77, compared with that in Tianjin, Beijing, and Hebei (Table 3). The lowest K (0.53) was in Hebei province, along with the lowest crop yield. Therefore, regional water balance should be considered and drought or flood risk might be reduced in these areas. China has investigated agricultural drought area for decades, so it is important to investigate the degree that K and ET_0 with agricultural drought surveys, especially in their climatic trends.

5. Conclusions

The NCP has experienced a semiarid to humid climate from north to south based on the humidity index due to the slight change in precipitation and the significant decline of ET_0 on annual and spatial scales. In the study region, 71.0% of the sites showed a "pan evaporation paradox" phenomenon. ET_0 was the most sensitive to relative humidity, particularly in East Shandong, followed by wind speed. The dominant cause of ET_0 decline was wind speed, with the highest attribution rates, particularly in Beijing and Tianjin. The higher the humidity index in Shandong and Henan province was, the higher the crop yield was. The lower the humidity index in Hebei province was, the lower the crop yield was. It is necessary to analyze the influence of ET_0 on crop yield at various crop growth stages.

Data Availability

The data used to support the findings of this study have been deposited in the 3691421data-2019.xls repository and are included within the article.

Disclosure

The first author is Wanlin Dong.

Conflicts of Interest

The authors declare that there are no conflicts of interest regarding the publication of this paper.

Acknowledgments

This research was supported by The National Key Research and Development Program of China (2017YFC0503805 and 2017YFD0300304).

References

[1] IPCC, *Climate Change 2013: The Physical Science Basis. Contribution of Working Group I to the Fifth Assessment Report of the Intergovernmental Panel on Climate Change*, Cambridge University Press, Cambridge, UK, 2013.

[2] Q. Zhang, C. Xu, and Z. Zhang, "Observed changes of drought/wetness episodes in the Pearl River basin, China, using the standardized precipitation index and aridity index," *Theoretical and Applied Climatology*, vol. 98, no. 1-2, pp. 89–99, 2009.

[3] Z. Huo, X. Dai, S. Feng, S. Kang, and G. Huang, "Effect of climate change on reference evapotranspiration and aridity index in arid region of China," *Journal of Hydrology*, vol. 492, pp. 24–34, 2013.

[4] H. L. Penman, "Natural evaporation from open water, bare soil and grass," *Proceedings of the Royal Society of London. Series A. Mathematical and Physical Sciences*, vol. 193, pp. 120–145, 1948.

[5] N. Chattopadhyay and M. Hulme, "Evaporation and potential evapotranspiration in India under conditions of recent and future climate change," *Agricultural and Forest Meteorology*, vol. 87, no. 1, pp. 55–73, 1997.

[6] M. Gangopadhyay, V. A. Uryvaev, M. H. Oman, T. J. Nordenson, and G. E. Harbeck, *Measurement and Estimation of Evaporation and Evapotranspiration*, P. Govinda Rao, Ed., World Meteorological Organization, Geneva, Switzerland, 1966.

[7] J.-P. Lhomme, "Towards a rational definition of potential evaporation," *Hydrology and Earth System Sciences*, vol. 1, no. 2, pp. 257–264, 1997.

[8] S. Irmak, I. Kabenge, K. E. Skaggs, and D. Mutiibwa, "Trend and magnitude of changes in climate variables and reference evapotranspiration over 116-yr period in the Platte River Basin, central Nebraska-USA," *Journal of Hydrology*, vol. 420-421, pp. 228–244, 2012.

[9] T. C. Peterson, V. S. Golubev, and P. Y. Groisman, "Evaporation losing its strength," *Nature*, vol. 377, no. 6551, pp. 687-688, 1995.

[10] S. Sun, H. Chen, G. Wang et al., "Shift in potential evapotranspiration and its implications for dryness/wetness over Southwest China," *Journal of Geophysical Research: Atmospheres*, vol. 121, no. 16, pp. 9342–9355, 2016.

[11] S. Lavergne, N. Mouquet, W. Thuiller, and O. Ronce, "Biodiversity and climate change: integrating evolutionary and ecological responses of species and communities," *Annual Review of Ecology, Evolution, and Systematics*, vol. 41, no. 1, pp. 321–350, 2010.

[12] K. E. McCluney, J. Belnap, S. L. Collins et al., "Shifting species interactions in terrestrial dryland ecosystems under altered water availability and climate change," *Biological Reviews*, vol. 87, no. 3, pp. 563–582, 2012.

[13] K. Zhang, S. Pan, W. Zhang et al., "Influence of climate change on reference evapotranspiration and aridity index and their temporal-spatial variations in the Yellow River Basin, China, from 1961 to 2012," *Quaternary International*, vol. 380-381, pp. 75–82, 2015.

[14] J. Doorenbos, *Guidelines For Predicting Crop Water Requirements*, FAO Irrigation Drainage, Rome, Italy, 1977.

[15] W. Shuttleworth and J. Wallace, "Calculating the water requirements of irrigated crops in Australia using the Matt-Shuttleworth approach," *Transactions of the ASABE*, vol. 52, no. 6, pp. 1895–1906, 2009.

[16] P. Frich, L. V. Alexander, P. Della-Marta et al., "Observed coherent changes in climatic extremes during the second half of the twentieth century," *Climate Research*, vol. 19, pp. 193–212, 2002.

[17] Z. Li, Y. He, C. Wang et al., "Changes of daily climate extremes in southwestern China during 1961-2008," *Global and Planetary Change*, vol. 80-81, pp. 255–272, 2012.

[18] Z. Li, Z. Ouyang, X. Liu, and C. Hu, "Scientific basic for constructing the "Bohai Sea Grannry"-demands, potential and approaches," *Chinese Science Bulletin*, vol. 26, pp. 371–374, 2011.

[19] D. B. Lobell, M. B. Burke, C. Tebaldi, M. D. Mastrandrea, W. P. Falcon, and R. L. Naylor, "Prioritizing climate change adaptation needs for food security in 2030," *Science*, vol. 319, no. 5863, pp. 607–610, 2008.

[20] F. Tao, M. Yokozawa, Y. Hayashi, and E. Lin, "Future climate change, the agricultural water cycle, and agricultural production in China," *Agriculture, Ecosystems & Environment*, vol. 95, no. 1, pp. 203–215, 2003.

[21] F. Tao and Z. Zhang, "Climate change, wheat productivity and water use in the North China Plain: A new super-ensemble-based probabilistic projection, wheat productivity and water use in the North China Plain: a new super-ensemble-based probabilistic projection," *Agricultural and Forest Meteorology*, vol. 170, pp. 146–165, 2013.

[22] H. Bergamaschi, G. A. Dalmago, J. I. Bergonci et al., "Distribuição hídrica no período crítico do milho e produção de grãos," *Pesquisa Agropecuária Brasileira*, vol. 39, no. 9, pp. 831–839, 2004.

[23] G. Yan, Z. Yao, X. Zheng, and C. Liu, "Characteristics of annual nitrous and nitric oxide emissions from major cereal crops in the North China Plain under alternative fertilizer management," *Agriculture, Ecosystems & Environment*, vol. 207, pp. 67–78, 2015.

[24] R. G. Allen, L. S. Pereira, D. Raes, and M. Smith, *Crop Evapotranspiration Guidelines for Computing Crop Water Requirements*, FAO Irrigation and Drainage, Rome, Italy, 1998.

[25] S. Shen, F. Zhang, and Q. Sheng, "Spatio-temporal changes of wetness index in China from 1975 to 2004," *Transactions of the CSAE*, vol. 25, pp. 11–15, 2009, In Chinese.

[26] L. Gong, C. Xu, D. Chen, S. Halldin, and Y. D. Chen, "Sensitivity of the Penman-Monteith reference evapotranspiration to key climatic variables in the Changjiang (Yangtze River) basin," *Journal of Hydrology*, vol. 329, no. 3-4, pp. 620–629, 2006.

[27] K. Beven, "A sensitivity analysis of the Penman-Monteith actual evapotranspiration estimates," *Journal of Hydrology*, vol. 44, no. 3-4, pp. 169–190, 1979.

[28] Q. Hu, F. Pan, X. Pan et al., "Dry-wet variations and cause analysis in Northeast China at multi-time scales," *Theoretical and Applied Climatology*, vol. 133, p. 775, 2016.

[29] J. Estévez, P. Gavilán, and J. Berengena, "Sensitivity analysis of a Penman-Monteith type equation to estimate reference evapotranspiration in southern Spain," *Hydrological Processes*, vol. 23, no. 23, pp. 3342–3353, 2009.

[30] D. Guo, S. Westra, and H. R. Maier, "Sensitivity of potential evapotranspiration to changes in climate variables for different Australian climatic zones," *Hydrology and Earth System Sciences*, vol. 21, no. 4, pp. 2107–2126, 2017.

[31] Y. Yang, R. Chen, Y. Song, C. Han, J. Liu, and Z. Liu, "Sensitivity of potential evapotranspiration to meteorological factors and their elevational gradients in the Qilian Mountains, Northwestern China," *Journal of Hydrology*, vol. 568, pp. 147–159, 2019.

[32] H. Tabari and P. Hosseinzadeh Talaee, "Sensitivity of evapotranspiration to climatic change in different climates," *Global and Planetary Change*, vol. 115, pp. 16–23, 2014.

[33] M. Garcia, D. Raes, R. Allen, and C. Herbas, "Dynamics of reference evapotranspiration in the Bolivian highlands

(Altiplano)," *Agricultural and Forest Meteorology*, vol. 125, no. 1-2, pp. 67–82, 2004.

[34] L. R. Michael and D. F. Graham, "Changes in Australian pan evaporation from 1970 to 2002," *International Journal of Climatology*, vol. 24, pp. 1077–1090, 2004.

[35] M. L. Roderick and G. D. Farquhar, "The cause of decreased pan evaporation over the past 50 years," *Science*, vol. 298, no. 298, pp. 1410–1, 2002.

[36] O. E. Abiye, O. J. Matthew, L. A. Sunmonu, and O. A. Babatunde, "Potential evapotranspiration trends in West Africa from 1906 to 2015," *SN Applied Sciences*, vol. 1, pp. 1434–1456, 2019.

[37] Y. Dinpashoh, S. Jahanbakhsh-Asl, A. A. Rasouli, M. Foroughi, and V. P. Singh, "Impact of climate change on potential evapotranspiration (case study: west and NW of Iran)," *Theoretical and Applied Climatology*, vol. 136, no. 1-2, pp. 185–201, 2019.

[38] L. Hou, B. X. Hu, H. Li, and L. Wan, "Potential impacts of climate variation on potato field evapotranspiration: field experiment and numerical simulation of potato water use in an arid site," *Journal of Geophysical Research: Atmospheres*, vol. 123, no. 18, pp. 202–10, 2018.

[39] N. Whittlesey, "Improving irrigation efficiency through technology adoption: when will it conserve water?" *Developments in Water Science*, vol. 50, no. 3, pp. 53–62, 2003.

[40] S. Satchithanantham, V. Krahn, R. Sri Ranjan, and S. Sager, "Shallow groundwater uptake and irrigation water redistribution within the potato root zone," *Agricultural Water Management*, vol. 132, pp. 101–110, 2014.

[41] Y. Zhou, J. Wenninger, Z. Yang et al., "Groundwater– surface water interactions, vegetation dependencies and implications for water resources management in the semi-arid Hailiutu River catchment, China – a synthesis," *Hydrology and Earth System Sciences*, vol. 17, no. 7, pp. 2435–2447, 2013.

[42] C. Yu, C. Li, Q. Xin et al., "Dynamic assessment of the impact of drought on agricultural yield and scale-dependent return periods over large geographic regions," *Environmental Modelling and Software*, vol. 62, pp. 454–464, 2014.

[43] M. Mkhabela, P. Bullock, M. Gervais, G. Finlay, and H. Sapirstein, "Assessing indicators of agricultural drought impacts on spring wheat yield and quality on the Canadian prairies," *Agricultural and Forest Meteorology*, vol. 150, no. 3, pp. 399–410, 2010.

Hindawi
Advances in Meteorology
Volume 2020, Article ID 4361570, 10 pages
https://doi.org/10.1155/2020/4361570

Research Article

The Spatiotemporal Evolution Pattern and Influential Factor of Regional Carbon Emission Convergence in China

Xin Tong [1,2]

[1]*School of Business Administration, Northeastern University, Shenyang 110819, China*
[2]*Central University of Finance and Economics, School of Economics, Beijing 100081, China*

Correspondence should be addressed to Xin Tong; angel.tongtong@163.com

Received 16 May 2019; Revised 3 December 2019; Accepted 16 January 2020; Published 14 February 2020

Guest Editor: Salman Tariq

As economic development rapidly progresses in China, a method of carbon emission control that provides reasonable solutions is needed. This paper analyzes the convergence of carbon emission evolutionary characteristics in different regions of China and studies the dynamics of carbon emissions in China based on a convergence model. It was found that the carbon emission levels of each region are prominent in terms of time, and the regional carbon emission level has absolute β characteristics. The regional carbon emission condition β convergences have different convergence paths. Therefore, it is necessary to justify carbon emission reduction in China and put forward an emission reduction strategy.

1. Introduction

Ecological civilization is a millennium-scale plan in the report of the Nineteenth National Congress of the Communist Party of China. It can be seen that China takes an active part in global environmental governance and the responsibility of building a community in the future. In many negotiations on climate change, the research on climate change justice mainly focuses on the equity of carbon emissions in developed and developing countries. The responsibility and obligation to solve carbon emissions are considered the most important issues, while the research on the justice of carbon emissions within countries and regions is less emphasized. This paper discusses the spatial convergence of regisonal carbon emissions in order to achieve regional emission reductions and achieve overall green, sustainable development in China.

With the rapid development of the economy, an increasing number of people have begun to realize that climate change and environmental pollution is emerging on a large scale, forcing people to pay attention to economic and carbon emissions. Convergence refers to the degree of the reduction of the abandonment but also to approaching and examining a value [1]. The convergence hypothesis provides strong theoretical support for backward regions to catch up with developed regions and to lay a foundation for the neoclassical economic growth theory. Convergence mainly includes delta convergence, beta convergence, and club convergence, and beta convergence is divided into absolute beta convergence and conditional beta convergence [2]. Absolute beta convergence refers to the negative correlation between the economic growth rate and the initial level. Conditional beta convergence means that regional convergence is affected not only by the initial level of development but also by other factors [3]. Regional carbon emissions will also be different because of the different economic and geographical conditions of different regions. The convergence theory of economic growth was introduced to test the convergence of regional carbon emissions, which can be used to explore the driving factors of regional carbon emission convergence, and help us understand whether the regional carbon emission reduction goals are fair and reasonable.

With continuous development at an economic level, the upgrading of the industrial structure, improvement at the technological level, and the enhancement of environmental responsibility consciousness, regional carbon emissions will converge in theory. At present, the scope of convergence

theory is gradually expanding many fields, but there is a lack of systematic research on carbon emissions and social responsibility from the perspective of spatial justice. Based on the basic idea of the economic convergence hypothesis in neoclassical growth theory, this paper systematically analyzes the convergence of regional carbon emissions and social responsibility in China from the perspective of spatial justice.

2. Theoretical Basis and Research Hypothesis

Against the background of global warming, the process of China's economic development is at a critical stage in history, and each region is developing at a relatively fast speed in history. People realize that we must change the traditional, simple development mode, which only pays attention to benefits. In the process of economic development, attention should be paid not only to economic growth but also to the impact of economic development on the environment so as to reduce the carbon emissions from nonrenewable energy consumption and thus reduce the impact on climate change. However, in order to reduce carbon emissions in China, it is necessary to understand the mechanism of different factors on the convergence of carbon emissions. Different regional economic development has different characteristics. How can the principle of spatial justice be realized? Only by clarifying these key issues can we find corresponding policy measures and an emission reduction path to reduce carbon emissions, alleviate the pressure of carbon emissions people are facing, and promote China as a large developing country that can achieve low-carbon sustainable development.

In order to achieve the overall sustainable development of the low-carbon economy in China, it is necessary to further analyze the influencing factors of regional carbon emissions in China, find out the internal mechanism of regional carbon emissions change, and lay a solid theoretical foundation for the realization of China's carbon emission reduction. Regional carbon emissions involve different aspects; thus, to determine the influencing factors of regional carbon emissions, this paper explores these factors from different perspectives of resource consumption in the context of economic development.

Domestic scholars began to study carbon emissions at the beginning of the 21st century and have mostly applied the research methods of foreign scholars to analyze China's energy consumption and carbon emissions in the light of China's development situation. Existing research methods on carbon emissions mainly adopt decomposition research methods. Wang and other scholars used the Laplace index decomposition method to decompose carbon emission factors into population, energy consumption intensity, and energy consumption factors for analysis [4]. Wu and other scholars used the logarithmic mean decomposition method to decompose and analyze the influencing factors of per capita carbon emissions. The empirical results show that optimizing the energy consumption structure, optimizing the industrial structure, and optimizing energy efficiency are all important factors in reducing carbon dioxide emissions [5]. Other scholars have used the decomposition analysis method to study the influence factors of carbon emissions in different cities [6, 7]. Zhao and Li used the logarithmic mean decomposition method to analyze the data of per capita carbon emissions and per capita GDP in China. The study found that per capita GDP increase was the main driving factor of per capita carbon emissions increase [8]. Fan and Ruiling used the logarithmic mean factor decomposition method to analyze the factors affecting carbon dioxide emissions in China's industry. The results show that economic activity and energy intensity are the two most important factors affecting carbon emissions in the chemical industry [9]. Some scholars quantitatively analyzed the impact of factors on carbon emissions in different stages of Xinjiang by using Dean's logarithmic average method. The results show that economic growth is the main factor contributing to the increase of carbon emissions [10]. Wang and other senior students used the structural decomposition analysis model to analyze the problem of residents' consumption carbon emissions [11]. The study found that the president of China's carbon emissions are an upward trend, which was determined by the economy and the amount of consumption. However, analysis from the impact dimension showed that the national residents' consumption still adhered to the path of low-carbon development.

Another major research method is the Kaya identity research method proposed by Kaya, a famous foreign scholar. According to Kaya identity, He and Zhang constructed a decomposition model of influencing factors of carbon emissions in the iron and steel industry and used the cointegration method to explore the equilibrium relationship between carbon emissions and influencing factors [12]. Zhu et al. based on the Kaya identity study found that the main driving force of China's carbon emission increase is economic expansion [13]. Li and other scholars used panel data to analyze the relationship between carbon dioxide emissions and population, economy, and technology in different regions. The results show that there are obvious differences in carbon dioxide emissions in different regions. The elasticity coefficients of carbon dioxide emissions with respect to the population, economy, and technology in different regions are different. Rapid economic growth is the most important driving factor for the increase of carbon dioxide emissions in different regions [14]. Wei and other scholars analyzed the mechanism of carbon emissions from the perspectives of economic growth, energy consumption, and development. The results show that in the long run, fossil energy consumption has the strongest effect on carbon emissions and financial development has a negative correlation. In the short run, economic growth and financial development, energy consumption and carbon emissions, and financial development and carbon emissions show a one-way Granger causality [15]. Zhu and other scholars used the extended STIRPAT model to measure and analyze the impact of population and technology on carbon emissions by the ridge regression method [16]. The results show that the extended STIRPAT model has a high explanatory power to China's national conditions, and the consumption level of residents, the urbanization rate of the population, and

population size are the main factors affecting the total carbon emissions in China. The explanatory power of technological progress factors with respect to China's emissions at this stage is limited, so China's potential to reduce carbon emissions through technological progress in the future is huge.

Other studies have been carried out by Weber and other scholars based on the input-output model to study the different impacts of carbon emissions [17, 18]. Li and other scholars based on static and dynamic panel models have found that international trade increases China's carbon dioxide emissions and the intensity of carbon emissions and has a serious negative impact on the environment [19]. Birdsall and other scholars believe that the increase in population will lead to an increase in energy consumption, resulting in relatively large carbon emissions, and an increase in population will also increase the destruction of the ecological environment [20]. Knapp and other scholars believe that population is the main driving force of global carbon emissions, while global population growth is also an important reason for the rapid increase in global carbon emissions [21].

Among the existing domestic and foreign scholars' research on the convergence of carbon emissions, foreign scholars mainly use the Gini coefficient and other research methods to test the convergence of carbon emissions. Romero and other scholars used the random convergence test method to analyze the convergence of carbon emissions beta [22]. Ezcurra analyzed the convergence of transnational carbon emissions and found that the difference of per capita carbon emissions was decreasing [23]. Gao and other scholars used the quantile method to analyze the reasons for the convergence of carbon emissions in 28 provinces in China and found that there are absolute convergence and conditional convergence between provinces [24]. Yang and other scholars tested the stochastic convergence of carbon dioxide in China and found that there was no global convergence trend [25]. Shao and other scholars analyzed the convergence of carbon emissions in different regions of China and different industries and found that the convergence paths of carbon emissions in different regions were different [26, 27]. Zhang systematically studied the convergence of carbon emission intensity in China and found that China's carbon emission intensity had significant absolute convergence, conditional convergence, and club convergence characteristics [28]. Although the existing research has an important reference value for revealing the relationship between the dynamic changes of carbon emissions and the influencing factors, the existing research on the convergence of carbon emissions does not take into account the role of spatial effects and needs to combine spatial justice to deeply analyze the convergence of carbon emissions and to explore the mechanism of the various influencing factors on carbon emissions synergistically to solve the problem of carbon emissions. Therefore, from the perspective of spatial justice, this paper systematically explores the impact of different factors on regional unit carbon emissions. The index system includes different aspects of regional unit economic development; thus, the mechanism of different factors on regional carbon emission convergence is systematically analyzed.

Population is the basis and main body of social production activities. However, different levels of economic development, different conditions of social development, and different processes of population development lead to a different understanding and reflection of population phenomena. Because of different regional development conditions, the mechanism of the population's role in carbon emissions is different.

Economic development is an index to measure the scale and speed of national and regional economic development, as well as a criterion for the stage and potential of economic development. It is usually used to reflect the level of development of a country or regional economy by such indicators as national income, economic development speed, gross national product, per capita national income, and economic growth speed. Economic development requires a large amount of energy input. Energy consumption may lead to the generation of pollutants and the increase of carbon emissions at the same time. However, with the development of the economy, people's consumption concept has changed so as to improve energy efficiency and accelerate the reduction of carbon emissions.

Technological progress is generally reflected in innovation activities. Patent data, as a measure of innovation, is the main indicator of technological progress in existing literature. This paper also uses the number of patents instead of the technical level index to measure the level of technological progress and development. Technological progress can not only directly reduce energy consumption and carbon emissions but also improve the level of environmental pollution control through technological progress, thereby improving the environmental situation.

Industrial structure refers to the distribution of production factors among different industrial sectors. Adjustment of industrial structure can reduce primary energy consumption and reduce carbon emissions. The higher proportion of secondary industries in China is the main reason for greater energy efficiency consumption and rising carbon emissions. Upgrading and optimizing industrial structure will improve the intensity of energy consumption and reduce the growth rate of carbon emissions.

At present, with the rapid development of China's finance, the role of the environment has been strengthened. As an indirect factor affecting carbon emissions, financial development indicators can adjust the investment intentions of enterprises. However, there is no consensus on the role of financial development in the convergence of carbon emissions. It is assumed that different regions actively adopt adjusting financial policies to adjust economic sustainable development. Therefore, entry into development can promote the convergence of carbon emissions.

As a policy factor affecting energy consumption, energy price can affect people's energy consumption and consequently the change of carbon emissions. Governments often adopt administrative and economic policies to intervene and regulate. In China's environmental policy, energy price is the main adjustment policy. Through a one-time energy price

rise and new energy policy subsidies, people's awareness of environmental protection is raised, and people are encouraged to consciously save energy, use environmental protection energy, and reduce pollutant emissions.

International trade generally includes export trading and import trading. As a world factory, China generally believes that international trade will aggravate the rise of carbon emissions in China. International trade plays a dual role in economic growth and other dependent variables. At the same time, international trade promotes economic growth, which also enables developing countries to have more funds to deal with environmental problems, introduce advanced equipment and technology, improve energy efficiency and clean energy utilization, and reduce environmental pollution such as carbon emissions.

The level of urbanization development is a major factor affecting carbon emissions. The impact of urbanization on the environment can be considered from different aspects. Population urbanization, through the improvement of people's awareness and changes in living habits, may encourage the population to produce fewer carbon emissions. The better living conditions in cities may also reduce the total energy consumption and reduce carbon emissions.

Fiscal decentralization can reflect the financial autonomy of local governments. Generally speaking, the higher the degree of fiscal decentralization, the greater the autonomy. The government does not need to adjust its behavior according to the incentive direction of the central government. However, existing studies at home and abroad suggest that fiscal decentralization has different impacts on regional carbon emissions.

3. Research Design

3.1. Data Collection. This paper studies the sample data of 30 provinces in China, and there are no official statistical data on carbon emissions. This article uses an IPCC calculation formula to determine carbon emissions. The formula is as follows:

$$C_{it} = \sum_{j=1}^{n} \left(E_{ijt} \times E_j \times EF_j \right), \tag{1}$$

where C_{it} is the total carbon emissions in the t-th year of the i-th province; ($i = 1, \ldots, 30$, $t = 2000, \ldots, 2015$); E_{ijt} is the total energy consumption of the j-th energy source in the t-th year of the i-th province; E_j is the converted standard coal coefficient of the j-th energy source; and EF_j is the carbon emission coefficient of the jth energy source.

Since all energy consumption in the China Energy Statistical Yearbook is represented as a physical quantity, this article first uses the China Energy Statistics Year based on the determination of the number of standard coals. One kilogram of raw coal is converted into 0.7143 kg of standard coal, natural gas is converted to 1.3300 kg of standard coal, and crude oil is converted to 1.4286 kg of standard coal. Energy consumption is converted into standard coal. The two energy sources recommended by the US Department of Energy (DOE)/EIA have a carbon emission coefficient of 0.702 for coal, 0.478 for oil, and 0.389 for natural gas. The carbon emissions of different energy sources are calculated based on the carbon emission coefficients of different energy sources. The data do not include carbon emissions data for Hong Kong, Macau, Taiwan, and Tibet. There is a small error with the total carbon emissions measured via the Carbon Dioxide Information Analysis Center of the Oak Ridge National Laboratory, which provides important reference values. Data regarding population, economic growth, industrial structure, financial development, energy price, international trade, urbanization rate, and fiscal decentralization come from the China Statistical Yearbook. Technological progress data come from the China Statistical Yearbook on Science and Technology.

3.2. Variable Measurement. According to the calculation formula of carbon emissions, the regional carbon emissions in China were calculated.

The variables of population, economic growth, technological progress, industrial structure, financial development, energy price, international trade, urbanization rate, and fiscal decentralization were selected:

(1) Population (P): according to the needs of this study, the total population at the end of the year in all regions of China is used.

(2) Economic growth (A): GDP data were used to represent economic growth indicators.

(3) Technological progress (T): technological progress is mainly reflected in the activities of innovation. Referring to the literature of scholars at home and abroad, the patent authorization data were used as the evaluation index of technological progress.

(4) Industrial structure (S): carbon emissions in different industrial sectors are also different. Referencing relevant studies, the proportion of secondary industry GDP to total GDP was used.

(5) Financial development (F): financial development is an important index to measure the expansion and efficiency of the financial system. This paper uses the ratio of the loan balance of financial institutions to GDP so as to measure the degree of financial development.

(6) Energy price (E): as a factor affecting energy consumption, energy price mainly considers raw materials, fuel, and the power price index of each province, which replaces the energy price index.

(7) International trade (EX): the differences in resource endowment, industrial structure, and the international division of labor between countries in the world inevitably lead to the problem of carbon emission transfer in international trade. This paper uses export dependence to reflect the level of the development of export trade in international trade.

(8) Urbanization rate (U): urbanization level is an important factor affecting carbon emissions. Urbanization rate is represented by the ratio of urban population to total population.

(9) Fiscal decentralization (FD): fiscal decentralization, as an index reflecting the degree of fiscal freedom of the government, is also a factor affecting carbon emissions. Referring to the decentralization index of Zhang and other scholars, the proportion of provincial government expenditure to central fiscal expenditure is used.

3.3. Construction of the Empirical Model. There are a few studies on carbon emission convergence, but there are no detailed and in-depth studies on different regions. Therefore, it is necessary to do further research on the basis of existing research and consider the spatial factor, which will elaborate on China's carbon emission convergence model and sample study and will follow the methods of an existing paper [29].

3.3.1. Convergence Model of Carbon Emissions. The convergence of regional carbon emissions is generally expressed by the standard deviation index:

$$\sigma = \sqrt{\frac{1}{n-1}\sum_{i=1}^{n}\left(I - \frac{1}{n}\sum_{i=1}^{n} I_i\right)}. \quad (2)$$

Standard deviation indicates the degree of deviation in carbon emissions from the overall average level. I_i represents the average carbon emissions of region I, n is the number of regions, and the average carbon emissions of all regions i in the country are also represented.

3.3.2. Beta Convergence Model of Carbon Emissions. The beta convergence of carbon emissions can be divided into absolute beta convergence and conditional beta convergence. The absolute beta convergence of carbon emissions implies strict assumptions and preconditions; that is, each region has a similar level of economic development, technological strength, industrial structure, environmental policies, etc. Under the same conditions, carbon emission levels in different regions will have the same steady state and thus have the same growth path and stable state. The beta convergence of carbon emission conditions refers to a convergence mode corresponding to the absolute beta convergence of carbon emissions. The beta convergence of carbon emission conditions does not require the assumption that different regions of absolute beta convergence must have exactly the same "basic characteristics," which means that different regions have different growth paths and stable states. According to neoclassical growth theory, if there is a condition of beta convergence for regional carbon emissions, then each region will converge to its own stable state and have its own convergence path.

The expression of absolute beta convergence of regional carbon emissions is as follows:

$$\ln\frac{I_{i,i+T}/I_{i,t}}{T} = a + b\ln\left(I_{i,t}\right) + u_{i,t}, \quad (3)$$

where I_i and T represent the level of carbon emissions in the period t and I_i, $I+T$ represents the level of carbon emissions in the period $T+T$, $\ln(I_i, I+T/I_i, t)/T$ represents the average annual growth rate of carbon emissions from the period T to $t+T$, and $u_{i,t}$ is a random error term.

When $T=1$, the absolute beta convergence expression of regional carbon emissions is as follows:

$$\ln\left(\frac{I_{i,i+T}}{I_{i,t}}\right) = a + b\ln\left(I_{i,t}\right) + u_{i,t}. \quad (4)$$

On the basis of the absolute beta convergence model of regional carbon emissions, appropriate control variables are added. The expression of the beta convergence model of regional carbon emission conditions is as follows:

$$\ln\frac{I_{i,i+T}/I_{i,t}}{T} = a + b\ln\left(I_{i,t}\right) + \sum_{k=1}^{m}\lambda_k X_{k,i,t} + u_{i,t}, \quad (5)$$

where K denotes the regression coefficient of the k-th control variable and X_k, i, and t denote the k-th control variable. When the coefficient is negative and has passed the significance level test, the level of carbon emissions has a conditional beta convergence trend.

When $T=1$, the expression of beta convergence of regional carbon emission conditions is as follows:

$$\ln\left(I_{i,i+T}/I_{i,t}\right) = a + b\ln\left(I_{i,t}\right) + \sum_{k=1}^{m}\lambda_k X_{k,i,t} + u_{i,t}. \quad (6)$$

4. Empirical Analysis

4.1. Descriptive Statistics and Correlation Analysis. The descriptive statistical results of the influencing factors of carbon emissions in China are shown in Table 1.

4.2. Relevance Analysis of Carbon Emissions in China. Firstly, global Moran's I statistics were used to determine the correlation of carbon emissions, and the results are shown in Table 2.

According to Table 2, there is a significant positive spatial autocorrelation of carbon emissions in 30 provinces of China between 2000 and 2015. The Moran index of spatial statistics shows an overall growth trend, which proves that the carbon emissions of 30 provinces in China have obvious spatial autocorrelation. *OLS* estimation of a classical linear regression model may neglect the inappropriate model setting of spatial effects.

Opengeoda software was used to analyze the spatial autocorrelation of carbon emissions. The average carbon emissions of 30 provinces in China from 2000 to 2015 were analyzed.

According to the Moran scatter plot of the average carbon emissions (CA) from 2000 to 2015, we can know that

Table 1: Descriptive statistical results of carbon emission impact factors in China.

Variables	Sample number	Maximum	Minimum	Mean	Median	Standard deviation
Population	480	10849	517	4366	3814	2634.63
Economic growth	480	54246.16	263.68	9401	6444	9309.62
Technological progress	480	269944	70	181731	4831	38167.02
Industrial structure	480	61.5	19.7	46.94	48.5	7.66
Financial development	480	26.46	0.08	1.41	1.24	1.31
Energy prices	480	123.9	84.3	103.58	104.2	6.75
International trade	480	91.59	0.86	15.9	6.92	18.96
Urbanization rate	480	89.6	18.61	47.86	45.93	15.29
Fiscal decentralization	480	7.3	0.4	2.55	2.3	1.32

Table 2: Moran's I test results of provincial carbon emissions from 2000 to 2015.

Year	Moran's I
2000	0.3003
2001	0.3416
2002	0.3304
2003	0.2940
2004	0.3245
2005	0.3448
2006	0.3285
2007	0.3257
2008	0.3340
2009	0.3149
2010	0.3119
2011	0.3073
2012	0.2743
2013	0.2780
2014	0.2605
2015	0.2564

the average carbon emissions of provinces in China are mostly concentrated in the first and third quadrants. The low-carbon emission areas are surrounded by low-carbon emission areas, and the high-carbon emission areas are surrounded by high-carbon emissions areas, which proves that the carbon emissions of provinces in China have the characteristics of accumulation.

According to the Hausman test, the absolute convergence of carbon emissions is determined by a fixed effect model or a random effect model. The Hausman test results were 18.8496, which passed the 0.05% significance level test, so we rejected the original hypothesis that individual effects were independent of explanatory variables and adopted the fixed effect model. According to the results of the Wald and LR tests, Wald_spatial_lag and LR_spatial_lag are 2.8106 and −15.1237, respectively. Their adjoint probabilities are 0.0936 and 1, and Wald_spatial_error and LR_spatial_error are 2.3593 and −12.2571, respectively. The adjoint probabilities are 0.1245 and 1. This shows that the log-likelihood ($\log L$) and goodness-of-fit system of spatial_error and LR_spatial_error are not consistent with the original hypothesis. The AdjR^2 values are 462.3068 and 0.1564, respectively, which is relatively high. Therefore, we chose the results of the spatial lag panel model II to explain the overall results.

According to the Hausman test, either the fixed effect model or the stochastic effect model is used to judge the convergence of carbon emission conditions. The result of the Hausman test was 30.8883, which passed the 0.05% significance level test, so we rejected the original hypothesis that individual effects were independent of explanatory variables and adopted the fixed effect model. According to Wald_spatial_lag and LR_spatial_lag, which are, respectively, 17.5168 and −173.5749, their adjoint probability values are 0.00637 and 1. Wald_spatial_error and LR_spatial_error are 14.0841 and −650.3549, and their adjoint probabilities are 0.1692 and 1. This shows that without the original assumption, $\log L$ and AdjR^2 of the spatial lag panel model II are 476.5879 and 0.2254, which are relatively high, so we chose the spatial lag panel model II and the spatial Durbin model to explain the overall results.

4.3. σ Convergence Analysis of Regional Carbon Emissions in China. We calculate the convergence of every year, and n is 30. We can obtain the standard deviation in 2000 was 1961.5850, which rose to 6053.112 in 2015. This shows that there is no trend of convergence in China's interprovincial carbon emissions. The convergence rate of carbon emissions decreased in 2006, which may be related to the speed of economic development in China. The year 2006 is the first in the Eleventh Five-Year Plan. Industrialization and urbanization are also in the stage of accelerating development. The gross domestic product (GDP) has reached 20187.1 billion yuan, an increase of 11.1% per year, and the per capita GDP has increased by 19.9% per year. With the most complex year of China's economy being 2010, facing adjustment and change in the global economic development mode and governance structure, China's external environment presents a complex economic pattern. The central government resolutely launched the macropolicy control, which increased the standard deviation of carbon emissions in China. It can be seen that the State Council made some achievements in vigorously developing new industries such as energy conservation, environmental protection, new energy, new materials, and new generation information technology. However, on the whole, the standard deviation curve of regional carbon emissions in China has been on the rise, showing evolution characteristics in the overall divergence.

4.4. Absolute Beta Convergence Analysis of Regional Carbon Emissions in China. The absolute beta convergence of China's provincial carbon emissions was tested, and the results are shown in Table 3.

Table 3: Spatial econometric model estimate result.

Variable	Spatial lag panel model				Spatial Durbin panel model			
	No fixed effects I	Spatial fixed effects II	Time period fixed effects III	Spatial and time period fixed effects IV	No fixed effects I	Spatial fixed effects II	Time period fixed effects III	Spatial and time period fixed effects IV
C	0.2569 (0.0000)				0.2422 (0.0000)			
β	−0.0252 (0.0016)	−0.0747 (0.0000)	−0.0138 (0.0080)	−0.1292 (0.0000)	−0.0109 (0.0799)	−0.1125 (0.0000)	−0.0020 (0.7509)	−0.1383 (0.0000)
WLni					−0.0130 (0.0002)	0.0519 (0.0134)	−0.0109 (0.0007)	−0.0610 (0.1231)
ρ	0.3520 (0.0000)	0.3080 (0.0000)	−0.0550 (0.4245)	0.0321 (0.6289)	−0.0379 (0.0000)	0.3410 (0.0000)	−0.0220 (0.7476)	−0.0540 (0.4318)
Log L	412.8868	462.3068	451.4023	505.9498	462.3068	465.5667	457.6220	507.0783
AdjR^2	0.0637	0.1564	0.0170	0.0790	0.1928	0.1671	0.0428	0.0844

According to panel model II of the spatial lag in Table 3, it can be seen that the level of carbon emissions at the beginning of the period is inversely proportional to its growth rate, which proves that absolute beta convergence exists in China's regional carbon emissions, and that the convergence of carbon emissions between regions has a spatial spillover effect. The correlation coefficient is 0.3080, which passes the significant level test of 0.05%, and the level of carbon emissions in adjacent regions tends to converge steadily.

4.5. Beta Convergence Analysis of Regional Carbon Emission Conditions in China. To further test the existence of conditional beta convergence of regional carbon emissions, the influencing factors are added to the conditional convergence model of regional carbon emissions as control variables. Table 4 is a spatial model with the natural logarithm of carbon emissions as explanatory variables and the natural logarithm of population growth, urbanization rate, industrial structure, economic growth, energy price, and technological progress also as explanatory variables. As a result, the estimated coefficients of beta in Table 4 are all negative, which proves that beta convergence exists in China's carbon emissions. Technological progress and fiscal decentralization have passed the significance test on the coefficient of convergence of carbon emissions, but other factors have not passed this test, which proves that these factors are the reasons for the convergence of regional carbon emission conditions in China.

The results of the spatial lag panel model II and the spatial Durbin panel model with carbon emissions as explanatory variables were analyzed. It can be seen that the impact of population on carbon emissions passed the significance test, and some have not. This proves that China is still a developing country, and living standards are low. Population growth is not the main reason for the increase and convergence of carbon emissions.

Economic growth is not a factor of carbon emission convergence but is the main cause of carbon emission increase. The regression results of spatial econometric model show that regional economic development has a spillover effect. Changing the mode of economic development is the only way to achieve sustainable development in China.

Technological progress plays a role in promoting the convergence of carbon emissions to a certain extent, but the spillover effect of technological innovation in adjacent regions is not significant. Therefore, as the main way to reduce carbon emissions, technological progress should accelerate technological innovation and take active measures to achieve certain results in reducing carbon emissions.

Industrial structure does not promote the convergence of carbon emissions, but still leads to the increase in carbon emissions. The industrial structure coefficients in the Durbin model are all positive. Some of them pass the significance test. The industrial structure has no effect on the convergence of carbon emissions in nearby areas and has a certain spatial spillover effect, which proves that the industrial structure of the country needs to be rationalized.

The effect of financial development on carbon emission convergence is not significant nor do the adjacent regions show an effective role. This proves that financial reform has achieved some results, but there is still room for improvement.

In theory, the energy price index should be negatively correlated with energy consumption and should play a positive role in promoting the convergence of carbon emissions. From the regression results, the energy price has no significant effect on the convergence of carbon emissions. The main reason may be that the information release system of the energy price is not perfect, and the phenomenon of local protectionism still exists. We should improve the rules and regulations as soon as possible so as to make the energy price play a macrocontrol role.

International trade has not promoted the convergence of carbon emissions but is still a factor leading to the increase of carbon emissions. Interregional international trade has a spillover effect, which proves that China's international trade transformation has made some achievements.

The estimated coefficient of the urbanization rate on carbon emissions is negative, but it has not passed the significance test, and the spatial spillover effect is not significant. Therefore, China should speed up the development

Table 4: Spatial estimation results of provincial carbon emission.

Variable	Spatial lag panel model				Spatial Durbin panel model			
	No fixed effects I	Spatial fixed effects II	Time period fixed effects III	Spatial and time period fixed effects IV	No fixed effects I	Spatial fixed effects II	Time period fixed effects III	Spatial and time period fixed effects IV
C	0.3539 (0.3614)				−0.5349 (0.3282)			
β	−0.0190 (0.0669)	−0.1502 (0.0000)	−0.0112 (0.2632)	−0.1619 (0.0000)	−0.0334 (0.0084)	−0.2049 (0.0000)	−0.0249 (0.0454)	−0.2660 (0.0000)
$\ln P$	−0.0002 (0.9910)	−0.0780 (0.4517)	−0.0036 (0.8567)	−0.0654 (0.5088)	−0.0127 (0.5983)	−0.1281 (0.3414)	−0.0151 (0.5336)	−0.2676 (0.0294)
$\ln A$	0.0493 (0.0181)	0.1399 (0.0000)	0.0380 (0.1507)	−0.0272 (0.6771)	0.0706 (0.0209)	0.2549 (0.0001)	0.0635 (0.0404)	0.1372 (0.0413)
$\ln T$	−0.0286 (0.0106)	−0.0440 (0.0035)	−0.0172 (0.1363)	−0.0212 (0.2125)	−0.0228 (0.0628)	−0.0347 (0.0693)	−0.0174 (0.1478)	−0.0154 (0.3877)
$\ln S$	0.0019 (0.9503)	0.1221 (0.0586)	0.0060 (0.8365)	0.1690 (0.0134)	0.0377 (0.3049)	0.1402 (0.0419)	0.0373 (0.3092)	0.1853 (0.0061)
$\ln F$	−0.0314 (0.0438)	0.0099 (0.6076)	−0.0347 (0.0328)	−0.0039 (0.8435)	−0.0303 (0.0653)	0.0105 (0.5939)	−0.0339 (0.0418)	0.0009 (0.9589)
$\ln E$	−0.0139 (0.8485)	0.0665 (0.3762)	−0.0890 (0.6206)	0.0123 (0.9462)	0.1558 (0.1775)	−0.1645 (0.3256)	−0.0772 (0.6707)	−0.0591 (0.7261)
$\ln \mathrm{EX}$	0.0288 (0.0000)	0.0087 (0.5278)	0.0232 (0.0028)	−0.0045 (0.7699)	0.0343 (0.0000)	0.0264 (0.0740)	0.0302 (0.0018)	−0.0182 (0.2419)
$\ln U$	−0.0774 (0.0070)	−0.0404 (0.3283)	−0.0758 (0.0091)	−0.0429 (0.2881)	−0.0814 (0.0135)	−0.0353 (0.3898)	−0.0767 (0.0155)	−0.0719 (0.0528)
$\ln \mathrm{FD}$	−0.0404 (0.0187)	−0.0491 (0.0511)	−0.0462 (0.0150)	−0.0397 (0.1007)	−0.0433 (0.0324)	−0.0642 (0.0112)	−0.0492 (0.0140)	−0.0546 (0.0150)
$\mathrm{W} \ln I$					0.0460 (0.0665)	0.2374 (0.0007)	0.0373 (0.1706)	−0.0646 (0.4211)
$\mathrm{W} \ln P$					0.0770 (0.0478)	0.4802 (0.0717)	0.0673 (0.1294)	0.2567 (0.3092)
$\mathrm{W} \ln A$					−0.0541 (0.2376)	−0.2769 (0.0022)	−0.0890 (0.0897)	−0.3024 (0.0004)
$\mathrm{W} \ln T$					−0.0191 (0.3638)	−0.0223 (0.3887)	0.0227 (0.3669)	0.0788 (0.0059)
$\mathrm{W} \ln S$					0.0548 (0.4155)	0.2200 (0.1106)	0.0870 (0.2348)	0.4374 (0.0038)
$\mathrm{W} \ln F$					0.0579 (0.0454)	0.0703 (0.0257)	0.0194 (0.5588)	0.0541 (0.1010)
$\mathrm{W} \ln E$					−0.1704 (0.0812)	0.2918 (0.1078)	−0.1622 (0.1314)	0.7745 (0.0012)
$\mathrm{W} \ln \mathrm{EX}$					−0.0095 (0.4585)	−0.0723 (0.0012)	−0.0212 (0.2176)	−0.1527 (0.0000)
$\mathrm{W} \ln U$					0.0463 (0.4789)	0.0720 (0.4555)	0.0458 (0.5109)	0.0410 (0.6508)
$\mathrm{W} \ln \mathrm{FD}$					−0.0225 (0.6011)	−0.0611 (0.2868)	−0.0429 (0.3464)	−0.0523 (0.3406)
ρ	0.2700 (0.0000)	0.2810 (0.0000)	−0.0460 (0.4962)	0.0308 (0.6426)	0.2330 (0.0001)	0.2360 (0.0001)	−0.0510 (0.4584)	−0.0900 (0.1893)
$\mathrm{Log}\, L$	446.0314	476.6667	476.275	513. 6055	454.7283	494.5247	484.3428	539.8509
$\mathrm{Adj}R^2$	0.2177	0.2291	0.1189	0.1099	0.2605	0.3042	0.1496	0.2080

of low-carbon urbanization. With the urbanization process restraining the increase in carbon emissions and with the improvement of the urbanization process, China's urbanization development will achieve better results.

Fiscal decentralization plays a certain role in the convergence of carbon emissions. Its spatial spillover effect is not significant, but it proves that fiscal decentralization plays an important role in reducing carbon emissions. According to this conclusion, we can see that China has been responsibly and actively responding to climate change and exploring a low-carbon economic development path in line with China's national conditions. China's government agencies at all levels have integrated climate issues into all parts of the country for the strategic deployment of regional economic development.

Spatial carbon emission convergence has shown a certain spillover effect, so we should increase efforts to actively promote the effect of interregional carbon emission

convergence, combined with the construction of regional low-carbon clusters.

5. Research Conclusions

China's regional carbon emissions are overall divergent, and there is no σ convergence. Considering the spatial effect, an absolute beta convergence phenomenon was found to exist when the spatial spillover effect among regions was considered, and it was shown that China's regional coordinated emission reduction has achieved certain results. On the premise of speeding up economic construction, we should actively strengthen regional cooperation while considering that developed regions drive backward regions, adhere to low-carbon economic construction, and slow down the growth of carbon emissions. The development of low-carbon economic cooperation should be accelerated, and the dependence on high energy consumption and high emissions as the main body in economic development should be transformed. Efforts are needed to actively accelerate technological innovation and the construction of local government team, implement the strategy of regional coordinated development, and consider urban agglomeration as required to build a coordinated development pattern of large- and medium-sized cities and small towns so as to jointly promote the development of a low-carbon economy in China.

According to our research conclusions, China's population is not the main factor in increasing carbon emissions. China should strengthen international cooperation in low-carbon economic construction and low-carbon industrial cooperation, reduce the rate of increase in carbon emissions, coordinate the coordinated development of regional economies, improve the enthusiasm of low-carbon economic development, and promote the development of low-carbon industries in China so as to realize the transformation to a low-carbon economy in the whole country.

We found that technological progress has a significant effect on carbon emission convergence but that the industrial structure has none. China should accelerate the role of the industrial structure on carbon emission convergence spillover, guiding the rational flow of social capital, promoting the effective allocation of resources, and actively forming low-carbon innovation construction of low-carbon industrial clusters on the basis of adjusting the industrial structure. The development of a low-carbon economy necessarily requires the research and development of low-carbon technology, which requires a large amount of investment and high risk, and must play a leading and promoting role in the government. While focusing on the heterogeneity of local economic development, government departments should not ignore the role of spatial effects on carbon emissions and other influencing factors and should promote the development of a low-carbon economy in the region through the development of an adjacent regional economy. Lastly, it was found that fiscal decentralization has made some achievements in the convergence of carbon emissions, but energy prices have not achieved the desired results. Therefore, we should actively develop green finance, establish green production and consumption policy orientation, strengthen the role of local governments in financial regulation, actively adopt financial policy orientation, adjust the export trade situation with energy-saving industries as major actors, and take practical actions. China has different stages of regional economic development. China should establish and implement low-carbon development measures and policies that are adapted to local conditions. Government departments can actively guide enterprises to build low-carbon competitive advantages and promote enterprises to develop low-carbon technology. The government can coordinate the relationship between international trade and carbon emissions, formulate environmental regulations reasonably and effectively, improve low-carbon technologies for energy saving and emission reduction, and focus on reducing the intensity of carbon emissions for enterprises with a large proportion of exports. The reduction of carbon emissions, while developing international trade, is urgent. Therefore, China should actively participate in the practice of global governance, take the initiative to assume international responsibilities that match our national conditions and development stages, promote the establishment of a fair and reasonable climate governance system, and enter a new era of low-carbon economic development.

Data Availability

The data used to support the findings of this study are available from the corresponding author upon request.

Conflicts of Interest

The author declares that there are no conflicts of interest regarding the publication of this paper.

Acknowledgments

This work was funded by the China Scholarship Council, the China Postdoctoral Science Foundation (project approval number: 2016M601240), and the Doctoral Foundation of Northeastern University at Qinhuangdao (project approval number: XNB201704).

References

[1] W. Swan, "Economic growth and capital accumulation," *Economic Record*, vol. 32, no. 2, pp. 334–661, 1956.

[2] R. M. Solow, "A contribution to the theory of economic growth," *The Quarterly Journal of Economics*, vol. 70, no. 1, pp. 65–94, 1956.

[3] E. D. Domar, "Capital expansion, rate of growth, and employment," *Econometrica*, vol. 2, no. 14, pp. 137–147, 1946.

[4] J. Wang and H. Chanfei, "Energy consumption, economic growth and CO_2 emissions in China—analysis based on logarithm mean divisa decomposure method," *Resources and Environment in the Yangtze Basin*, vol. 19, no. 1, pp. 18–23, 2010.

[5] L. Wu, S. Kaneko, and S. Matsuoka, "Driving forces behind the stagnancy of China's energy-related CO_2 emissions from 1996 to 1999: the relative importance of structural change,

intensity change and scale change," *Energy Policy*, vol. 33, no. 3, pp. 319–335, 2005.

[6] S. Dhakal, S. Kaneko, and H. Imura, "CO_2 emissions from energy use in east Asian mega-cities: driving factors and their contributions," *Environmental Systems Research*, vol. 31, no. 2, pp. 209–216, 2003.

[7] L. Liu and Ji Liu, "Using LMDI to analyze the driving forces in industrial CO_2 intensity: evidence for Xinjiang," *Ecological Economy*, no. 4, pp. 34–38, 2011.

[8] A. Zhao and Li Dong, "EKC test for China's carbon dioxide emissions and analysis of the affecting factors," *Science of Science and Management of S & T*, vol. 33, no. 10, pp. 107–115, 2012.

[9] T. Fan and L. Ruiling, "Study on influence factors for carbon dioxide emissions in China's chemical industry with LMDI method," *China Soft Science Magazine*, no. 3, pp. 166–174, 2013.

[10] L. Zhang, J. Lei, and X. Zhang, "Variations and influential factors of carbon emissions of primary energy consumption in Xinjiang during the period 1952–2008," *Resources Science*, vol. 34, no. 1, pp. 42–49, 2012.

[11] H. Wang and X. Yan, "Influence factors VS. Developments of China's household carbon emissions," *Chinese Journal of Management Science*, vol. 25, no. 8, pp. 1–10, 2017.

[12] W. He and K. Zhang, "The decomposition analysis on the influencing factors of China steel industry carbon emission," *Journal of Industrial Technological Economics*, no. 1, pp. 3–10, 2013.

[13] Q. Zhu, X. Peng, Z. Lu et al., "Factors decomposition and empirical analysis of variations in energy carbon emission in China," *Resources Science*, vol. 31, no. 12, pp. 2072–2079, 2009.

[14] G. Li and Z. Li, "Regional difference and influence factors of China's carbon dioxide emissions," *China Population, Resources and Environment*, vol. 20, no. 5, pp. 22–27, 2010.

[15] W. Jingfu, X. Zheng, and W. Tian, "The impact of economic growth, energy consumption and financial development on carbon emission—based on the empirical study of the BRIC countries," *Journal of Chongqing Technology and Business University (Social Sciences Edition)*, vol. 35, no. 1, pp. 42–49, 2018.

[16] Q. Zhu, X. Peng, and Z. Lu, "Analysis model and empirical study of impacts from population and consumption on carbon emissions," *China Population, Resources and Environment*, vol. 20, no. 2, pp. 98–102, 2010.

[17] C. L. Weber, G. P. Peters, and D. Guan, "The contribution of Chinese exports to climate change," *Energy Policy*, vol. 36, no. 3, pp. 3572–3577, 2008.

[18] C. Bhowmik, S. Bhowmik, A. Ray, and K. M. Pandey, "Optimal green energy planning for sustainable development: a review," *Renewable and Sustainable Energy Reviews*, vol. 71, no. 71, pp. 796–813, 2017.

[19] K. Li and S. Qi, "Trade openness, economic growth and carbon dioxide emission in China," *Economic Research*, no. 11, pp. 60–72, 2011.

[20] N. Birdsall, *Another Look at Population and Global Warming: Population, Health and Nutrition Policy Research. Working Paper*, vol. 1020, World Bank, WPS, Washington, DC, USA, 1992.

[21] T. Knapp and R. Mookerjee, "Population growth and global CO_2 emissions," *Energy Policy*, vol. 24, no. 1, pp. 31–37, 1996.

[22] D. Romero-Ávila, "Convergence in carbon dioxide emissions among industrialised countries revisited," *Energy Economics*, vol. 30, no. 5, pp. 2265–2282, 2008.

[23] R. Ezcurra, "Is there cross-country convergence in carbon dioxide emissions?" *Energy Policy*, vol. 35, no. 2, pp. 1363–1372, 2007.

[24] G. Gao and H. Ma, "Carbon emission convergence in China: quantile regression based on panel data," *Statistics & Decision*, no. 18, pp. 25–28, 2012.

[25] Y. Qian and H. Liu, "The convergence of carbon dioxide emissions in China: the perspective of stochastic convergence with two emission indicators," *Economic Review*, no. 40, pp. 73–80, 2013.

[26] S. Shao, Xi Zhang, and X. Zhao, "Empirical decomposition and peaking pathway of carbon dioxide emissions of China's manufacturing sector—generalized divisia index method and dynamic scenario analysis," *China Industrial Economics*, no. 3, pp. 44–63, 2017.

[27] X. Tong, "On the convergence of China's regional carbon emissions," *Journal of Northeastern University Social Science*, vol. 19, no. 4, pp. 364–370, 2017.

[28] C. Zhang, *A Thesis Submitted to Chongqing University in Partial Fulfillment of the Requirement for the Doctor's Degree of Management*, Chongqing University, Chongqing, China, 2016.

[29] X. Tong, X. Li, L. Tong, and X. Jiang, "Spatial spillover and the influencing factors relating to provincial carbon emissions in China based on the spatial panel data model," *Sustainability*, vol. 10, no. 12, p. 4739, 2018.

Hindawi
Advances in Meteorology
Volume 2019, Article ID 5947976, 10 pages
https://doi.org/10.1155/2019/5947976

Research Article

Preliminary Evaluation of the HOBO Data Logging Rain Gauge at the Chuzhou Hydrological Experiment Station, China

Zehui Zhou,[1,2] **Bin Yong**,[1,2] **Jiufu Liu**,[3] **Aimin Liao**,[3] **Niu Wang**,[3] **Ziwei Zhu**,[2] **Dekai Lu**,[2] **Wang Li**,[2] **and Jianyun Zhang**[3]

[1]*State Key Laboratory of Hydrology-Water Resources and Hydraulic Engineering, Hohai University, Nanjing 210098, China*
[2]*School of Earth Sciences and Engineering, Hohai University, Nanjing 211100, China*
[3]*Nanjing Hydraulic Research Institute, Nanjing 210029, China*

Correspondence should be addressed to Bin Yong; yongbin_hhu@126.com

Received 22 March 2019; Revised 25 July 2019; Accepted 3 October 2019; Published 4 November 2019

Guest Editor: Zia ul-Haq

As a tipping bucket rain gauge, the HOBO Data Logging Rain Gauge RG3-M (RG3-M) has been widely used for the field precipitation observation owing to its superiority of independent power supply by a small portable battery. To quantify the measurement accuracy of the RG3-M gauge, a standard Manual Gauge (MG) and eight other models of tipping bucket rain gauges were installed at the Chuzhou hydrological experiment station of China. In this study, we first compared and investigated the accumulated mounts of 18 rainfall events of two RG3-M gauges benchmarked by the standard MG. Then, five typical rainfall events were chosen to further analyse the observed accuracy of the RG3-M gauge for different rainfall intensities at hourly temporal scale. Finally, the impacts of wind speed and rainfall intensity on the precipitation measurements of the RG3-M gauge were preliminarily explored. Results indicate that the RG3-M gauge measurement generally underestimates rainfall approximately −4% against the standard MG observation, but the maximum deviation even reaches −12.87%. In terms of the hourly rainfall process, the reliable measurement scope of the RG3-M gauge is ranging from 1.5 to 3 mm/h; however, it should be noted that the underestimation is rather significant at the higher rainfall rates (>6 mm/h). Last, it was found that rainfall intensity is a nonnegligible factor for influencing the measurement of the RG3-M gauge. But the windy effect seems to be insignificant in our experiments, which might be attributed to the similar exposure of the compared gauges.

1. Introduction

As one of the most important water cycle elements, precipitation is the release of water from the atmosphere to reach the surface of the earth. Measurement of precipitation has a long history, but till now precisely measuring precipitation is still a challenging task due to the high spatio-temporal variability and inhomogeneity of precipitation itself [1, 2]. Rain gauges can provide point observations of precipitation and are normally recognized as "ground truth" for validating the radar-estimated or satellite-retrieved rainfall [3]. However, in practice, some systematic and random errors, such as the diversity of rain gauge designs, wind-induced gauge undercatch, human operating errors, and the instability of gauge installations, inevitably affect the accuracy of gauge-measured precipitation [4, 5].

In previous studies, the World Meteorological Organization (WMO) carried out several intercomparison projects of precipitation measurement, and many efforts have been made to quantify the accuracy of different rain gauges and analyse the uncertainties and biases existing in gauge-measured precipitation [6–14]. These projects have achieved satisfactory results for the observational performance of the rain gauges they have studied. With the development of the times, it is necessary to study the latest and most practical automatic rain gauge to measure precipitation.

Currently, the Chinese meteorological network operated by the China Meteorological Administration (CMA) consists of over 30,000 automated recording rainfall gauges, most of which are distributed in the eastern and southern regions of China. These automated rain gauges mainly include three types, namely, the tipping bucket rain gauge

(TBR), the weighing rain gauge, and the siphon rain gauge. Among them, the most popular rain gauge is TBR owing to its simple, durable, highly reliable, and inexpensive design [15–17]. However, the majority of TBRs need an external power supply. As a special model of TBRs, the HOBO Data Logging Rain Gauge RG3-M (RG3-M) is a battery-powered rainfall data collection and recording system, which includes one small lithium battery (3 volt, CR-2032) embedded in its data logger enveloped by waterproof material inside the gauge cylinder. The portable battery could last about 1 year for conventional use. Because of this advantage, RG3-M gauges are particularly well suited to be installed in remote regions for various research studies of meteorology, hydrology, ecology, and agriculture [18–21]. Nevertheless, literature survey suggests a specific investigation for the measuring accuracy of the RG3-M gauge, particularly based on the field experiments, is still lacking.

The focus of this study is entirely experimental. Altogether 10 models of rain gauges installed in the Chuzhou hydrological station, China, were employed to record the rainfall events and raining processes. Here, we collected the observed rainfall data of 18 rainfall events occurred in 2017 to quantify the measurement accuracy of the RG3-M gauge. First, we compared the accumulated rainfall amounts of two tested RG3-M gauges and validate their measuring biases by employing a standard Manual Gauge (MG) as the reference. Next, we furtherly analysed error feature and variation process of different rain gauges with different rainfall intensities at the hourly scale. Finally, we attempted to detect the effects of both wind speed and rainfall intensity on the measurements of the RG3-M gauge during different rainfall events. We believe that our analysis results will be of great interest to both meteorologists and hydrologists who have been or want to be the RG3-M gauge users.

2. Materials and Methods

2.1. Observation Site. The experimental observation site is the Chuzhou hydrological experiment station located within the Huashan watershed at the eastern region of Anhui Province, China (Figure 1(a)). The station operated by the Nanjing Hydraulic Research Institute (NHRI) is approximately 87 km away from the Nanjing city at latitude of 32°17′28.61″N and longitude of 118°12′24.31″E. It has a typical subtropical humid monsoon climate. The main purpose of the station is to monitor the hydrometeorological elements of typical humid climate region and investigate the hydrological mechanism of rainfall-runoff. Our experiments of rainfall observations were performed at the Hydrometeorological Observation Field (Figure 1(b)), which is just situated in the centre of the station. In 2012, an automatic weather station system and a near-surface meteorological gradient observation system were installed in the field to obtain the conventional meteorology elements, mainly including rainfall, relative humidity, total radiation, soil temperature, and atmospheric pressure, and the wind speed, air temperature, and relative humidity at different heights (2, 4, 6, 8, and 10 meters).

2.2. Rain Gauges. To comprehensively intercompare the measuring features of different rain gauges, we installed a manual gauge (MG) and nine models of TBRs at the Hydrometeorological Observation Field in 2016, including the RG3-M, TR-525, TR-525M, JDZ01, JDZ02, JDZ05, JDZ10, TJ01, and TJ05. Figure 1(c) shows the spatial positions of all rain gauges in the field. The distance between two adjacent rain gauges is controlled within 1-2 m. According to the Chinese national standard, all gauges were installed in the field with 70 cm length from the TBR top to the ground surface. During the installation, all the connection cables between the gauge and the logger are enclosed in a weatherproof box to avoid direct exposure to the air. The instrument parameters of ten models of rain gauges are summarized in Table 1.

First, the MG was installed at the field for benchmarking the total rainfall amounts measured by all the TBRs. Currently, the MG-measured rainfall amounts can be obtained by two ways, i.e., the weighting method and the horizontal visual method with a measuring cylinder. There is small difference between these two experimental methods. Hence, here we selected the latter owing to its simple operation (Figure 2(d)).

As for the three TBRs (RG3-M, TR-525, and TR-525M) made in USA, one can note that they have different resolution (0.2 mm, 0.254 mm, and 0.1 mm) and barrel diameter (152.4 mm, 163 mm, and 245 mm). The data logger of RG3-M, whose power source comes from a small lithium battery, can record the time of each tip and the instantaneous temperature (Figure 2(c)). The TR-525 gauge has been tested and used in the Ohio's Upper Big Walnut Creek Watershed [15]. The experimental results showed that the TR-525 gauge has a larger deviation compared to other gauges.

Additionally, the series of JDZ and TJ gauges have been widely applied in China for the liquid precipitation observations. In our study, there are four types of JDZ gauges, which represent four different resolutions, i.e., JDZ01 (0.1 mm), JDZ02 (0.2 mm), JDZ05 (0.5 mm), and JDZ10 (1.0 mm), respectively. Differing from other TBRs, the TJ gauges do not have the filter screen which can screen out various fragments such as leaves and branches. In the experimental field, there are two models of TJ gauges, i.e., TJ01 and TJ05 with resolutions of 0.1 mm and 0.5 mm, respectively. Specifically, the barrel diameter of all rainfall gauges made in China is the same 200 mm. Note that the resolution (0.2 mm) of the studied RG3-M is the same as that of JDZ02.

2.3. Laboratory Calibration. Based on the reference of GB/T 11832-2002 "tipping bucket rain gauge" [22] and the WMO laboratory calibration standard, all the experimental TBRs were first calibrated individually in the laboratory before installation in the field. The calibration process mainly consists of two steps. For the first step, we performed the volumetric calibration for rain gauges. By pouring 10 mm water into the tested gauge each time, we recorded the counting number of the tipping bucket and then carefully adjusted the correction screw under the gauge base. This

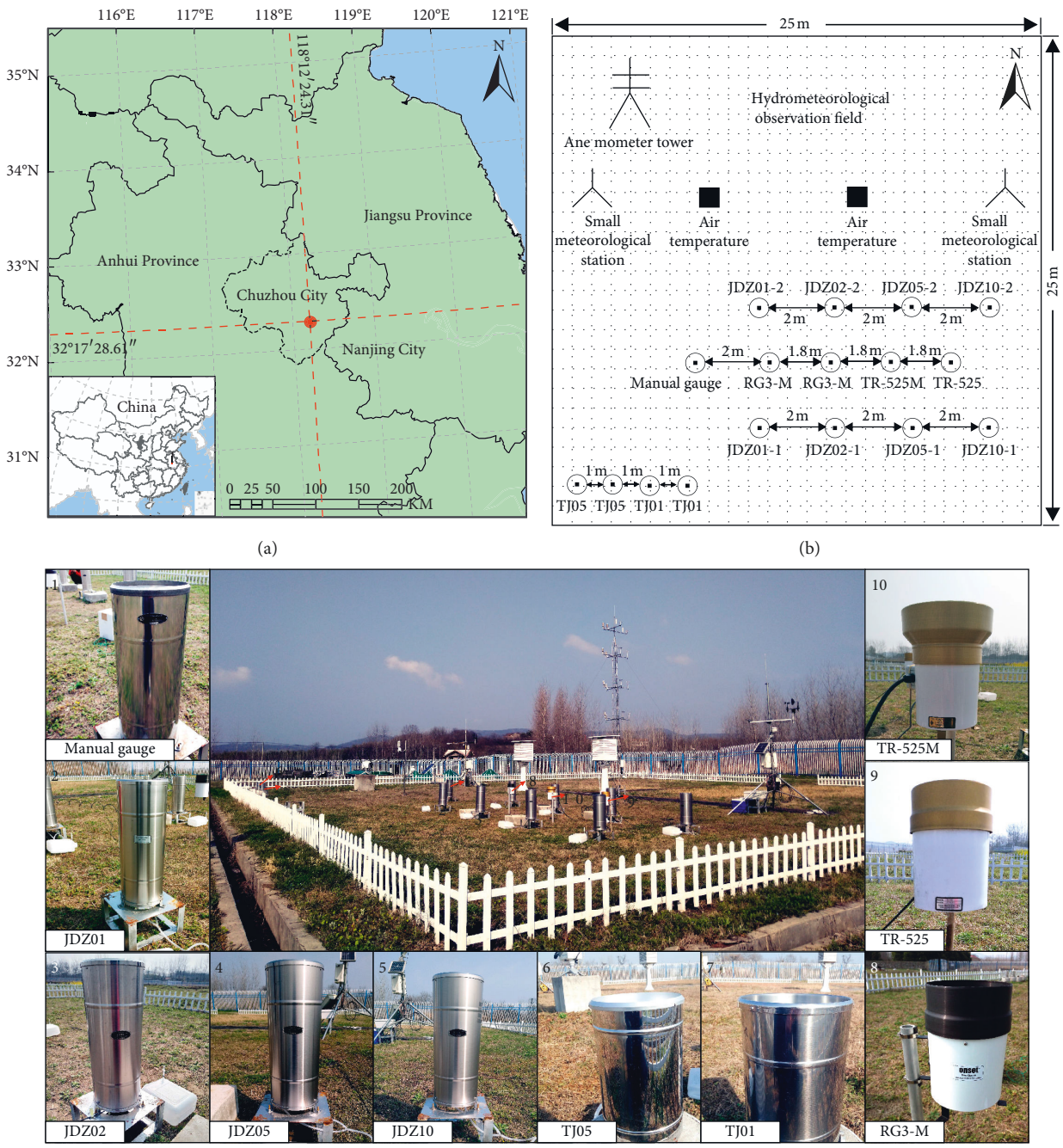

Figure 1: (a) Field view of the Chuzhou hydrological experiment station, (b) distribution of 10 models rain gauges, and (c) the site of hydrometeorological observation field.

process was repeated several times for each gauge till that the tipping bucket reached the required resolution. Second, we carried out the dynamic calibration for each rain gauge. The dynamic calibration used an automatic calibration device developed by the Nanjing Hydraulic Research Institute (NHRI) [23], which can produce a series of water flows with different speeding rates to simulate different rainfall intensities (Figure 3). This calibration device can also be applied in the field, especially for the periodical test and adjustment for the installed TBRs (Figures 2(a)–2(c)). The purpose of dynamic calibration is to eliminate systematic error as far as possible. Apart from the systematic errors, rain gauges also suffer from random errors. These errors should be kept in mind in comparison with the gauge rainfall.

2.4. Data Collection. At the experiment field, the amount of liquid precipitation obtained from the MG was accurately measured after each rainfall event. All data from TBRs but

Table 1: Instrumental information at the Chuzhou hydrological experiment station.

Model of gauge	Origin	Resolution (mm)	Splash out protection (cm)	Rainfall rate	Diameter (mm)	Operating temperature range (°C)	Calibration accuracy (%)
Manual gauge	Jiangsu, China	—	—	—	200	—	—
HOBO RG3-M	USA	0.2	5	≤2.12 mm/min	152.4	0~+50	±1.0 (up to 2 cm per hour)
TR-525	USA	0.254	5	≤11.67 mm/h	163	0~+50	±1.0 (up to 5 cm per hour)
TR-525M	USA	0.1	5	≤11.67 mm/h	245	0~+50	±1.0 (up to 5 cm per hour)
JDZ01	Jiangsu, China	0.1	14	≤4 mm/min	200	−10~+55	≤4.0
JDZ02	Jiangsu, China	0.2	14	≤4 mm/min	200	−10~+55	≤4.0
JDZ05	Jiangsu, China	0.5	14	≤4 mm/min	200	−10~+55	≤4.0
JDZ10	Jiangsu, China	1.0	14	≤4 mm/min	200	−10~+55	≤4.0
TJ05	Tianjin, China	0.5	20	≤5 mm/min	200	−10~+50	≤5.0
TJ01	Tianjin, China	0.1	20	≤5 mm/min	200	−10~+50	≤5.0

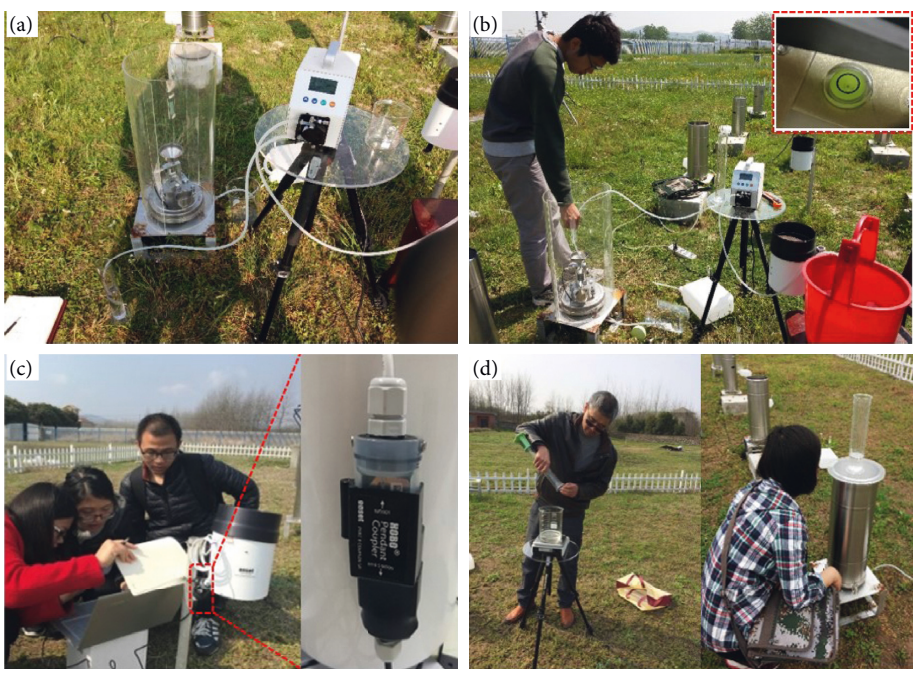

Figure 2: (a) Peristaltic pump used for calibration. (b) The calibration of tipping bucket rain gauge. (c) Obtaining the data from RG3-M (left), the data logger (right). (d) Comparison of precipitation measurement for the manual gauge: weighting method (left) and horizontal visual method (right).

for RG3-M record through a data acquisition system in time step of one minute. The data logger of the RG3-M gauge can instantaneously record both rainfall amount and temperature when the gauge collects 0.2 mm of rainfall to trigger the tipping bucket flipping once. By dynamic calibration testing, we found that the mechanical biases of RG3-M gauges have been corrected before they leave the factory. The wind speed at the height of 2 m observed by the automatic weather station system was made available at 10 min resolution. All meteorological data were performed by the data quality control in this study.

3. Methods

In this study, we adopt the approaches proposed by Duchon and Essenberg [3] and Tokay et al. [24] to comprehensively evaluate the performance of the RG3-M gauge from three perspectives. First, we validated the observation accuracy of

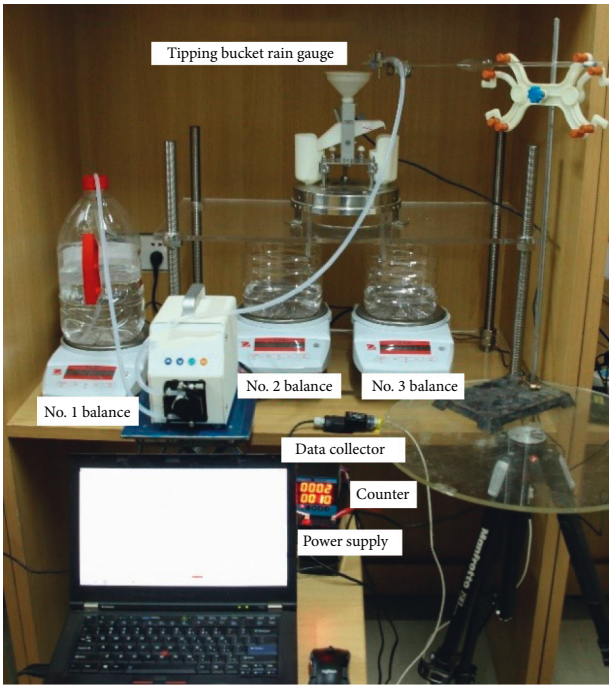

Figure 3: Calibration system.

RG3-M for rainfall events benchmarked by the MG gauge. Two statistical indices, namely, the Relative Bias (BIAS) and Relative Root Mean Squared Error (RRMSE), are used to calculate the error of RG3-M against the MG gauge. The BIAS measures the systematic errors, whereas the RRMSE is amplified by both systematic and nonsystematic errors. The formulas for the two statistics are

$$\mathrm{BIAS} = \frac{T_{\mathrm{g}} - T_{\mathrm{m}}}{T_{\mathrm{m}}} \times 100\%,$$
$$\mathrm{RRMSE} = \frac{\sqrt{(1/n)\sum_{i=1}^{n}\left(T_{\mathrm{g}} - T_{\mathrm{m}}\right)^2}}{(1/n)\sum_{i=1}^{n} T_{\mathrm{m}}}, \tag{1}$$

where n represents the sample size at each rain intensity range, and T_{g} and T_{m} represent the total rainfall of each event recorded by the gauge and MG, respectively. Second, the validation of rainfall events cannot completely reflect the observation ability of a rain gauge because the dynamic change of precipitation has also obvious distinctions at shorter time scales rather than at event scale [5]. Considering that it is impossible to get referenced rainfall at short time scales by MG, here we will select a best TBR with the highest observation accuracy to test the rainfall measurements of RG3-M at hourly scale. Finally, we analysed the impact of both wind speed and rainfall intensity on RG3-M on the basis of the wind speed and the rainfall intensity corresponding to the recording step of hourly rain observations.

4. Results and Discussion

4.1. Rainfall Events. The observed rainfall and meteorological data from March to September in 2017 are used in our study. The rainfall data can provide 18 complete rainfall events. Figure 4 demonstrates the comparison results between two RG3-M gauges and MG. As can be seen from Figure 4(a), the RG3-M gauges generally underestimate the rainfall amounts for almost all the events compared to the referenced MG (Figure 4(a)). In terms of the average precipitation intensity for each event, the BIAS of RG3-M ranges from −12.87% to 3.92% (Figure 4(b)). Thus, the average BIAS of RG3-M is calculated as −3.96%, which mainly contributed from light and moderate rain events. During the raining process, we found that the screen strainer of RG3-M is easier to form a kind of thin liquid sheet, which easily rebounds some raindrops out of the gauge especially for larger rainfall. Additionally, the diameter of RG3-M (152.4 mm) is smaller than that of the MG (200 mm) and other TBRs (see Table 1). In particular, we also note that the length from barrel top to screen strainer of RG3-M is much shallower than that of other gauges. This is likely to be the major reason for the underestimation of RG3-M observation. According to different rain intensity ranges, next we categorized the 18 rainfall events into 4 classes, i.e., 0–0.5 mm/h, 0.5–1.5 mm/h, 1.5–3 mm/h, and ≥3 mm/h, respectively. With regard to BIAS, the RG3-M gauges have rather good agreement (average bias = 1.79%) with MG at the range of 1.5–3.0 mm/h, while they exhibit an obvious underestimation (<−4%) at other intensity ranges. As for RRMSE, the error value (3.05%) is closer to zero for the range of 1.5–3.0 mm/h than other ranges, which is consistent with that of BIAS. Our experimental results indicate that the best range of rain intensity for RG3-M is 1.5–3.0 mm/h (Figure 4(c)).

Since the MG can only record the total precipitation for every raining event, it could not reflect the variation process of rainfall at short time scale. It is necessary to select an accurate tipping bucket gauge for validating the hourly rainfall of the RG3-M gauge. Comparison results of other TBRs against MG are provided in Table 2. In general, the JDZ gauges underestimate the rainfall amounts and the other gauges overestimate the rainfall amounts. It can be seen that the TR-525 gauge shows a larger deviation (average bias up to 20%), which is similar to the conclusion in Shedekar et al. [25]. The average bias of TJ05 gauge is 3.02%, which is another positive deviation gauge besides TR-525 gauge, but its value is smaller than TR-525. As for the JDZ gauges, the overall underestimation is greatest in the case of JDZ01 gauge (average bias = −18.07%), followed by JDZ02 gauge (average bias = −4.47%) and JDZ10 gauge (average bias = −4.14%), and the best is JDZ05 gauge (average bias = −1.51%). Moreover, the performance of the two JDZ05 gauges is rather stable since they record almost the same amount of total rainfall. In addition, JDZ05 matched with the MG measurements rather well and is always equivalent to the average values of all the TBRs for three typical rainfall events with different magnitudes (Figure 5). Therefore, in this study, we selected the JDZ05 gauge as the benchmark for detecting the varying errors of RG3-M at the hourly scale.

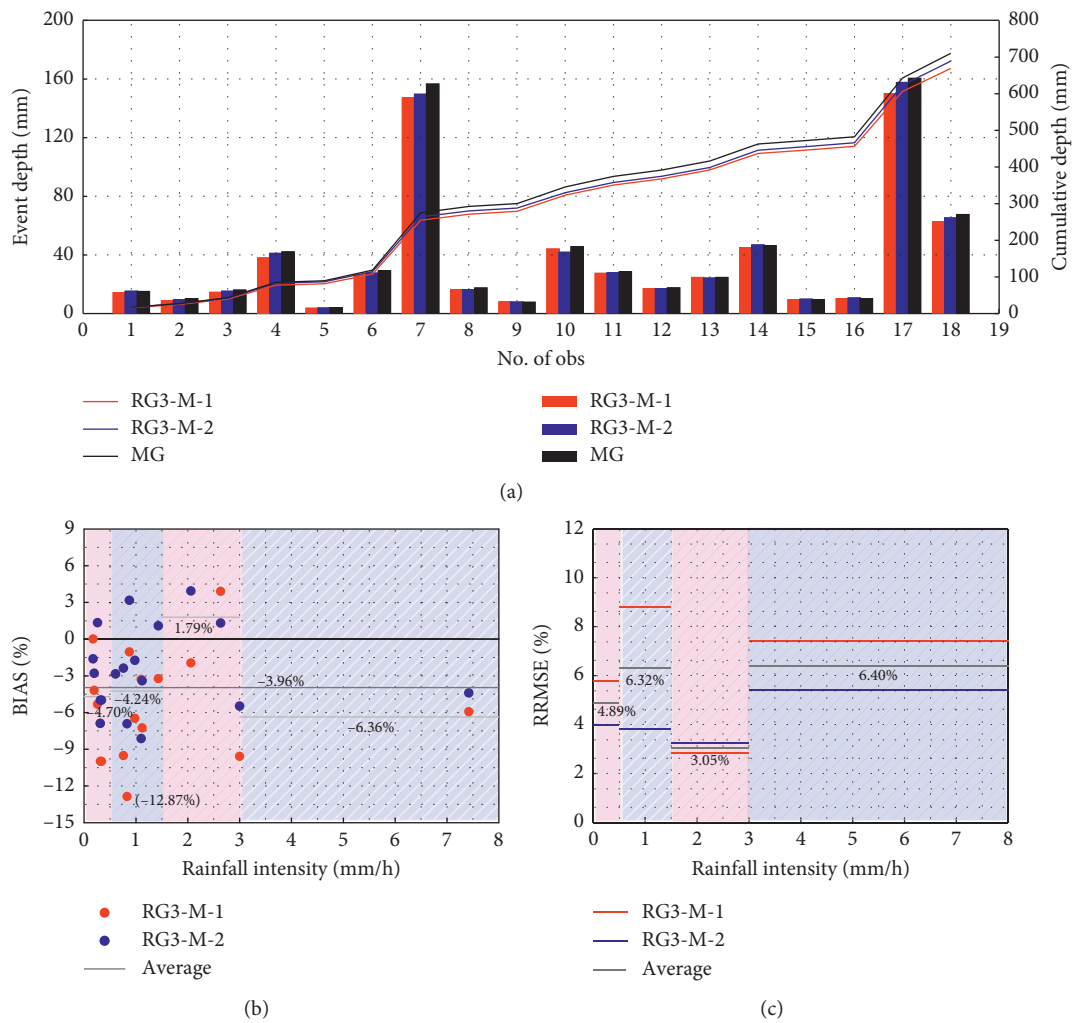

Figure 4: (a) Rainfall data measured by RG3-M gauges at the hydrometeorological observation field during 18 rainfall events compared to data recorded at the adjacent MG (bars represent event totals, and lines represent cumulative rainfall depth). (b) The relationship between BIAS and rainfall intensity (rainfall total ÷ even duration) using event total amounts. (c) The distribution of RRMSEs at four rain intensity ranges.

Table 2: Total precipitation (mm) and BIAS (%) for 11 rain gauges against the manual gauge in five rainfall events at hydrometeorological observation field.

	Manual gauge (mm)	JDZ (0.1 mm)		JDZ (0.2 mm)		JDZ (0.5 mm)		JDZ (1.0 mm)		TJ (0.5 mm)		TR-525 (0.254 mm)
		JDZ01-1	JDZ01-2	JDZ02-1	JDZ02-2	JDZ05-1	JDZ05-2	JDZ10-1	JDZ10-2	TJ05-1	TJ05-2	
2017 03/19 05:01–03/20 08:00												
Total (mm)	8	6.4	6	7.4	7	7	7	8	6	8.5	7.5	9.144
BIAS (%)	0	−20.00	−25.00	−7.50	−12.50	−12.50	−12.50	0	−25.00	6.25	−6.25	14.30
2017 04/04 17:01–04/06 16:00												
Total (mm)	16	13.8	13.3	16	15.4	16	16.5	17	16	16.5	16.5	19.812
BIAS (%)	0	−13.75	−16.88	0	−3.75	0	3.13	6.25	0	3.13	3.13	23.83
2017 04/08 19:01–04/11 01:00												
Total (mm)	42	30.4	34.9	42.4	41.4	43	43	45	42	42.5	44	53.086
BIAS (%)	0	−27.62	−16.9	0.95	−1.43	2.38	2.38	7.14	0	1.19	4.76	26.40
2017 04/16 18:01–04/17 05:00												
Total (mm)	4	3.3	3.1	3.8	3.6	4	4	4	3	4	4.5	4.826
BIAS (%)	0	−17.5	−22.5	−5	−10	0	0	0	−25	0	12.5	20.65
2017 05/03 23:01–05/04 08:00												
Total (mm)	29.2	28	24.4	28.8	28	29.5	29.5	30	27	30	30	36.322
BIAS (%)	0	−4.11	−16.44	−1.37	−4.11	1.03	1.03	2.74	−7.53	2.74	2.74	24.39
MB (%)	0	−18.07		−4.47		−1.51		−4.14		3.02		21.92

Notes: MB = mean BIAS of same model gauges; JDZ01-1 = No.1 JDZ01 rain gauge; JDZ01-2 = No.2 JDZ01 rain gauge; other models of rain gauge are the same as above.

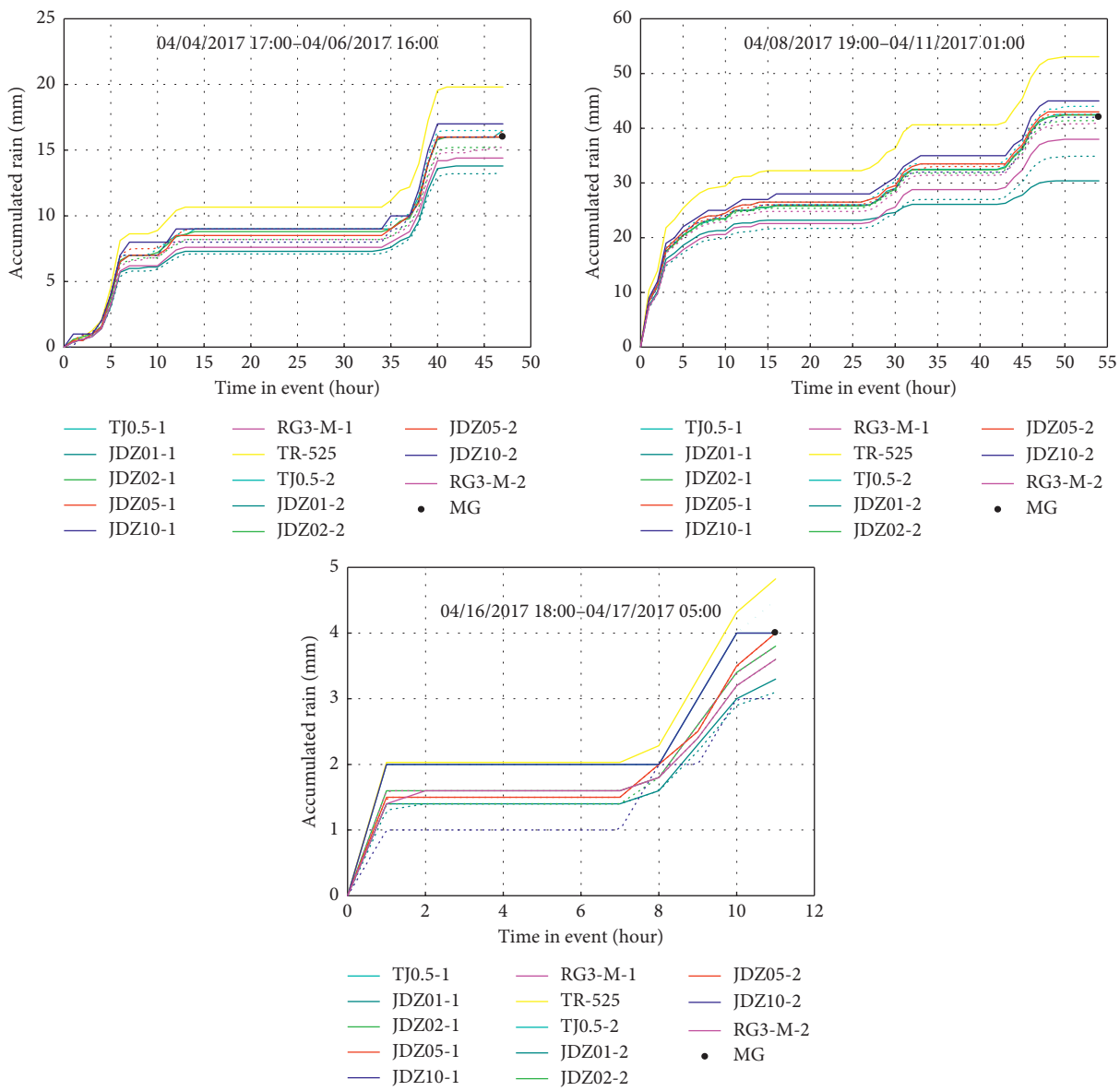

Figure 5: Cumulative rainfall measured by 13 rain gauges for three storms on 4 April 2017, 8 April 2017, and 16 April, 2017 recorded at the Hydrometeorological Observation Field, respectively (dot indicates the total depth of rainfall recorded by the manual gauge).

4.2. Hourly Rainfall. Considering that the difference of resolution between RG3-M and JDZ05 might cause errors at a short time step, we adopt the average hourly rainfall of two gauges with the same model in our comparison. Figure 6 shows the comparison of average hourly rainfall observation obtained from the RG3-M gauges against that of the JDZ05 gauges. Altogether, 67 hourly rainfall events were involved in the analysis. In this scattergram, a summary of the comparison between the two variables is shown in the upper left. The purpose of these summaries is to obtain a sense of the actual magnitude of differences in contrast to the results from linear regression. The solid line is the 1:1 line, and the dashed line is the least squares simple linear regression of the RG3-M gauge onto the JDZ05 gauge. The regression equation is given in the lower right quadrant of the figure.

The hourly precipitation of RG3-M and JDZ05 exhibits an evident linear distribution with R^2 of 0.993 (Figure 6). However, the scatter points slightly fluctuate around the fit line under the light rain intensity (0–2 mm/h). This could be attributed to the different resolution of the two gauges (0.2 mm for RG3-M but 0.5 mm for JDZ05), which also explained the relatively larger negative bias of RG3-M against JDZ05 (−11.02%). These two models of gauges show a good agreement at the range of moderate rain (2-3 mm/h), which is consistent with the result in Figure 4. In addition, one can see that the underestimation of RG3-M is gradually increasing with the increase of rain intensity especially for the range of exceeding 3 mm/h. It is because the smaller tipping bucket of the RG3-M gauge could not flip quickly when the rain intensity increases beyond the threshold, which is consistent with the limitations of tipping bucket

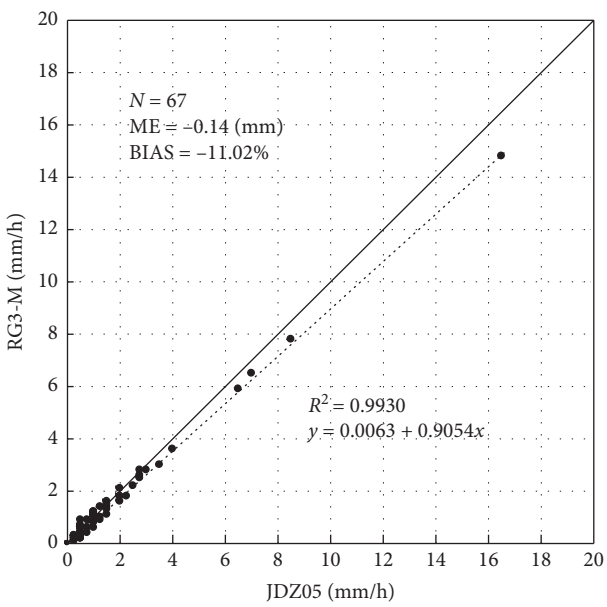

Figure 6: Comparison of average hourly rainfall of the RG3-M gauge and the JDZ05 gauge at the hydrometeorological observation field.

rain gauges described by Molini et al. [26]. In a word, The RG3-M gauge rainfall event totals are, on the average, −11.02% smaller than those of the JDZ05 gauge, and the average absolute difference is 0.14 mm, which mainly results from the difference in moderate and large rain intensities.

4.3. Impact of Wind Speed and Rainfall Intensity on RG3-M Measurements. To further understand the performance of RG3-M in the field experiments, next we examined the hourly difference between RG3-M and JDZ05 considering both wind speed at 2 m height and rainfall intensity. The analysis in this section aims to identify the possible dominant factor influencing the observed accuracy of rain gauges.

Figures 7(a)–7(c) display scatterplots showing the differences between the two RG3-Ms as a function of wind speed, rainfall intensity, and both factors, respectively. The figure plots show that the range of the difference varies from 0 mm to 0.8 mm under different conditions of wind speed and rainfall intensity. Generally, the hourly measurements of the two gauges with the same model of RG3-M are almost equal each other. Their difference is less than 0.2 mm (only one tip of RG3-M) per hour, which most likely is due to the time interval and random errors. The consistent performance of the different RG3-M gauges also further verified the reliability of the volumetric calibration procedure used in our experiments. On the other hand, the stability of RG3-M gauge seems to be hardly affected by wind speed. However, Figure 7(b) suggests that the difference between these two RG3-M gauges increased obviously with the increase of rainfall intensity. Even for lower wind speeds less than 2 m/s, there still exist some rainy events with higher differences due to different rainfall intensity. Further data analysis confirmed that these points are mainly associated with high rain intensity despite low wind speed.

Similarly, we also plotted the difference between RG3-M and JDZ05 at different wind speeds (2 m height) and different rain intensities in Figures 7(d)–7(f). With the increase of wind speed, the difference does not exhibit any apparent tendency (Figure 7(d)). However, the difference between the two models of rain gauges shows a clear upward trend with the increasing rainfall intensity (Figure 7(e)). This result remains consistent with that in Figure 7(d)–7(f).

To further reveal the impact of wind speed and rainfall intensity on rain gauges, we combined these two crucial factors together to analyse the variations of observation difference (see Figure 7(c) and 7(f)). It is apparent that the RG3-M gauge generally demonstrates a relatively poor performance at high rainfall intensity, while the wind speed does not show a significant effect on observation difference between different rain gauges. As for the wind impacts on rain gauges, there still exist disagreements in the prior studies. For example, analysing some experimental observations in the field, Yang et al. [27] considered that the impact of wind speed on the measurements of rain gauges can be negligible. But some other researchers found that the wind could induce undercatch of rain gauges [28, 29]. Our evaluation result cannot support this viewpoint probably due to the relatively small wind speed (less than 5 m/s) observed during the experiments. Such weak wind could not produce significant impacts on the measurements of liquid precipitation in the experimental field site.

Last but not least, we have to admit that the JDZ05 gauge used as a benchmark in this study was exposed to wind in the same way as the tested RG3-M gauge. This is likely to be the cause that led to the little difference between RG3-M and JDZ05. Therefore, an effective windshield device needs to be applied for eliminating the wind impact in the future experiments. In addition, Duchon and Essenberg [3] mentioned that the spatiotemporal distribution of raindrop size played an important role in the magnitude of undercatch. Through a numerical simulation, Nešpor and Sevruk [30] found that larger fraction of smaller raindrops and higher wind speeds could cause greater undercatch for rain events. To better explore the effects of wind and rainfall intensity on the accuracy of the RG3-M gauge, we are installing two raindrop spectrometers at the experimental site. It is anticipated that the impact of several crucial factors on measurements of rain gauges can be revealed better, especially with different wind speed and raindrop size.

5. Conclusions

In this study, measuring accuracy of the portable RG3-M gauge widely used in remote regions was comprehensively investigated by comparing with other 9 models of TRBs at the Chuzhou hydrological experiment station in China. Benchmarked by the standard manual gauge, the rainfall observation of the RG3-M gauge exhibits a clear underestimation with the average bias of −3.96%, ranging from −12.87% to 3.92%. The underestimation of RG3-M might be attributed to some design flaws itself, such as smaller screen mesh and shallow screen strainer (see Supplementary Materials (available here)), which can cause some raindrops

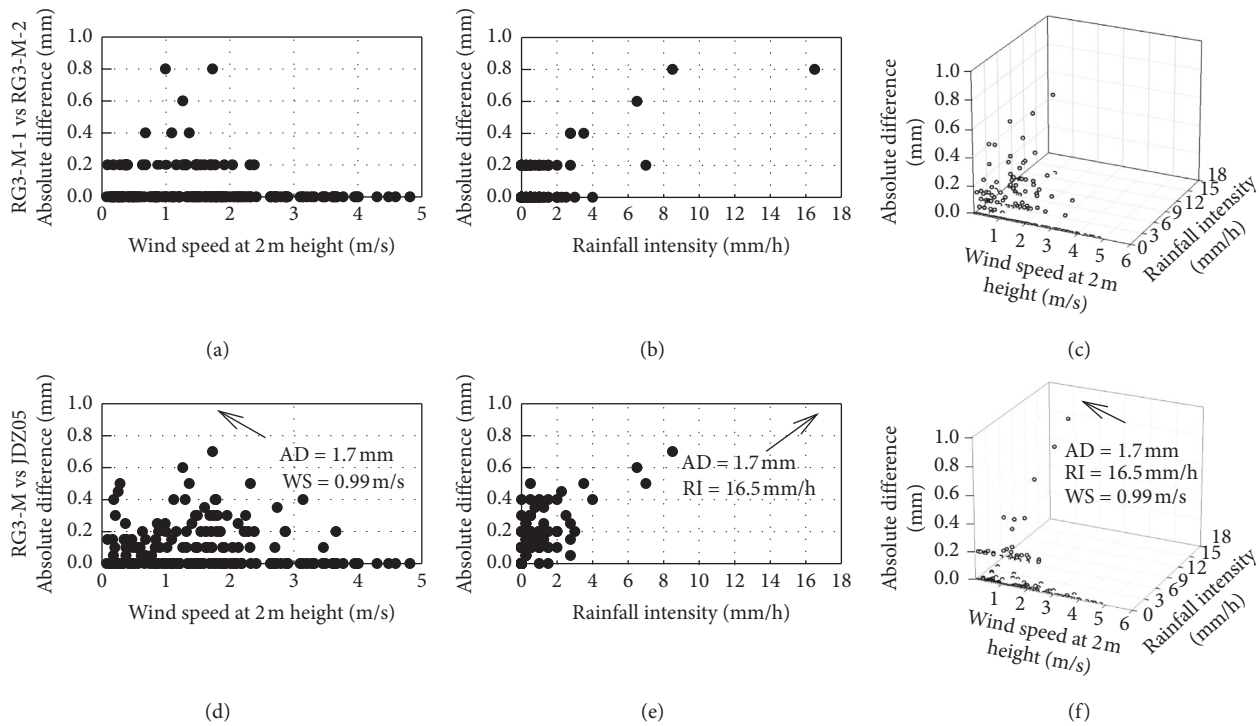

Figure 7: Scatterplots of hourly absolute difference between two tested RG3-M gauges with variation of (a) wind speed and (b) rain intensity, respectively, and (c) three-dimension relationship of the three variables (hourly absolute difference, wind speed, and rain intensity). (d), (e), and (f) correspond to (a), (b), and (c), respectively, but for averaged hourly difference between the RG3-M gauge and the JDZ05 gauge.

splashing out of the gauge especially for larger rainfall intensity.

Our experiments indicate that the RG3-M gauge seems to be suitable for observing the rain intensities at the moderate range of 1.5–3.0 mm/h. As for the hourly rainfall measurement, the underestimation of the RG3-M gauge seems to be serious with the increasing rain intensity especially for the range beyond 3 mm/h. By analysing the impact of both wind speed and rainfall intensity on measurements of RG3-M, we found that rainfall intensity has a significant influence on the measuring accuracy of RG3-M, but the wind effect was not detected in our experiments. The missing correlation with wind can be attributed to the similar exposure of the compared gauges in the current experimental setup. To improve the experimental conditions, two sets of raindrop spectrometers and a new windshield device have been tested in our experimental field. In the further research, the systematic mechanical biases of tested TBRs should be completely corrected.

The preliminary evaluation reported here can provide a wider recognition of the RG3-M gauge for the hydrological and meteorological users. However, owing to the limited number of samples and the lack of special wind-proof instalments, the measuring characteristics of RG3-M, such as seasonality, climatic applicability, and wind impacts, are not completely revealed in this study. In the future, efforts will be focused on investigating these physical features of the RG3-M gauge under different meteorological conditions with a longer observation period and more experimental data.

Data Availability

The data used to support the findings of this study are available from the corresponding author upon request.

Conflicts of Interest

The authors declare that there are no conflicts of interest regarding the publication of this paper.

Acknowledgments

This work would not have been possible without the cooperation of the observers at the Chuzhou hydrological experiment station. The authors would like to acknowledgment Nanjing Hydraulic Research Institute for providing data and feedback on various aspects of data collection and quality and gauge maintenance. This work was financially supported by National Key Research and Development Program of China (2018YFA060202) and the National Natural Science Foundation of China (51979073, 91647203, 51609145).

Supplementary Materials

Figure: comparison of screen strainer and mesh size between RG3-M and the manual gauge. Note that the screen mesh of RG3-M usually forms a thin liquid film during rainfall which easily makes raindrops rebounding out of the strainer. Thus,

more raindrops splash out of the RG3-M gauge than those of manual gauge, especially for the storm with high intensity. (*Supplementary Materials*)

References

[1] M. R. Allen and W. J. Ingram, "Constraints on future changes in climate and the hydrologic cycle," *Nature*, vol. 419, no. 6903, pp. 224–232, 2002.

[2] B. Yong, D. Liu, J. J. Gourley et al., "Global view of real-time TRMM multisatellite precipitation analysis: implications for its successor global precipitation measurement mission," *Bulletin of the American Meteorological Society*, vol. 96, no. 2, pp. 283–296, 2015.

[3] C. E. Duchon and G. R. Essenberg, "Comparative rainfall observations from pit and aboveground rain gauges with and without wind shields," *Water Resource Research*, vol. 37, no. 12, pp. 3253–3263, 2001.

[4] D. Yang, B. Goodison, J. Metcalfe et al., "Compatibility evaluation of national precipitation gage measurements," *Journal of Geophysical Research: Atmospheres*, vol. 106, no. D2, pp. 1481–1491, 2001.

[5] D. Yang and A. Simonenko, "Comparison of winter precipitation measurements by six Tretyakov gauges at the Valdai experimental site," *Atmosphere-Ocean*, vol. 52, no. 1, pp. 39–53, 2014.

[6] V. S. Golubev, P. Y. Groisman, and R. G. Quayle, "An evaluation of the United States standard 8-in nonrecording raingage at the Valdai Polygon, Russia," *Journal of Atmospheric and Oceanic Technology*, vol. 9, no. 5, pp. 624–629, 1992.

[7] E. J. Sadler and W. J. Busscher, "High-intensity rainfall rate determination from tipping-bucket rain gauge data," *Agronomy Journal*, vol. 81, no. 6, pp. 930–934, 1989.

[8] D. Yang, D. L. Kane, L. D. Hinzman et al., "An evaluation of the Wyoming gauge system for snowfall measurement," *Water Resources Research*, vol. 36, no. 9, pp. 2665–2677, 2000.

[9] D. Yang, "Double fence intercomparison reference (DFIR) vs. Bush gauge for "true" snowfall measurement," *Journal of Hydrology*, vol. 509, pp. 94–100, 2014.

[10] D. Yang, B. E. Goodison, J. R. Metcalfe et al., "Accuracy of NWS 8" standard nonrecording precipitation gauge: results and application of WMO intercomparison," *Journal of Atmospheric and Oceanic Technology*, vol. 15, no. 1, pp. 54–68, 1998.

[11] L. G. Lanza and E. Vuerich, "The WMO field intercomparison of rain intensity gauges," *Atmospheric Research*, vol. 94, no. 4, pp. 534–543, 2009.

[12] L. G. Lanza and L. Stagi, "High resolution performance of catching type rain gauges from the laboratory phase of the WMO field intercomparison of rain intensity gauges," *Atmospheric Research*, vol. 94, no. 4, pp. 555–563, 2009.

[13] M. Colli, L. G. Lanza, and P. La Barbera, "Performance of a weighing rain gauge under laboratory simulated time-varying reference rainfall rates," *Atmospheric Research*, vol. 131, pp. 3–12, 2013.

[14] M. Stagnaro, M. Colli, L. G. Lanza, and P. W. Chan, "Performance of post-processing algorithms for rainfall intensity using measurements from tipping-bucket rain gauges," *Atmospheric Measurement Techniques*, vol. 9, no. 12, pp. 5699–5706, 2016.

[15] V. S. Shedekar, K. W. King, N. R. Fausey, A. B. O. Soboyejo, R. D. Harmel, and L. C. Brown, "Assessment of measurement errors and dynamic calibration methods for three different tipping bucket rain gauges," *Atmospheric Research*, vol. 178-179, pp. 445–458, 2016.

[16] L. G. Lanza, E. Vuerich, and I. Gnecco, "Analysis of highly accurate rain intensity measurements from a field test site," *Advances in Geosciences*, vol. 25, pp. 37–44, 2010.

[17] A. Tokay, D. B. Wolff, K. R. Wolff, and P. Bashor, "Rain gauge and disdrometer measurements during the keys area microphysics project (KAMP)," *Journal of Atmospheric and Oceanic Technology*, vol. 20, no. 11, pp. 1460–1477, 2003.

[18] I. Y. Sulen and J. Reuder, "Predictability of precipitation in complex terrain—a comparison of high-resolution rain gauge measurements and fine-scale numerical simulations," in *Proceedings of the EGU General Assembly 2009*, Vinenna, Austria, April 2009.

[19] O. S. Vallejosbarra, R. M. Pizarrotapia, M. A. V. Sandoval et al., "Effect of vegetation on precipitation interception in the Andean foothills of the Maule region, Chile," *Biological Trace Element Research*, vol. 135, no. 1–3, p. 182, 2010.

[20] R. Zhao, J. Zhang, L. I. Yuting et al., "Soil moisture characteristics and its response to rainfall in artificial forests in Loess region of Western Shanxi province," *Journal of Soil and Water Conservation*, vol. 30, no. 1, pp. 178–183, 2016, in Chinese.

[21] J. C. Rodda and H. Dixon, "Rainfall measurement revisited," *Weather*, vol. 67, no. 5, pp. 131–136, 2012.

[22] The First Editorial Room of Standards Press of China, *Compilation of National Standards for Hydrological Instruments*, Standards Press of China, Beijing, China, 2010.

[23] X. Li, J. Liu, A. Liao et al., "Evaluation of measurement errors for eight domestic tipping bucket rain gauges," *Water Resources and Power*, vol. 37, no. 6, pp. 160–163, 2019, in Chinese.

[24] A. Tokay, P. G. Bashor, and V. L. McDowell, "Comparison of rain gauge measurements in the Mid-Atlantic region," *Journal of Hydrometeorology*, vol. 11, no. 2, pp. 553–565, 2010.

[25] V. S. Shedekar, L. C. Brown, M. Heckel et al., "Measurement errors in tipping bucket rain gauges under different rainfall intensities and their implication to hydrologic models," in *Proceedings of the 2009 ASABE Annual International Meeting*, Reno, Nevada, USA, June 2009.

[26] A. Molini, L. G. Lanza, and P. L. Barbera, "The impact of tipping-bucket raingauge measurement errors on design rainfall for urban-scale applications," *Hydrological Processes*, vol. 19, no. 5, pp. 1073–1088, 2005.

[27] D. Yang, B. E. Goodison, J. R. Metcalfe et al., "Quantification of precipitation measurement discontinuity induced by wind shields on national gauges," *Water Resources Research*, vol. 35, no. 2, pp. 491–508, 1999.

[28] M. D. Pollock, G. O'Donnell, P. Quinn et al., "Quantifying and mitigating wind-induced undercatch in rainfall measurements," *Water Resources Research*, vol. 54, no. 6, pp. 3863–3875, 2018.

[29] M. Colli, R. Rasmussen, J. M. Thériault, L. G. Lanza, C. B. Baker, and J. Kochendorfer, "An improved trajectory model to evaluate the collection performance of snow gauges," *Journal of Applied Meteorology and Climatology*, vol. 54, no. 8, pp. 1826–1836, 2015.

[30] V. Nešpor and B. Sevruk, "Estimation of wind-induced error of rainfall gauge measurements using a numerical simulation," *Journal of Atmospheric and Oceanic Technology*, vol. 16, no. 4, pp. 450–464, 1999.

Hindawi
Advances in Meteorology
Volume 2019, Article ID 4942827, 12 pages
https://doi.org/10.1155/2019/4942827

Research Article

The Spatiotemporal Pattern of the Aerosol Optical Depth (AOD) on the Canopies of Various Forest Types in the Exurban National Park: A Case in Ningbo City, Eastern China

Yufeng Chi,[1,2] **Shudi Zuo**,[1,2,3] **Yin Ren**,[1,3] **and Kaichao Chen**[4]

[1]*Key Lab of Urban Environment and Health, Institute of Urban Environment, Chinese Academy of Sciences, Xiamen 361021, China*
[2]*University of Chinese Academy of Sciences, Beijing 100049, China*
[3]*Ningbo Urban Environment Observation and Research Station-NUEORS, Chinese Academy of Sciences, Ningbo 315800, China*
[4]*Ningbo Forest Farm, Ningbo 315000, China*

Correspondence should be addressed to Yin Ren; yren@iue.ac.cn

Received 12 July 2019; Accepted 4 October 2019; Published 30 October 2019

Guest Editor: Salman Tariq

The spatiotemporal distribution pattern of the aerosol optical depth (AOD) is influenced by many environmental factors, such as meteorological condition changes, atmospheric pollution, and topographic changes. Understanding the relationship between the vegetation land cover and the AOD would favor the improvement of forest ecosystem services. This quantitative research integrated remote sensing and ground survey data and used spatial statistical methods to explore the drivers that influence the AOD of the exurban national forest park and analyze the differences between various forest types. The driver analysis was carried out in the hot ($Z \geq 1.64$) and cold ($Z \leq -1.64$) spots of AOD in 2010 and 2017. Our results showed that (1) the forest type was proved to be the main factor contributing to the AOD pattern and (2) from 2010 to 2017, the average growth rate of broad-leaved forest, coniferous forest, bamboo, and shrub in hot spots was significantly higher than that in cold spots, while there was no significant difference in the mixed forest. The average growth rate of biomass densities of bamboo, coniferous forest, and mixed forest were higher than that of the shrub and broad-leaved forest. These findings provided the guidance for the rational allocation of tree species to increase the biomass and improve the ecosystem service values of forest parks.

1. Introduction

There are two major sources of atmospheric aerosol: natural and human emissions, which is a system comprising atmospheric medium with mixed solid and liquid particles. The composition is complex and diverse, including various trace metals, inorganic oxides, sulfates, nitrates, and oxygen-containing organic compounds [1–4]. The composition of the urban atmosphere affected by the various pollution sources changes greatly. However, the composition in the exurbs is relatively stable, which is generally related to the local soil composition. As a crucial natural provider of multiple ecosystem services, the quantitative assessment and improvement measures of exurban national forest parks are of increasing concern to urban managers [5, 6]. Human health and vegetative growth are inevitably affected by aerosols. Aerosols have important effects on air quality, visibility, acid deposition, precipitation, atmospheric radiation balance, and chemical reactions in the stratosphere and troposphere. Thus, understanding the spatiotemporal pattern of the aerosol in the exurban national park and its relationship to the forest type on the ground will be helpful to improve ecological system services provided by the forest.

AOD is an important index of atmospheric turbidity [7, 8]. It has been widely used in related studies to improve air quality because of certain linear relationships with the PM 2.5 concentration on the ground. The smaller the AOD, the cleaner the atmosphere and vice versa. Furthermore, it is vital to study the mechanisms influencing the distribution pattern of aerosols. Previous studies have shown that AOD

may overestimate aerosol concentration when the relative humidity (RH) is higher than 40% and can better reflect dry aerosol concentration when the RH is lower than 40% [9]. Quantitative analysis of influencing factors of aerosol spatial distribution requires the integration of remote sensing images and field surveys to identify influential factors, which have strong effects in clustering regions (hot or cold spots) differentiated by spatial statistical analyses [10–13]. Besides the influence of human activities, the meteorological condition, topography, soil, and forest vegetation also have an interactive impact on aerosol concentration. The relationship between vegetation and aerosol is mainly reflected in the direct and indirect effects of aerosols on plants. The manifestation of direct influence is the aerosol coverage on plant leaves, affecting plant respiration, stomatal conductance, and utilization rate of sunlight. The indirect effect refers to the influences of aerosols on precipitation and temperature of the atmosphere as well as the scattering of sunlight, etc., further resulting in the effects on the utilization of light, water, and heat by plants [14]. Natural and anthropogenic aerosols mixed in the atmosphere mainly have indirect effects on plant growth, but less direct effects. The influence of aerosols on net primary production (NPP) may be positive, neutral, or negative [15]. Although certain concentrations of aerosols inhibit plant growth, the light scattering caused by aerosols disperses direct sunlight to every layer of leaves, including the leaves under canopy. This phenomenon is named as diffusion radiation fertilization effect, which has positive influences on vegetation [16].

At present, the research on the relationship between AOD and plant growth is mainly divided into two spatial scales: the sample scale and a large regional scale [17–19]. Most of the recent studies were based on the quantitative experiment of ground-based remote sensing and the small-scale sample points, where the relationships between the AOD and a particular species or some species were detected by a statistical approach, On small-scale sample points, it has been proved that higher AOD concentration significantly promoted plant growth [20]. A part of the studies used global or large-scale model simulations to measure the effects caused by AOD diffuse radiation and showed that the diffuse radiation improved the efficiency of photosynthesis [21, 22]. However, in order to enhance regional ecosystem service capacity through forest management, these study results may bias the application guidance [23, 24]. On the one hand, sample plots may be difficult to reflect the aggregation effects of different tree species in the forest park on the spatial pattern of aerosol at the regional scale. On the other hand, a wide range of meteorological digital model simulations do not reflect the characteristics of vegetation properties inside the forest park. Furthermore, the AOD spatial resolution of existing satellite remote sensing products are 500 m or coarser, making it difficult to fully describe forest property details [25]. The ground forest management planning inventory (FMPI) data required the remote sensing images with high spatial resolution, such as 30 m, to support the mechanism analysis. In this study, we took the exurban Siming Mountain National Forest Park of Ningbo City in the Yangtze River Delta as an example. To conduct the analysis, we firstly integrated the multisource data composed of the FMPI, Landsat remote sensing data, road network data, meteorological data, and demographic data. Then, we used a geographical detector to analyze the heterogeneity of the AOD spatial-temporal distribution pattern in 2010 and 2017 and its main influencing factors. Finally, a statistical analysis was applied to find the relationship of AOD on different types of forest canopies.

The purpose of this study is to find out the main influencing factors of aerosol distribution in exurban forest parks and to explore the differences in biomass growth of different forest types in aggregation areas with different concentrations. We tried to answer two questions: (1) in addition to human emission sources, what are the main ecological factors influencing exurban forest park AOD? and (2) do the AOD concentrations cause differences in biomass growth rates among different types of forests in the study area? The research results can provide guidance for improving the ecosystem service value of forest parks and provide reference for the further study of mechanisms.

2. Materials and Methods

2.1. Overview. We approached this research in the following steps: First, to create a database that integrates multiple types of GIS and remote sensing (RS) data (including Landsat 8 OLI images, Landsat 7-ETM$^+$ images, FMPI, MODIS data, OpenStreetMap data, and Landscan data). Second, to preprocess the database. There were two substeps included: (1) replenishment of missing remote sensing pixel values, caused by cloud occlusion, through the Kriging interpolation which is a geostatistical method for predicting missing spatial information (AOD, MODIS data) [26, 27] and (2) inversion of the AOD by Landsat data. Third, the hot spots and cold spots of AOD in this area were identified by the high Z values ($Z \geq 1.64$) and low Z values ($Z \leq -1.64$) respectively, which were calculated through global Moran's I and Getis-Ord Gi* [28, 29]. The optimal threshold distance was calculated using the incremental spatial autocorrelation module. Fourth, the factor detector of the Geodetector model was used to quantify the impact contribution of different factors on the AOD. Lastly, we calculated and analyzed the biomass changes of different forest types in cold and hot spots from 2010 to 2017.

2.2. Study Area. Siming Mountain National Forest Park is in Ningbo City, Zhejiang Province, China (Figure 1). The location is longitude 120°59′20″E–121°25′16″E and latitude 29°31′39″N–29°59′20″N. The park is subject to the subtropical monsoon climate, which is characterised by 1,277 km^2, 976 m highest altitude, 77.5% forest coverage, and yellow soil. The annual average temperature is 10oC, and the annual average rainfall is 1,800 mm.

2.3. Multisource Dataset and Preprocessing. Three types of data in two years, which included the year 2010 and 2017, were collected. The first type of data was the Landsat satellite

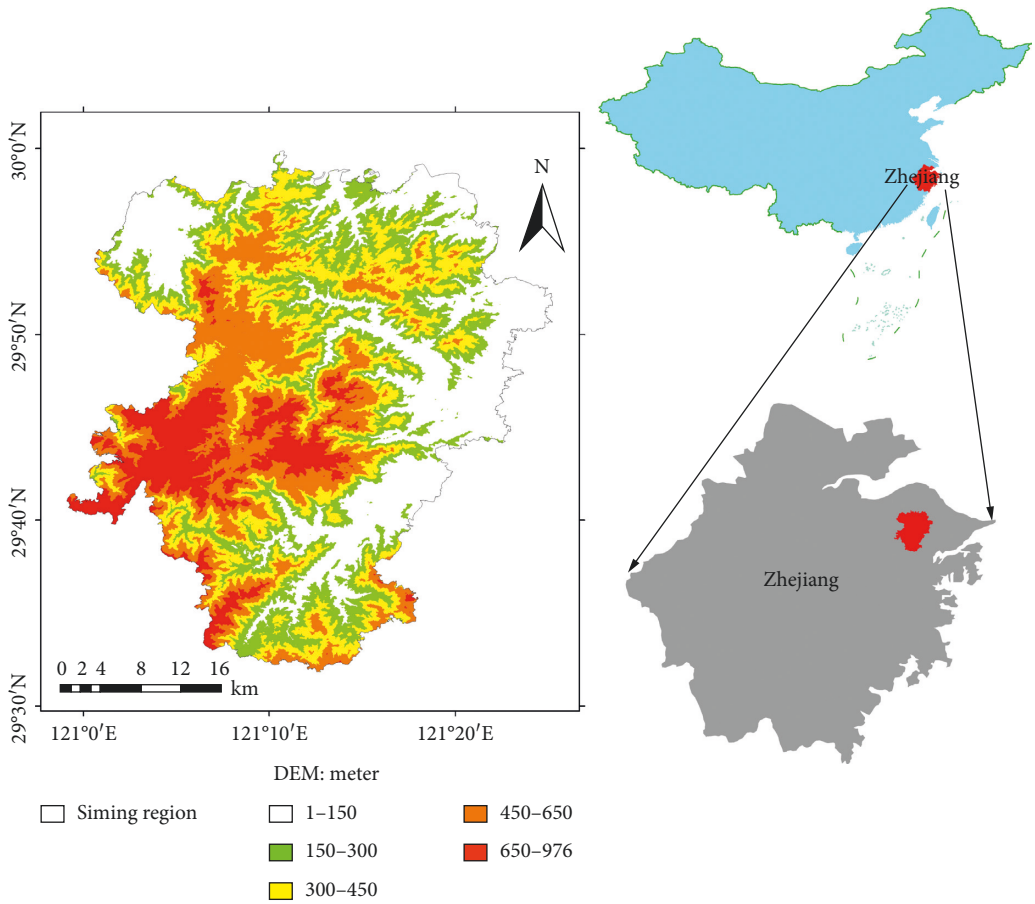

Figure 1: Map of study area. The inset shows the location in China.

remote sensing data for AOD retrieval with a spatial resolution of 30 m. To ensure representation of the data, we selected the two nearest meteorological stations in the China Meteorological Data Network (http://data.cma.cn) (Nos. 58467 and 58562, respectively) to screen for wind speed and air pressure that were within a 5% error limitation of the mean value in both 2010 and 2017. Afterwards, we collected eight remote sensing image data for the four seasons in 2010 and 2017 (row number 118, column number 39). The remote sensing images and data from the four phases of the ETM sensor and the four phases of the OLI sensor were chosen based on the cloud cover percentage. The less cloudy ones were selected, which were the Landsat 7 ETM images on January 1, April 23, July 28, and December 3, 2010, and Landsat 8 OLI image on April 2, August 24, and October 27, 2017, and January 15, 2018 (Table 1). The cloud covers were 0.01%, 6.62%, 24.63%, 0.10%, 0.37%, 0.26%, 14.27%, and 1.27%, respectively. The average wind speeds at the two meteorological stations were (2.1 and 3.2 m/s), (4.1 and 3.1 m/s), (2.1 and 4.7 m/s), (3.6 and 3.5 m/s), (4.2 and 4.1 m/s), (2.2 and 2.3 m/s), (5.1 and 6.1 m/s), and (5.5 and 5.5 m/s) with relative humidity (75 and 77%), (88 and 86%), (90 and 91%), (88 and 85%), (79 and 82%), (85 and 90%), (90 and 90%), and (77 and 78%) in the years 2010 and 2017, correspondingly.

The second type of data was the FMPI, which is obtained from in situ investigation and observation by the national forestry bureau and its affiliations in China. These data provide forest ground survey results on a regional scale. The attribute database contains information on forest patch area, diameter of breast height (DBH), height, canopy, tree density, tree composition, origin, forest management type, volume, forest resource distribution map, etc. The study area includes 20,452 and 53,980 irregular forest patches with the average of 6.499 ± 15.847 (mean ± SD) ha and 2.376 ± 6.784 ha in 2010 and 2017, respectively. The data selected for this research are (1) forest attribute data (age, DBH, dominant species, and species composition), (2) soil data (layer thickness and type), and (3) topographic data (altitude, slope degree, and slope direction). The values of the above data were calculated by averaging values of all units in the forest patches. The tree species of Siming Mountain National Forest Park mainly include *Pinus massoniana*, *Cunninghamia lanceolata*, *Pinus taiwanensis*, *Pinus thunbergii*, *Pinus elliottii*, *Schima superba*, *Liquidambar formosana*, *Phyllostachys heterocycla*, *Dendrocalamopsis oldhami*, *Myrica rubra*, *Eriobotrya japonica*, *Camellia sinensis*, *Morus alba*, and *Camellia oleifera*. According to the dominant species and tree species composition data recorded in each patch, forest types were divided into six categories: coniferous tree,

Table 1: Information about the GIS and RS data in this study.

Type	Data	Time
GIS	FMPI	2010 2016
	OSM	2017
	LSP	2017
RS	Landsat 8 OLI Row 118/path 39	April 2, 2017 August 24, 2017 October 27, 2017 January 15, 2018
RS	Landsat 7 ETM Row 118/path 39	January 1, 2010 April 23, 2010 July 28, 2010 December 3, 2010
	MODIS TPWV MODIS LAI MODIS LST MODIS NDVI MOD04_3K	The time of MODIS data set is the same as that of Landsat data set

broad-leaved tree, mixed coniferous and broad-leaved, bamboo, shrub, and nonforest land (Figure 2).

The third type of data was obtained from open-access resources. It consisted of daily Moderate Resolution Imaging Spectroradiometer (MODIS), total precipitable water vapor (TPWV), daily leaf area index (LAI), daily land surface temperature (LST), 16-day normalised difference vegetation index (NDVI), MODIS Terra Aerosol 5-Min L2 Swath 3 km (MOD04_3K) and Landscan population (LSP) data (https://landscan.ornl.gov/) [30], and OpenStreetMap (OSM) data (https://www.openstreetmap.org) [31]. All data were selected in accordance with the shooting time of the Landsat satellite imagery dataset. Due to cloud problems, some missing pixel values of the MODIS data (TPWV, LAI, LST, and NDVI) were filled by Kriging interpolation [32–35]. Then, the spatial resolution of the whole dataset was resampled to 30 m [36].

2.4. Inversion of the AOD. The atmospheric top radiation captured by satellite sensors is the result of the interaction of electromagnetic waves and the earth's atmospheric system. Atmospheric aerosol remote sensing, which is sensitive to aerosol scattering, depends on the characteristics of the short wavelength of visible light combined with Second Simulation of the Satellite Signal in the Solar Spectrum, 6 S atmosphere transmission model, to realise the inversion [37–39]. Assuming the earth surface to be a Lambert surface, the atmospheric level is uniform, and the apparent atmospheric reflectance (upward reflectance) observed by the satellite is as described in the following equation:

$$\rho_{\mathrm{TOA}}(\theta_s, \theta_v, \varphi) = \rho_0(\theta_s, \theta_v, \varphi) + T(\theta_s)T(\theta_v) \cdot \frac{\rho_s(\theta_s, \theta_v, \varphi)}{[1 - \rho_s(\theta_s, \theta_v, \varphi) \cdot R]}, \quad (1)$$

where θ_s is the solar zenith angle, θ_v is the satellite zenith angle, φ is the azimuth of the scattered radiation from the solar beam, ρ_0 is the path radiance, ρ_s is the angular surface reflectance, R is the atmospheric backscattering ratio, and $T(\theta_s)$ is the normalised downward flux for zero surface reflectance; $T(\theta_v)$ represents upward total transmission into the satellite's field of view.

In this study, we used ENVI software and IDL language to calculate AOD values at 550 nm. The first step was preprocessing of the Landsat images, including masking, radiation calibration, geometric correction, and the calculation of the apparent reflectance (ρ_TOA) of the atmosphere. The second step was inversion of the AOD by using the dark pixel method because of the high vegetation cover of the study area. The detailed processes include four substeps [39, 40]: (1) the dark pixels, which are usually in the dense vegetation covered areas with short wavelength and dark surface, were identified by the NDVI; (2) since the apparent reflectance of 2.1-2.2 μm wavelength is almost independent of aerosol [41–43], the short infrared band was chosen to calculate the surface reflectance; (3) the optimal AOD was determined by matching the 6 S LookUp Table (LUT) and apparent reflectance and the mean AOD mean values of red and blue band were obtained; (4) the Kriging interpolation was applied to the preliminary inversion results which were resampled to 30 m [44]; and (5)the AOD inversion results in this study were compared with MOD04_3K data to verify the inversion accuracy. In our study, For this substep, we firstly registered Landsat AOD and MOD04_3K data which were taken at the same time (two sets of data at the same time), then calculated the average value of the corresponding mesh of Landsat AOD according to the mesh size of MOD04_3K, counted the number of effective pixels, and finally counted the linear regression equation and R^2.

2.5. Statistical Method

2.5.1. Spatial Statistical Analysis. Two mean AOD spatial distribution maps were mapped based on the calculation of the average of each pixel of four AOD images in 2010 and 2017, respectively. The Getis-Ord G_i^* method effectively

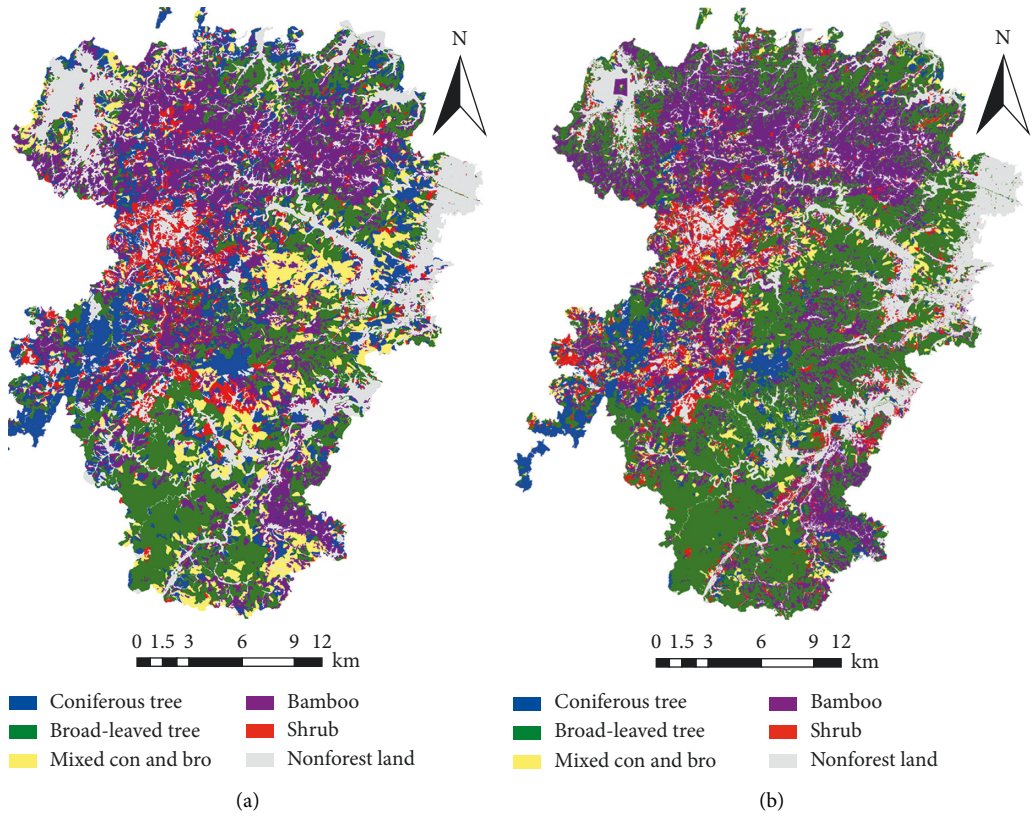

Figure 2: Forest types of the Siming Mountain National Forest Park in (a) 2010 and (b) 2017.

identified the statistically significant aggregation areas (e.g., hot spots representing the position with the high AOD concentrations ($p < 0.05$) and cold spots representing low AOD concentrations ($p < 0.05$)) [40], which is popular in spatial analysis [41, 42]. Moreover, we evaluated the AOD autocorrelation pattern by the Moran I index. The Getis-Ord Gi* demands optimal threshold distances for clustering. Therefore, we used the incremental spatial autocorrelation module to determine the optimal distance threshold, which is required, by increasing the threshold distance from 200 to 4,000 m at the interval of 200 m until it reached its maximum value (2,200 m) [43]. The distance was calculated using the Euclidean distance.

2.5.2. Geodetector Model. The Geodetector is a statistical tool for detecting spatially stratified heterogeneity and revealing the contribution of factors to the heterogeneity [44]. In this study, we used the factor detector (FD) module of this model to assess the explanation powers of the park features (e.g., tree species and NDVI), the topography (e.g., altitude, slope degree, and slope aspect), the soil (e.g., soil type and thickness), the human activity (e.g., road length and population density), and the meteorology (e.g., temperature and evaporation) on the AOD. The contribution power can be expressed using the following equation:

$$q = 1 - \frac{\sum_{h=1}^{L} N_h \sigma_h^2}{N_{\sigma^2}} = 1 - \frac{\text{SSW}}{\text{SST}}, \quad (2)$$

where $q \in (0,1)$ is the impact power of the independent variable on the dependent variable 1, 2, 3, . . ., L, L is a strata of dependent or independent variables; stratum h is composed of N_h unit; σ_h^2 is the variance of AOD in the same stratum; N is the number of FMPI patches; σ^2 is the variance of the AOD in the entire region; N is the number of FMPI patches in the same stratum; SSW is the within sum of squares; and SST is the total sum of squares. The larger the q value is, the greater the similarity between independent factors and AOD.

2.5.3. Statistical Analysis. The independent sample T test was used to analyze the difference of biomass growth rate of different forest types in cold and hot spots from 2010 to 2017. The system clustering was used to classify the differences of independent variables.

To ensure that the analysis of biomass growth rate is not affected by seedling plantation or forest fire, we selected forest patches with biomass growth from 2010 to 2017. Moreover, we also screened the forest patches with the same forest type in both years in order to reduce statistical errors.

2.6. Biomass Estimation. The biomass is an important indicator to evaluate the quality of forest park because it is a fundamental factor in evaluating plant growth. The Volume-Biomass Compatibility Model (VBCM) was used to estimate individual tree biomass by tree height, the DBH, and the

coefficients [45–48]. The forest biomass density was inferred from the number of trees and the area of forest patches recorded by the FMPI. Although there were errors in estimating regional biomass by inference, it would not significantly influence the analysis result because the growth rate was the ratio of the regional biomass estimates in the two years. The formula is shown in the following equation:

$$W = aD^k H^j \times \frac{\text{numtree}}{A}, \quad (3)$$

where W is the biomass density (t/ha); a, k, and j are the coefficients; D is the DBH (cm); H is the tree height (m); numtree is the number of patch plants; and A is the area (ha). Dominant tree species and forest composition were recorded in the FMPI using the coefficients of the dominant tree species (*Cunninghamia lanceolate*, *Phyllostachys heterocycle*, *Schima superba*, and *Camellia oleifera*) [47, 49, 50] in Table 2 to calculate the biomass.

Table 2: Coefficients of different dominant tree species in the VBCM.

Tree species (dominant species)		a	k	j
Coniferous	*Cunninghamia lanceolata*	0.0811	1.6942	0.8472
Bamboo	*Phyllostachys heterocycla*	66.9197	2.5500	0.0437
Broad-leaved	*Schima superba*	0.2993	1.8530	0.2774
Shrub	*Camellia oleifera*	0.1510	2.0170	0.0000

3. Results

3.1. AOD Distribution and Various Forest Types Spatial Statistical Result in Siming Mountain National Forest Park. As shown in Figure 3, there were 717 and 718 verification points in the 2010 and 2017 images of Landsat AOD paired with MOD04_3K, respectively, and R2 was 0.752 and 0.724. These outcomes proved that the inversion results of Landsat AOD are reliable.

From 2010 to 2017, the annual average AOD decreased from 0.567 to 0.292 with a change in tree species distribution. Specifically, from the proportion of tree species distribution aspect, the area proportional to broad-leaved forest increased greatly (from 24.49% to 42.58%). The area proportion of nonforest land, coniferous forest, mixed coniferous, and broad-leaved forest decreased significantly (from 21.38%, 15.57%, and 9.06% to 16.2%, 6.29%, and 4.14%, respectively), while bamboo (from 23.01% to 23.90%) and shrub (from 6.49 to 6.89%) showed a slight increase. The aggregation degree of AOD distribution decreased in terms of Moran's I, which was 0.348 and 0.177 in the two years, respectively (Table 3).

The average AOD of the cold and hot spots area in 2010 was significantly different from that in 2017 (Figure 4).The cold spot area increased significantly from 18,119.64 ha to 41,924.62 ha with a decrease in the average AOD from 0.39 to 0.16. While the hot spot area decreased from 57,964.31 ha to 26,706.11 ha with a decrease in the average AOD from 0.69 to 0.52. From the five regions marked in Figure 4, we found the five regions with great changes, including the 1st (north), 3rd (west), and 5th (east) regions where the cold spots areas increased significantly. In 2017, the 2nd and the 4th regions where the hot spots areas increased as well, but with a lower AOD than in 2010.

The 10,178 forest patches of cold spots and the 10,581 forest patches of hot spots were selected based on the screening principle in the overlapped regions of cold and hot spots in 2010 and 2017. The area proportion of the various forest types in cold and hot spots area varied dramatically (Table 4). The broad-leaved forests and bamboo accounted for the largest areas in the cold spots. Specifically, the percentages of broad-leaved forests and bamboo were 18.28% and 15.15% larger than in the hot spots. In the hot spots, the nonforest land was larger than in the cold spots. Moreover, the proportion of the coniferous forest, shrub, mixed forest, and nonforest land was 5.19%, 7.30%, 8.60%, and 13.15% higher than in cold spots, respectively.

3.2. 2010 and 2017 Factor Detector Results of Geodetector Model. The forest type played the most important role in both cold and hot spots during the two years. In the year of 2010, temperature (0.0301 and 0.0159) and NDVI (0.0257 and 0.0354) ranked second and third in both cold and hot spots. In the year of 2017, the second and third important factors were the Landscan population density (0.0189) and the OSM road length (0.0195) in hot spots and the NDVI (0.0204) and Landscan population density (0.0201) in cold spots. In the two-year average, the followers were the OSM road length (0.0234) and NDVI (0.0158) in the hot spots and the NDVI (0.0273) and slope (0.0064) in the cold spots. The forest type and other factors were classified into two clusters through the hierarchical cluster analysis (Table 5).

3.3. Biomass Variations and Growth Rates of Various Forest Types in 2010 and 2017. Analysis of samples from the broad-leaved forest, shrub, coniferous and broad-leaved mixed forest, coniferous forest, and bamboo were in the number of 385, 214, 31, 196, and 63 patches in the hot spots and 596, 88, 22, 191, and 239 patches in the cold spots, respectively.

In 2010, there was no significant difference between the biomass densities of different forest types in the hot and cold spots. The average biomass densities of the broad-leaved forest, mixed forest, coniferous forest, bamboo, and shrub in the hot spots were 142.82 t/ha, 126.57 t/ha, 102.11 t/ha, 51.82 t/ha, and 38.25 t/ha, and in the cold spots, 143.18 t/ha, 128.14 t/ha, 100.68 t/ha, 51.53 t/ha, and 36.26 t/ha, respectively.

However, in 2017, the biomass density differences were significant between the hot and cold spots ($p < 0.01$) for all of the forest types except for the mixed forest. The biomass densities of these five forest types were 187.09 t/ha, 158.21 t/ha, 152.14 t/ha, 80.8 3 t/ha, and 49.34 t/ha for the broad-leaved forest, mixed forest, coniferous forest, bamboo, and shrub in the hot spots; 181.84 t/ha, 161.45 t/ha, 141.96 t/ha, 75.23 t/ha, and 43.87 t/ha of them were in the cold spots, respectively.

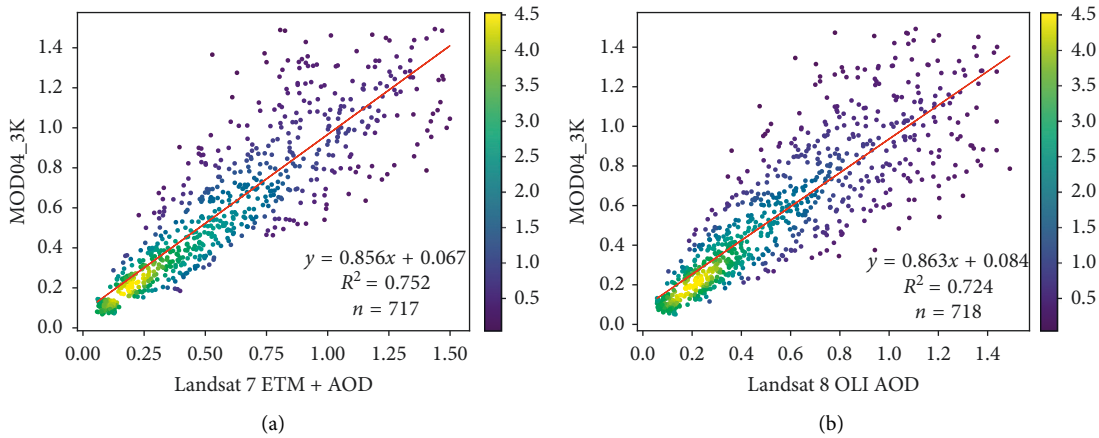

Figure 3: Verification results of Landsat AOD and MOD04_3K data. (a) 2010. (b) 2017. The color bars represent the counts of points. The red solid line represents the regression line.

Table 3: Results of Moran's I.

Year	2010	2017
Moran's I	0.348**	0.177**
Z-score	98.157	52.983
Pattern	Aggregated	Aggregated

Note. **The significant value ($p < 0.01$).

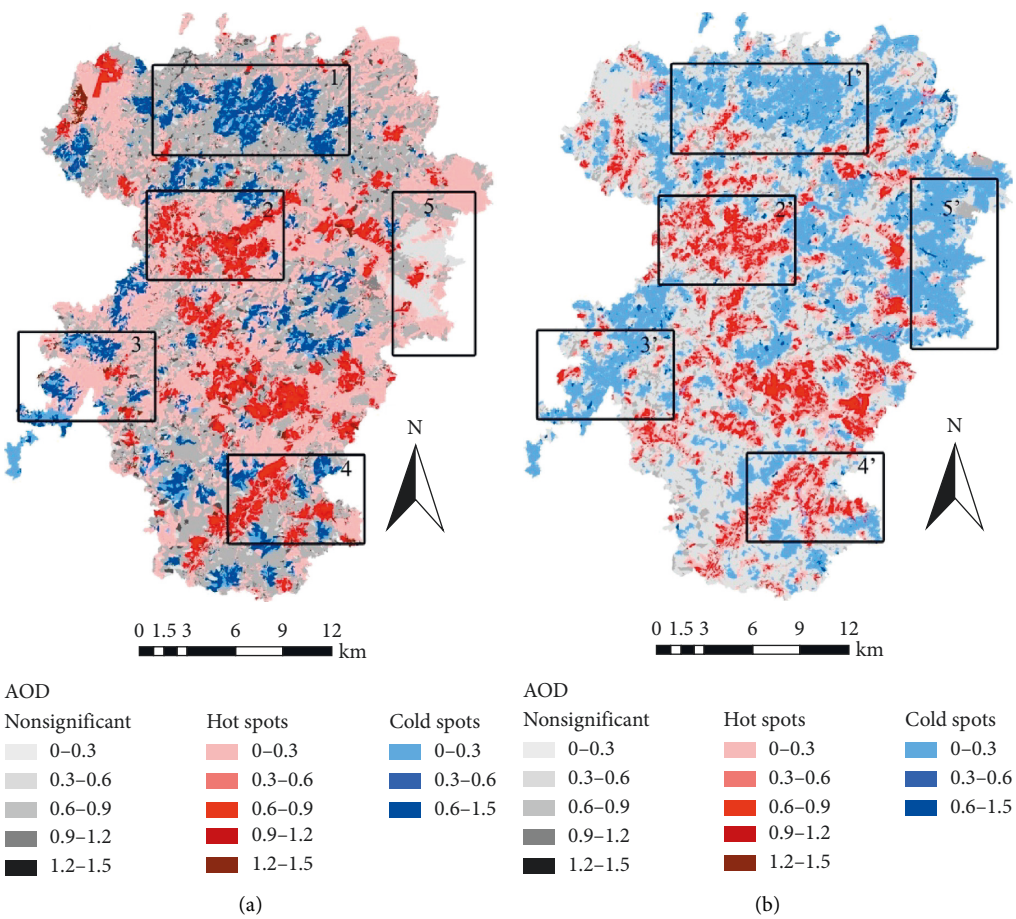

Figure 4: Cold and hot spots of the AOD spatial distribution maps in (a) 2010 and (b) 2017. The regions with 1–5 indicate great changes in hot and cold spots.

Table 4: Area proportion of different forest types in the overlapped cold and hot spots in 2010 and 2017.

%	Coniferous forest	Broad-leaved forest	Shrub	Nonforest	Bamboo	Con and bro mixed forest	Total
Cold spots	3.80	50.50	3.00	1.80	39.80	1.10	100.00
Hot spots	9.09	32.22	10.30	14.95	24.75	9.70	100.00

Con and bro mixed forest = coniferous and broad-leaved mixed forest.

Table 5: The results of different factors through FD and cluster analysis in 2010, 2017 and the two periods' average.

Factors	2010		2017		Two periods' average		Hierarchical cluster
	Hot spots	Cold spots	Hot spots	Cold spots	Hot spots	Cold spots	
TSY	0.1248**	0.1196**	0.1389**	0.1450**	0.1569**	0.1735**	1
NDVI	0.0257**	0.0354**	0.0146**	0.0204**	0.0158**	0.0273**	2
LST	0.0301**	0.0159**	0.0101**	0.0095**	0.0094**	0.0057**	2
TPWV	0.0009**	0.0008**	0.0011**	0.0012**	0.0005**	0.0027**	2
ST	0.0099**	0.0121**	0.0115**	0.0141**	0.0093**	0.0051**	2
SLT	0.0085**	0.0099**	0.0054**	0.0021**	0.0056**	0.0027**	2
AT	0.0114**	0.0089**	0.0021**	0.0012**	0.0078**	0.007**	2
SL	0.0088**	0.0066**	0.0025**	0.0045**	0.0098**	0.0058**	2
SD	0.0027**	0.0056**	0.0077**	0.0096**	0.0025**	0.0064**	2
LSP	0.0012**	0.0098**	0.0189**	0.0201**	0.0029**	0.0003**	2
OSM	0.0012**	0.0083**	0.0195**	0.0055**	0.0234**	0.0017**	2

Note. p values for all areas are <0.01 in 2010, 2017, and the two-year average. **High significance ($p < 0.001$). TSY = tree species type; ST = soil type; SLT = soil layer thickness; AT = altitude; SL = slope; SD = slope direction; LSP = Landscan population; OSM = OSM road length.

Comparing the growth rate of biomass density in different forest types from 2010 to 2017 (Figure 5), the order of average biomass growth rate was bamboo > coniferous forest > broad-leaved forest > shrub > mixed forest in hot spots. In cold spots, the order of average biomass growth rate was bamboo > coniferous forest > mixed forest > broad-leaved forest > shrub. The average ages of the broad-leaved forest, the mixed forest, the coniferous forest, the bamboo, and the shrub increased from 15.42 ± 2.16 to 15.84 ± 2.31 (mean ± SD), 14.88 ± 2.55 to 15.27 ± 2.78, 9.01 ± 1.25 to 9.25 ± 1.12, 3.18 ± 0.97 to 3.51 ± 0.98, and 2.11 ± 0.88 to 2.44 ± 0.85, respectively. Except for the mixed forest, the growth rate of biomass densities of the four other forest types were significantly higher in hot spots than in cold spots ($p < 0.01$). The growth rate of biomass density of the mixed forest in cold spots was higher than that in hot spots, but not significant.

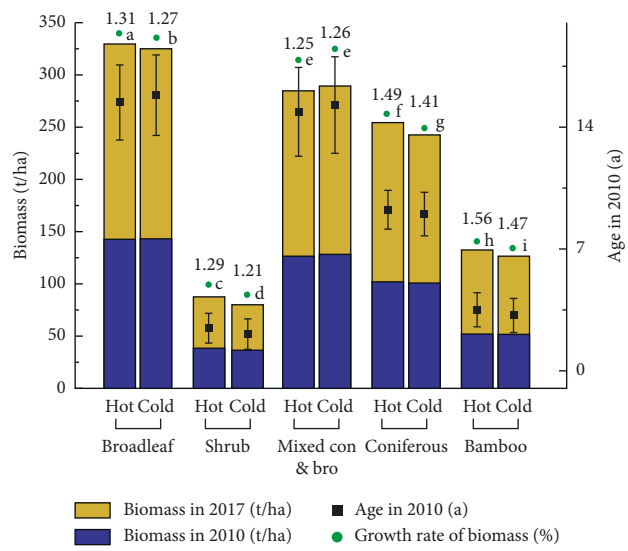

Figure 5: Biomass and biomass growth rates of different forest types in 2010 and 2017 (age and SD in 2010). The different letters indicate significant differences in the biomass increase rate between forest types at $p < 0.05$.

4. Discussion

The exploration of the impact factors of aerosol spatial distribution and the influences of AOD on the canopies of different forest types in the exurbs of cities encourage forest managers to improve the ecosystem service level. This study used multisource data, which included high-resolution remote sensing images and detailed ground investigation data to discover if the type of tree species is the one of the main factors affecting the AOD concentration difference in Siming Mountain Forest Park. We observed the impacts of AOD concentration on the growth of different tree species in the forest park, which supplemented the evidence of the relationship between AOD spatial distribution and the forest on a regional scale.

4.1. Relationship between Different Forest Types and AOD Distribution in the National Park. Siming Mountain Forest Park is located near the east coast of China, with a high forest coverage rate far from the urban center. The variation of AOD values may be caused by the combined action of moisture and particulate matter. In order to minimize the influence of water vapor, we selected eight remote sensing images taken during good and stable weather conditions between 10 : 00 and 11 : 00 am to avoid the condensation of water vapor caused by low temperature in the morning,

although the average value of AOD in the study area is low. The AOD is the integral of the extinction coefficient of the medium in the vertical direction, which reflects the comprehensive effect of atmospheric scattering and surface reflection. We cannot distinguish the aerosol types. Based on the analysis of aerosol sources in four forest areas in Sichuan Province, China, it was found that the aerosols were mainly from local primary emission sources such as crust dust and biomass combustion, followed by the long distance transmission of aged organic aerosols (aged OOA) [51]. In addition to soil dust, meteorology, and human activities, plant species was also an important factor for the AOD variation in forest areas. The reactivity of plant VOCs with oxidants (such as OH, NO_3 free radical, and O_3) was higher than that of artificial VOCs, resulting in the generation of secondary organic aerosols (SOA). Zhu et al. (2017) found that the main source of SOA at the top of the exurban Tai Mountain in China was from an artificial source (11.6–42.6%), such as the use of solvents, fuel combustion, and vehicle exhaust as well as the biological source (6.5%) such as secondary oxidation and biomass burning [52]. However, the source of a large proportion of SOA was not identified. Although plants contribute to the generation of aerosols, the underlying surface of forest cover affects the physical processes in the atmospheric boundary layer. The high vegetation coverage increases the friction between the air and the ground, reduces wind speed, and diminishes transmission of pollutants from the ground and over long distances.

The results of the Geodetector and cluster analysis in the cold and hot spots of this study in two years showed that the forest type was the main factor affecting AOD distribution in the exurban forest park, followed by NDVI and temperature. In the cold spots, more than half of the area was broad-leaved forest, while the percentage of broad-leaved forest decreased and the proportion of nonforest land area augmented in the hot spots. The result is similar to that of Deng et al. [53]. The maximized dust retention ability of the coniferous leaf for a single tree is higher than the broad-leaved tree species. However, there are many factors that influence the total dust retention quantity of the forest. As to the specific forest type, in addition to the blade characteristics, the factors influencing tree growth, such as temperature, humidity, soil nutrient, precipitation, and illumination, may affect the stand of leaf area index, thus further modifying the function of particulate matter retention. Moreover, the microstructure of the leaf surface is conducive to the deposition of particulate matter [54]. The forest increases the intensity of end flow in the surface atmosphere, thereby accelerating the deposition rate of particulate matter [55, 56]. Meanwhile, vegetation effectively absorbs pollutants such as SO_2, NO_x, and O_3 in the air in favor of reducing the formation of secondary aerosols [51, 57]. In addition, the large amount of the particle matter in the air can be trapped on the leaf surface as compared to the small amount trapped in the leaf epidermal wax layer [58, 59]. The delayed particulate matter on the leaf surface is eluted to the ground with the precipitation leading to the recovery of its retention ability [60].

From the perspective of the impact of aerosols on plants, the concentration threshold reversed the impact of aerosols on photosynthesis above which the net radiation (direct + scattering) effect of atmospheric aerosols would reduce the photosynthetic absorption of plants [61]. Xu quantified the AOD threshold of the impact of aerosol net radiation effect on ecosystem NPP in different regions of China and found that when the AOD was less than 1.5 at 550 nm in the southeast region, the aerosol net radiation effect increased NPP [16]. In this study, the average AOD value in hot spots was much lower than the threshold, and the results were in line with expectations. For example, the growth rate of tree species in hot spots was generally faster than that in cold spots. The average growth rates of the coniferous forest, broad-leaved forest, shrubs, and bamboos in cold spots were significantly different than in hot spots. The reason may be the diffusion radiation fertilization effect mentioned in the introduction, which increases the NPP and promotes growth in hot spots. However, there was not a significant difference in the growth rate of the coniferous broad-leaved mixed forest. The reason may be the large age variation between different tree species (large SD), which induced the different effects of diffusion radiation fertilization on tree species of different ages. The results of this study were consistent with other studies and verified the diffusion radiation fertilization effect at the regional forest park scale.

4.2. Limits and Prospects. There are two limitations in this study. First, the change of AOD is continuous with time. Landsat remote sensing satellite image data (a scene every 16 days) only obtains instantaneous information of the environment. Although the average value of four specific periods throughout the year was used as the research object in this study, the representativeness of inversion results still needs to be considered. At present, ground-based remote sensing and monitoring technologies represent the distribution of sample points and have the ability to obtain series time resolution data. Statistical analyses or machine learning algorithms could be used to obtain the relationships between the sample plot and the surface data. The scale expansion analysis based on multisource data fusion technology could be a solution to explore the mechanism of the aerosol characteristics in forest regions affected by the microclimate. Second, the research area was in the developed area of southeastern China. During the period of economic development from 2010 to 2013, many local residents engaged in the planting of flower and tree seedlings for economic benefits, resulting in a large amount of deforestation. From 2013 to 2017, the local government invested 150 million Yuan to restore 226,637 ha of forest area in order to restore the forest ecological service level. Large areas of land were affected by human disturbance in a short time, which may affect the formation of aerosols in the air. Although rigorous screening criteria were set up to ensure the accuracy of forest type classification, the flow feature of aerosols cannot exclude the influence of other disturbances.

In addition, this study has additional advantages. High-resolution AOD inversion data and detailed comprehensive ground forest resource survey data not only accurately depicted the spatial heterogeneity of the research objects but also explored the impact of different forest attributes on spatial heterogeneity. On the basis of integrating multi-source data, the effect of diffusion radiation fertilization on regional forest park scale was verified, and the relationship between forest type and AOD concentration was discussed.

5. Conclusion

This study overcame the low resolution of AOD remote sensing products and the unavailability problem of the forest vegetation vertical structure information from the optical remote sensing data by the use of high-resolution Landsat and ground survey data of forest resources. We analyzed the AOD spatial-temporal distribution pattern and its main influencing factors and explored the relationship of different types of forest canopies at the regional scale. It was found that the AOD distribution in the study area was clustered, and the forest type was one of the main impact factors. From 2010 to 2017, the average growth rate of broad-leaved forest, coniferous forest, bamboo, and shrub in hot spots was significantly higher than that in cold spots, while there was not a significant difference in mixed forests. The average growth rate of biomass in the cold and hot spots was higher in bamboo, coniferous forest, and mixed forest than in shrub and broad-leaved forest. In summary, at the regional forest park scale, the vegetation type had the closest interaction with AOD. The research results provide the guidance for the rational allocation of tree species to improve biomass and ecosystem service value of the exurban forest park.

Data Availability

The meteorological observation data were supplied by the National Meteorological Information Center (http://data.cma.cn/) under license and so cannot be made freely available. The ground forest management planning inventory (FMPI) data which are obtained from the Forestry Bureau of Zhejiang Province and so cannot be made freely available. The MODIS and LandSat data are provided in the site of USGS (https://www.usgs.gov/). Landscan population (LSP) data are provided in the site of ORNL (https://landscan.ornl.gov/), and OpenSstreetMap (OSM) data are provided in the site of OSMF (https://www.openstreetmap.org).

Conflicts of Interest

The authors declare that there are no conflicts of interest.

Acknowledgments

This work was supported by the National Key Research Program of China (2016YFC0502704), National Natural Science Foundation of China (31670645, 31470578, 31200363, 41801182, 41771462, and 41807502), National Social Science Fund of China (17ZDA058), Fujian Provincial Department of S&T Project (2016T3032, 2016T3037, 2018T3018), Key Program of the Chinese Academy of Sciences (KFZDSW-324) and Ningbo Public Welfare Project (2009c10056).

References

[1] O. Dubovik, B. Holben, T. F. Eck et al., "Variability of absorption and optical properties of key aerosol types observed in worldwide locations," *Journal of the Atmospheric Sciences*, vol. 59, no. 3, pp. 590–608, 2002.

[2] S. K. Friedlander, "Smoke, dust and haze: fundamentals of aerosol behavior," *Physics Today*, vol. 333, 1977.

[3] B. N. Holben, T. F. Eck, I. Slutsker et al., "AERONET-A federated instrument network and data archive for aerosol characterization," *Remote Sensing of Environment*, vol. 66, no. 1, pp. 1–16, 1998.

[4] M. Mc and H. Peter, "A review of atmospheric aerosol measurements," *Atmospheric Environment*, vol. 34, pp. 1959–1999, 2000.

[5] L. M. Hildemann, G. R. Markowski, and G. R. Cass, "Chemical composition of emissions from urban sources of fine organic aerosol," *Environmental Science & Technology*, vol. 25, no. 4, pp. 744–759, 1991.

[6] Y. C. Chan, R. W. Simpson, G. H. McTainsh, P. D. Vowles, D. D. Cohen, and G. M. Bailey, "Characterisation of chemical species in PM2.5 and PM10 aerosols in Brisbane, Australia," *Atmospheric Environment*, vol. 31, no. 22, pp. 3773–3785, 1997.

[7] T. F. Eck, B. N. Holben, J. S. Reid et al., "Wavelength dependence of the optical depth of biomass burning, urban, and desert dust aerosols," *Journal of Geophysical Research: Atmospheres*, vol. 104, no. D24, pp. 31333–31349, 1999.

[8] M. Sato, J. E. Hansen, M. P. McCormick, and J. B. Pollack, "Stratospheric aerosol optical depths, 1850-1990," *Journal of Geophysical Research*, vol. 98, no. D12, pp. 22987–22994, 1993.

[9] J. Quan, C. Jiang, J. Xin et al., "Evaluation of satellite aerosol retrievals with in situ aircraft and ground measurements: contribution of relative humidity," *Atmospheric Research*, vol. 212, pp. 1–5, 2018.

[10] J. Barrell and J. Grant, "Detecting hot and cold spots in a seagrass landscape using local indicators of spatial association," *Landscape Ecology*, vol. 28, no. 10, pp. 2005–2018, 2013.

[11] Y. Ren, L.-Y. Deng, S.-D. Zuo et al., "Quantifying the influences of various ecological factors on land surface temperature of urban forests," *Environmental Pollution*, vol. 216, pp. 519–529, 2016.

[12] S. Zuo, S. Dai, X. Song et al., "Determining the mechanisms that influence the surface temperature of urban forest canopies by combining remote sensing methods, ground observations, and spatial statistical models," *Remote Sensing*, vol. 10, no. 11, p. 1814, 2018.

[13] V. Bernardoni, G. Calzolai, F. Lucarelli et al., "High time-resolved measurements of fine aerosol (PM2. 5) in a hot-spot area during wintertime: multi-wavelength optical absorption properties and source apportionment," in *Proceedings of the EAC Symposium*, Arusha, Tanzania, 2016.

[14] J. T. Randerson, M. V. Thompson, T. J. Conway, I. Y. Fung, and C. B. Field, "The contribution of terrestrial sources and sinks to trends in the seasonal cycle of atmospheric carbon dioxide," *Global Biogeochemical Cycles*, vol. 11, no. 4, pp. 535–560, 1997.

[15] D. S. Cohan, J. Xu, R. Greenwald, M. H. Bergin, and W. L. Chameides, "Impact of atmospheric aerosol light

scattering and absorption on terrestrial net primary productivity," *Global Biogeochem Cy*, vol. 16, 2002.

[16] X. Yue and N. Unger, "Aerosol optical depth thresholds as a tool to assess diffuse radiation fertilization of the land carbon uptake in China," *Atmospheric Chemistry and Physics*, vol. 17, no. 2, pp. 1329–1342, 2017.

[17] J. Proctor, S. Hsiang, J. Burney, M. Burke, and W. Schlenker, "Estimating global agricultural effects of geoengineering using volcanic eruptions," *Nature*, vol. 560, no. 7719, pp. 480–483, 2018.

[18] A. Knohl and D. D. Baldocchi, "Effects of diffuse radiation on canopy gas exchange processes in a forest ecosystem," *Journal of Geophysical Research-Biogeosciences*, vol. 113, 2008.

[19] G. G. Cirino, R. A. F. Souza, D. K. Adams, and P. Artaxo, "The effect of atmospheric aerosol particles and clouds on net ecosystem exchange in the Amazon," *Atmospheric Chemistry and Physics*, vol. 14, no. 13, pp. 6523–6543, 2014.

[20] X. Wang, J. Wu, M. Chen et al., "Field evidences for the positive effects of aerosols on tree growth," *Global Change Biology*, vol. 24, no. 10, pp. 4983–4992, 2018.

[21] K. D. Kanniah, J. Beringer, P. North, and L. Hutley, "Control of atmospheric particles on diffuse radiation and terrestrial plant productivity," *Progress in Physical Geography: Earth and Environment*, vol. 36, no. 2, pp. 209–237, 2012.

[22] A. Rap, D. V. Spracklen, L. Mercado et al., "Fires increase Amazon forest productivity through increases in diffuse radiation," *Geophysical Research Letters*, vol. 42, no. 11, pp. 4654–4662, 2015.

[23] H. Mo, L. Li, W. Lai et al., "Characterization of summer PM2.5 aerosols from four forest areas in Sichuan, SW China," *Particuology*, vol. 20, pp. 94–103, 2015.

[24] M. Pullman, *Conifer PM2. 5 Deposition and Resuspension in Wind and Rain Events*, Cornell University, Ithaca, NY, USA, 2008.

[25] G. Yun, S. Zuo, S. Dai et al., "Individual and interactive influences of anthropogenic and ecological factors on forest PM2.5 concentrations at an urban scale," *Remote Sensing*, vol. 10, no. 4, p. 521, 2018.

[26] Y. Wang, Q. Yuan, T. Li, H. Shen, L. Zheng, and L. Zhang, "Evaluation and comparison of MODIS Collection 6.1 aerosol optical depth against AERONET over regions in China with multifarious underlying surfaces," *Atmospheric Environment*, vol. 200, pp. 280–301, 2019.

[27] Y. Wang, Q. Yuan, T. Li, H. Shen, L. Zheng, and L. Zhang, "Large-scale MODIS AOD products recovery: spatial-temporal hybrid fusion considering aerosol variation mitigation," *ISPRS Journal of Photogrammetry and Remote Sensing*, vol. 157, pp. 1–12, 2019.

[28] A. Getis and J. K. Ord, "The analysis of spatial association by use of distance statistics," *Geographical Analysis*, vol. 24, no. 3, pp. 189–206, 1992.

[29] J. K. Ord and A. Getis, "Local spatial autocorrelation statistics: distributional issues and an application," *Geographical Analysis*, vol. 27, no. 4, pp. 286–306, 1995.

[30] B. Bhaduri, E. Bright, P. Coleman, and J. Dobson, "LandScan: locating people is what matters," *Geoinformatics*, vol. 5, pp. 34–37, 2002.

[31] M. Haklay and P. Weber, "Openstreetmap: user-generated street maps," *IEEE Pervasive Computing*, vol. 7, no. 4, pp. 12–18, 2008.

[32] Q. Wang, W. Shi, P. M. Atkinson, and Y. Zhao, "Downscaling MODIS images with area-to-point regression kriging," *Remote Sensing of Environment*, vol. 166, pp. 191–204, 2015.

[33] C. Yu, L. F. Chen, L. Su, M. Fan, and S. S. Li, "Kriging interpolation method and its application in retrieval of MODIS aerosol optical depth," in *Proceedings of the 2011 19th International Conference on Geoinformatics*, Shanghai, China, 2011.

[34] D. Hu, H. Shu, H. Hu, and J. Xu, "Spatiotemporal regression Kriging to predict precipitation using time-series MODIS data," *Cluster Computing*, vol. 20, no. 1, pp. 347–357, 2017.

[35] T. Hengl, G. B. M. Heuvelink, M. Perčec Tadić, and E. J. Pebesma, "Spatio-temporal prediction of daily temperatures using time-series of MODIS LST images," *Theoretical and Applied Climatology*, vol. 107, no. 1-2, pp. 265–277, 2012.

[36] J. Yang and M. Hu, "Filling the missing data gaps of daily MODIS AOD using spatiotemporal interpolation," *Science of The Total Environment*, vol. 633, pp. 677–683, 2018.

[37] Q. Xiao, H. Zhang, M. Choi et al., "Evaluation of VIIRS, GOCI, and MODIS Collection 6 AOD retrievals against ground sunphotometer observations over East Asia," *Atmospheric Chemistry and Physics*, vol. 16, no. 3, pp. 1255–1269, 2016.

[38] H. Jethva, S. K. Satheesh, and J. Srinivasan, "Assessment of second-generation MODIS aerosol retrieval (Collection 005) at Kanpur, India," *Geophysical Research Letters*, vol. 34, 2007.

[39] R. C. Levy, L. A. Remer, J. V. Martins et al., "Evaluation of the MODIS aerosol retrievals over ocean and land during CLAMS," *Journal of the Atmospheric Sciences*, vol. 62, no. 4, pp. 974–992, 2005.

[40] J. Eck, S. Chainey, J. Cameron, and R. Wilson, "Mapping crime: understanding hotspots," *British Journal of Surgery*, vol. 5, 2005.

[41] C. Kara and N. Akçit, "Traffic accident analysis using GIS: a case study of Kyrenia City," in *Proceedings of the Third International Conference on Remote Sensing and Geoinformation of the Environment (RSCy2015*, p. 953514, Paphos, Cyprus, March 2015.

[42] Z. Mei, S. Xu, and J. Ouyang, "Spatio-temporal association analysis of county potential in the Pearl River Delta during 1990–2009," *Journal of Geographical Sciences*, vol. 25, no. 3, pp. 319–336, 2015.

[43] T. J. Stopka, C. Krawczyk, P. Gradziel, and E. M. Geraghty, "Use of spatial epidemiology and hot spot analysis to target women eligible for prenatal women, infants, and children services," *American Journal of Public Health*, vol. 104, no. S1, pp. S183–S189, 2014.

[44] J.-F. Wang, T.-L. Zhang, and B.-J. Fu, "A measure of spatial stratified heterogeneity," *Ecological Indicators*, vol. 67, pp. 250–256, 2016.

[45] W. S. Zeng, "Developing tree biomass models for eight major tree species in China," in *Biomass Volume Estimation and Valorization for Energy*, IntechOpen, London, UK, 2017.

[46] W.-S. Zeng and S.-Z. Tang, "Modeling compatible single-tree aboveground biomass equations for masson pine (*Pinus massoniana*) in southern China," *Journal of Forestry Research*, vol. 23, no. 4, pp. 593–598, 2012.

[47] F. M. Cao, *Biomass and Carbon Storage of Bamboo Forest Ecosystem in Taojiang*, Central South University of Forestry and Technology, Changsha, Hunan, China, 2017.

[48] J. Zhang, H. D. Gao, B. G. Ying et al., "The biomass dynamic analysis of public walfare forest in Xianju county of Zhejiang province (in Chinese)," *Journal of Nanjing Forestry University Natural Science Edition*, vol. 35, pp. 147–150, 2011.

[49] L. Cao and H. K. Li, "Comparison of two compatible biomass models: a case from three broadleaf tree species in Guangdong

(in Chinese)," *Chinese Journal of Ecology*, vol. 38, pp. 1916–1925, 2019.

[50] Q. B. Luo, W. S. Zeng, D. B. He, T. H. Bao, and W. D. Lin, "Establishment and application of compatible tree avoveground biomass models (in Chinese)," *Journal of Natural Resources*, vol. 14, pp. 271–277, 1999.

[51] F. Yang, J. Tan, Q. Zhao et al., "Characteristics of $PM_{2.5}$ speciation in representative megacities and across China," *Atmospheric Chemistry and Physics*, vol. 11, no. 11, pp. 5207–5219, 2011.

[52] Y. Zhu, L. Yang, K. Kawamura et al., "Contributions and source identification of biogenic and anthropogenic hydrocarbons to secondary organic aerosols at Mt. Tai in 2014," *Environmental Pollution*, vol. 220, pp. 863–872, 2017.

[53] S. Deng, J. Ma, L. Zhang, Z. Jia, and L. Ma, "Microclimate simulation and model optimization of the effect of roadway green space on atmospheric particulate matter," *Environmental Pollution*, vol. 246, pp. 932–944, 2019.

[54] H. Shi, H. X. Wang, and Y. Y. Li, "Wettability on plant leaf surfaces and its ecological significance," *Acta Ecologica Sinica*, vol. 31, pp. 4287–4298, 2011.

[55] A. Q. Yang, G. Q. Sun, L. X. Lu, Z. F. Guo, and Y. M. Liu, "Deriving aerodynamic roughness length and zero-plane displacement height from MODIS product for Eastern China (in Chinese)," *Journal of the Meteorological Sciences*, vol. 31, pp. 516–524, 2011.

[56] C. X. Zhao, Y. J. Wang, Y. Q. Wang, and H. L. Zhang, "Interactions between fine particulate matter ($PM_{2.5}$) and vegetation: A review (in Chinese)," *Chinese Journal of Ecology*, vol. 32, pp. 2203–2210, 2013.

[57] M. Treshow, *Air Pollution and Plant Life*, Wiley, Hoboken, NJ, USA, 1984.

[58] N. Thao, X. Yu, and H. Zhang, "Deposition of particulate matter of different size fractions on leaf surfaces and in epicuticular waxes of urban forest species in summer and fall in Beijing, China," *International Journal of Phytoremediation*, vol. 3, 2014.

[59] K. Dzierżanowski, R. Popek, H. Gawrońska, A. Sæb, and S. W. Gawroński, "Deposition of particulate matter of different size fractions on leaf surfaces and in waxes of urban forest species," *International Journal of Phytoremediation*, vol. 13, pp. 1037–1046, 2011.

[60] J. Hofman, K. Wuyts, S. Van Wittenberghe, and R. Samson, "On the temporal variation of leaf magnetic parameters: seasonal accumulation of leaf-deposited and leaf-encapsulated particles of a roadside tree crown," *Science of the Total Environment*, vol. 493, pp. 766–772, 2014.

[61] Y. Zheng, Q. Zhang, Y. Liu, G. Geng, and K. He, "Estimating ground-level $PM_{2.5}$ concentrations over three megalopolises in China using satellite-derived aerosol optical depth measurements," *Atmospheric Environment*, vol. 124, pp. 232–242, 2016.

Hindawi
Advances in Meteorology
Volume 2019, Article ID 5250870, 14 pages
https://doi.org/10.1155/2019/5250870

Research Article

Impacts of Recent Climate Trends and Human Activity on the Land Cover Change of the Abbay River Basin in Ethiopia

Asaminew Abiyu Cherinet,[1] Denghua Yan,[1,2,3] Hao Wang,[1,2,3] Xinshan Song,[1] Tianlin Qin,[2,3] Mulualem T. Kassa,[4] Abel Girma,[1,5] Batsuren Dorjsuren,[6] Mohammed Gedefaw,[1,5] Hejia Wang,[7] and Otgonbayar Yadamjav[8]

[1]*College of Environmental Science and Engineering, Donghua University, Shanghai 201620, China*
[2]*State Key Laboratory of Simulation and Regulation of Water Cycle in River Basin, China Institute of Water Resources and Hydropower Research (IWHR), Beijing 100038, China*
[3]*Water Resources Department, China Institute of Water Resources and Hydropower Research (IWHR), Beijing 100038, China*
[4]*Bio-Taq Economy Innovations (BioTEI) Inc, Winnipeg, Canada*
[5]*Department of Natural Resource Management, University of Gondar, Gondar 196, Ethiopia*
[6]*Department of Environment and Forest Engineering, School of Engineering and Applied Sciences, National University of Mongolia, Ulaanbaatar 210646, Mongolia*
[7]*Department of Hydraulic Engineering, Tsinghua University, Haidian District, Beijing 100084, China*
[8]*Department of Sociology and Social Work, School of Art & Sciences, National University of Mongolia, Ulaanbaatar 210646, Mongolia*

Correspondence should be addressed to Denghua Yan; yandh@iwhr.com

Received 2 April 2019; Revised 9 August 2019; Accepted 5 September 2019; Published 15 October 2019

Guest Editor: Selahattin Incecik

The Abbay River Basin, which originates in Ethiopia, is a major tributary and main source of the Nile River Basin. Land cover and vegetation in the Abbay River Basin is highly susceptible to climate change. This study was conducted to investigate the trends of climate change for a period of thirty-six years (1980–2016) within selected stations of the basin by using the innovative trend analysis method, Mann–Kendall test, and Sen's slope estimator test to investigate the mean annual precipitation and temperature variables. Changes in land cover and vegetation in the Abbay River Basin were studied for a period of thirteen years (2001–2013) by using remote sensing, GIS analysis, land cover classification, and vegetation detection methods to assess the land cover and vegetation in the basin. In addition, Normalized Difference Vegetation Index (NDVI), Enhanced Vegetation Index (EVI), and Transformation Matrix were employed to analyze the spatial and temporal patterns of land cover and vegetation impacted by changes in climate. The result reflects that the trend of average annual temperature was remarkably increased ($\Phi = 0.12$, $Z = 0.75$) in the 36-year period, and the temperature was increased by 0.5°C, although precipitation had slightly decreased during the same period. In the thirteen years' period, forest land and water resource decreased by 3429.62 km^2 and 81.45 km^2, respectively. In contrast, an increment was observed in grassland (2779.33 km^2), cultivated land (535.34 km^2), bare land (43.08 km^2), urban land (0.65 km^2), and wetland (152.66 km^2) in the same period. In the study, it was also observed a decrease of an NDVI value by 0.1 was observed in 2013 in the southern part of the basin. The findings of the present study illustrate a significant change in eco-hydrological conditions in the ARB with an adverse impact on the environment. Hydroclimatic changes caused the increase in temperature and decreasing trend in precipitation which significantly impacted the land cover and vegetation in the basin. The changes in land cover were mostly caused by global and local climate influence which mainly affects the hydroclimate and eco-hydrology systems of the basin. The result is consistent with that of the previous studies conducted elsewhere. The findings of this paper could help researchers to understand the eco-hydrological condition of the study basin and become a foundation for further studies.

1. Introduction

Climate change is a major factor, which directly influences land cover and hydrology systems. In the past five decades, a global climatic change had been observed, leading to the changes in the hydrological cycle [1]. Climate change affects water resources by disrupting the hydrological system mainly through a change in quantity and quality of water, erratic water flow, timing, groundwater recharge, and others. Thus, future policies on water resources planning, development, and management should consider the impacts of climate change on land cover and water resources [2–4]. In addition, other forces of change such as demographic trends, climate variability, and national and macroeconomic policies alter the land cover which could, in turn, impact the hydrologic system [5]. Deforestation and plantation were the key factors of the land cover change. It is well-known that deforestation is a major cause of serious global environmental crisis [6]. As previously reported [6], deforestation of natural forests is a common phenomenon in the study basin. The land cover change could greatly alter the provision of ecosystem services. Vast areas of native grasslands, natural forests, and wetlands around the world had been destroyed and converted into croplands (for food production), tree plantations (for timber), and urban areas (housing). This alteration of the natural system had seriously impacted ecosystem services and biodiversity [5]. In developing countries, in particular, deforestation of forestlands had significantly been accelerated due to human needs for more agricultural lands for food production [7]. Another main cause of climate change is natural factors, which can bring either direct or indirect changes [8]. Land cover change, in general, is a key indicator of climate and human impacts on the environment. These include settlement and agricultural history, population growth and mobility, farming system practices, land and tree tenure systems, markets, and infrastructure and technological changes [9]. Land cover change is a very important topic in global change research. In the global scope, it plays an important role in the hydrothermal cycle of the global land water system [10]. As noted in the previous study [11], a land cover change had significant impacts on a global environmental change that affects the quantity of water in the ecosystems.

The Abbay River Basin has a dynamic change in land cover exacerbated by a high rate of population growth and climate change in the region. There is evidence that had shown forest lands being replaced by food crops [12]. Croplands usage is primarily shifted to coffee or Eucalyptus tree plantation [12]. Recent reports had also shown a significant increase in urbanization in the region with a higher rate (16%) of urban population growth [13, 14]. The high demands for fuelwood and construction materials have significantly enhanced the plantation of Eucalyptus trees in the region [15]. These shifts in land cover profile had cascading effects on ecosystem services and pose serious challenges in the region [16]. In this study, we analyzed the overall trends and changes of the land cover on ecosystem services using a transformation matrix for a period of 13 years (2001–2013) and historical climate change trends for 36 years (1980–2016). The study had also analyzed vegetation evolution assessment to identify the level of change in vegetation cover using Normalized Difference Vegetation Index (NDVI) and Enhanced Vegetation Index (EVI).

2. Materials and Methods

2.1. Study Area. Abbay River Basin is located in the northwestern region of Ethiopia between 7°40′N and 12°51′N latitude and 34°25′E and 39°49′E longitude. It covers an area of 199,592.17 km^2 [17] and extends to Amhara, Oromia, and Benishan-gul-Gumuz regional states. It shares a boundary with the Tekeze Basin to the north, the Awash Basin to the east and southeast, the Omo-Gibe Basin to the south, and the Baro-Akobo Basin to the southwest. The country's largest freshwater lake, Lake Tana, is the source of the Abbay River Basin and is located north of the basin. The basin is subdivided into 16 subbasins based on major rivers in the basin and its tributaries [13, 17, 18]. The Abbay River Basin is a land of dramatic gorges and mountains and is the most important river basin in Ethiopia. It is the major source of water for the Nile River Basin (Figure 1).

2.2. Data Sources

2.2.1. Land Cover Data Sources. The land cover satellite data of the study area were collected from the Ministry of Energy and Water Resources of Ethiopia. The data were found from Global Land Covers Dataset (GlobeLand30) as described by the National Geometrics Center of China in 2014 (Table 1). It shows the name, code, and definition of land cover classification and Landsat Thematic Mapper (TM) and Enhanced Thematic Mapper Plus (ETM+) data with a resolution of 30 m for thirteen-year period (2001 to 2013). Images data files were downloaded from the United State Geological Survey (USGS) website and extracted to Tiff format files to interpret the land cover spatial pattern data for the 13-year (2001–2013) period. In this study, the expanded classification system was adopted to sufficiently capture the local characteristics of the study area (Table 1). To understand the overall changes in land cover, matrix changes were analyzed and mapped [16]. Prior to classification, pre-image-processing operations including image restoration, georeferencing, and image enhancement were performed. Ecological landscape potential map, topographic, forest, and vegetation maps were chosen for accuracy testing and validation. The accuracy was tested after classification with accuracy assessment tools using representative data points.

2.2.2. Meteorology Data Sources. As cited in a previous study [19], the baseline climate scenario represents current climate conditions, particularly precipitation and temperature patterns. As in most climate change studies, this study uses average annual precipitation and temperature data from thirty-six years (1980 to 2016). Data for current climate conditions of the study area were acquired from the Ministry of Energy and Water Resources of Ethiopia, the National Meteorological Agency of Ethiopia. The data were collected from 5 different stations from four regional states and were derived from the National Oceanic and Atmospheric

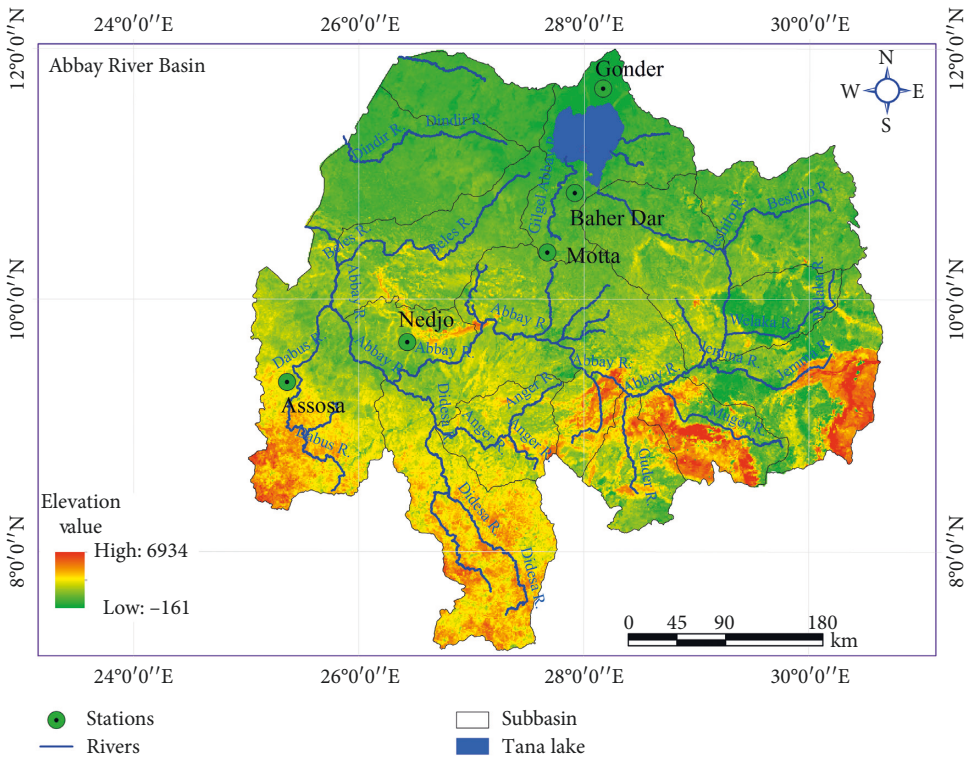

Figure 1: Digital elevation map (DEM) of Ethiopia and location map of the study area.

Table 1: Land covers types and their detail descriptions in Abbay River Basin.

Land cover types	Code	Description
Bare land	Bl	Areas of land that are poorly covered by vegetation due to erosion, overgrazing, cultivation, mining area, etc.
Cultivated land	Cl	Lands used for agriculture, horticulture, and gardens, including paddy fields, irrigated and dry farmland, vegetation and fruit gardens, etc.
Forest land	Fl	Lands covered with trees, with vegetation cover over 30%, including deciduous and coniferous forests, and sparse woodland with cover 10–30%, etc.
Grass land	Gl	Lands covered by natural grass with cover over 10%, etc.
Urban	Ur	Lands modified by human activities, including all kinds of habitation, residential, commercial, industrial, transportation facilities, interior urban green zones, etc.
Water	Wa	Water bodies in the land area, including river, lake, reservoir, fish pond, lands covered by temporally snow, glacier and icecap, etc.
Wetland	Wl	Lands covered with wetland plants and water bodies, including inland marsh, lake marsh, river floodplain wetland, forest/shrub wetland, peat bogs, mangrove and salt marsh, etc.

Administration (NOAA), National Centers for Environmental Information (NCEI).

2.2.3. Vegetation Data Sources. Normalized Difference Vegetation Index (NDVI) and Enhanced Vegetation Index (EVI) data were extracted by referencing the Moderate Resolution Imaging Spectra Radiometer Enhanced Vegetation Index (MODIS NDVI) product (MOD13Q1) obtained from NASA. The NDVI was calculated from the MODIS land-surface reflectance values from the red band (610–680 nm) and near-infrared band (780–890 nm) and corrected with molecular scattering, ozone absorption, and aerosols [9]. The MOD13A3 products, which include 12

scientific data sets with a 250 m by 250 m spatial resolution and a 16-day temporal sampling period, were derived from the latest version (Collection 6) from 1st September to 16th September in both 2001 and 2013. The MOD13Q1 products were downloaded from USGS (https://lpdaac.usgs.gov/).

2.3. Methods

2.3.1. Land Cover Analysis. Classified and unclassified maps of the study area were generated based on a classification scheme with a maximum likelihood classifier (Table 1). Abbay River Basin landscape was classified into seven land classes (Figure 2). Land cover maps of the study area for the year 2001 and 2013 were generated from Landsat TM and ETM+ imagery classification. Land cover change extent was determined as previously described [20]. The analysis evaluates the changes in land cover over time to establish the relationship between land cover changes and spatial patterns using overlapping operation. The analysis was conducted using postclassification comparison method where Landsat image for each year was classified and labeled independently followed by a comparison using an overlay procedure [21]. The magnitudes of change in terms of land cover were determined using the method described by [22]. The variables were calculated as follows:

$$A = \mathrm{TA}(t_2) - \mathrm{TA}(t_1), \tag{1}$$

$$\mathrm{CE} = \left[\frac{\mathrm{CA}}{\mathrm{TA}(t_1)}\right] * 100, \tag{2}$$

where TA is the total area, CA is the changed area, CE is the change extent, and t_1 and t_2 are the beginning and ending times the land cover studies were conducted.

It is worth noting here that the widest classification accuracy used by most researchers is in the form of an error matrix, which is used to derive a series of descriptive and analytical statistics. As described in [21, 23], assessment of classification accuracy for 2001 and 2013 images was conducted to determine the quality of information derived from the data. It was coupled with previous knowledge of the area and used as reference data. If classification data are to be useful in detecting change analysis, it is important to perform an accuracy assessment for each individual classification. Kappa coefficient and error matrix are standard measures of the reliability and accuracy of the maps produced. The Kappa statistics were determined in this study while the methods were described in detail in the previous studies [24, 25]. Kappa coefficient was calculated using the following equations [21]:

$$K = \frac{P(A) - P(E)}{1 - P(E)}, \tag{3}$$

$$P(A) = \frac{(A + D)}{N}, \tag{4}$$

$$(E) = \left(\frac{A1}{N}\right) * \left(\frac{B1}{N}\right) + \left(\frac{A2}{N}\right) * \left(\frac{B2}{N}\right), \tag{5}$$

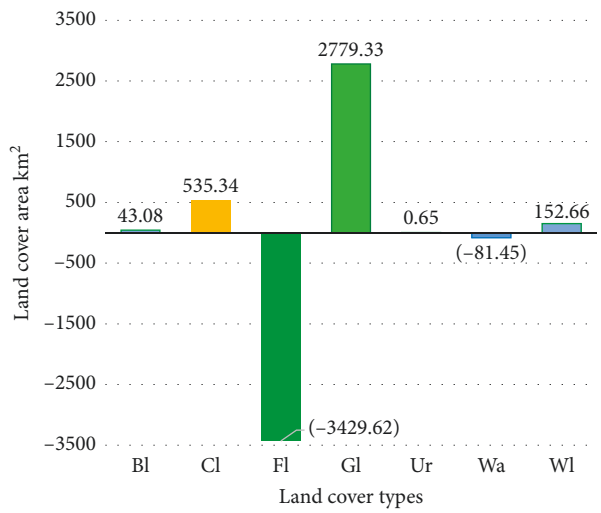

Figure 2: Land cover change extent in 2001 and 2013 of the study area.

where K is the Kappa coefficient, $P(A)$ is the number of times the k raters agree, and $P(E)$ is the number of times the k raters are expected to agree only by chance [26], A and D are the unchanged categories, $A1$ and $B1$ are the subject's categories, and N is the change of results.

2.3.2. Vegetation Analysis. Normalized Difference Vegetation Index (NDVI) metric and the coarse spatial resolution were primarily used for testing possible methodologies and were supported by ground-based information [9]. Vegetation attributes were used in various models to study photosynthesis, carbon budget, water balance, and related terrestrial processes [27]. The MODIS Vegetation Index was developed within 16 days of variation, and at multiple spatial resolutions to provide consistent spatial and modern comparisons of leafy surroundings, a composite property of leaf area, chlorophyll and canopy structures. The common compositing time of 8–14 days provides at least 25–30 global NDVI datasets per year as described in [28]. These products characterize more effectively the global range of vegetation states and processes. The MODIS Normalized Difference Vegetation Index (NDVI) complements NOAA's Advanced Very-High-Resolution Radiometer (AVHRR) NDVI products and provides continuity for time series historical applications. Enhanced Vegetation Index (EVI), which minimizes canopy soil variation, was used to improve sensitivity over dense vegetation conditions. Vegetation cover was determined using the NDVI and EVI matrices (Figure 2). Normalized Difference Vegetation Index (NDVI) is the most widely used vegetation index to distinguish between healthy vegetation from others (e.g., nonvegetated areas) [25]. NDVI is one of the indicators for the vegetative greenness of an area, and therefore, changes in NDVI are changes in vegetation and vegetation indices, which is an indirect indicator of plant biomass and vegetation activity [27, 29]. It is derived using the following expression:

$$\mathrm{NDVI} = \frac{(\mathrm{NIR} - \mathrm{RED})}{(\mathrm{NIR} + \mathrm{RED})}, \tag{6}$$

where NIR is the near-infrared and RED is the red channel of the electromagnetic spectrum, corresponding to bands 2 and 1 of the MODIS (MOD13Q1) product.

The study also explored the conceptual and methodological issues that arise when scaling the use of NDVI for obtaining information on land cover from country to the study area scale. The second vegetation layer is the Enhanced Vegetation Index (EVI), which has improved sensitivity for high biomass regions and was calculated using the following equation:

$$D = \frac{(\mathrm{NDVI} - \mathrm{NDVI}_{\min})}{(\mathrm{NDVI}_{\max} - \mathrm{NDVI}_{\min})}, \tag{7}$$

where $\mathrm{NDVI}_{\max}$ and $\mathrm{NDVI}_{\min}$ represent the maximum and minimum NDVI values for each vegetation (forest, grassland, shrub land) class. Afterwards, the values of the cover density index were classified into four ranges (<20, 20–50, 50–80, and >80%). Integration, spatial analysis, and any calculations were carried out in the GIS environment (QGIS 1.8, GRASS 6.4.2). The geographic information was projected to WGS84 UTM zone 33.

2.3.3. Meteorology Analysis. Metrological data like average annual Temperature and precipitation data from 5 stations were investigated in the Abbay River Basin from different representative stations of the study area (Table 2). Based on the class of the stations, the number of climate variables collected varies from stations to stations. Observe the selected climate stations in the Abbay River Basin are taken into indicator in the following table classification class's considerations. Climate data were calculated on 5 metrological stations of Assosa, Bahir Dar, Gondar, Nedjo, and Motta for analytical mathematics method.

(1) Innovative Trend Analysis Method (ITAM). The innovative trend analysis method (ITAM) divides a time series into two equal parts, and it sorts both subseries in the ascending order [6, 30–34]. Then, the two halves are placed on a coordinate system $(x_i : i = 1, 2, 3, \ldots, n/2)$ on X-axis and $(x_j : j = n/2 + 1, n/2 + 2, \ldots, n)$ on Y-axis. If the time series data on a scattered plot are collected on the 1 : 1 (45°) straight line, it indicates no trend. However, the trend is increasing when data points accumulate above the 1 : 1 straight line and the trend is decreasing when data points accumulate below the 1 : 1 straight line. The mean value difference between x_i and x_j could give the trend magnitude of data series. The first observed data point was not considered in this study when classifying the time series data into x_i and x_j data points have a different size (Figure 3).

Annual precipitation is 36 years from 1980–2016, and annual temperature is 36 years from 1980 to 2016. The direction of the trend is also affected by x_i data series. The trend indicator of ITAM is multiplied by 10 to make the scale similar to the other two tests. The trend indicator is given as follows:

Table 2: Names of meteorology stations, longitude, latitude, and elevation of the study area.

No.	Name of stations	Longitude E	Latitude N	Elevation (m)
1	Bahir Dar	37°22′59.99″E	11°35′59.99″N	1770
2	Gondar	37°27′59.99″E	12°35′59.99″N	1967
3	Motta	37°51′59.99″E	11°04′60.00″N	2440
4	Assosa	34°30′59.99″E	10°03′60.00″N	1600
5	Nedjo	35°29′59.99″E	9°29′59.99″N	1800

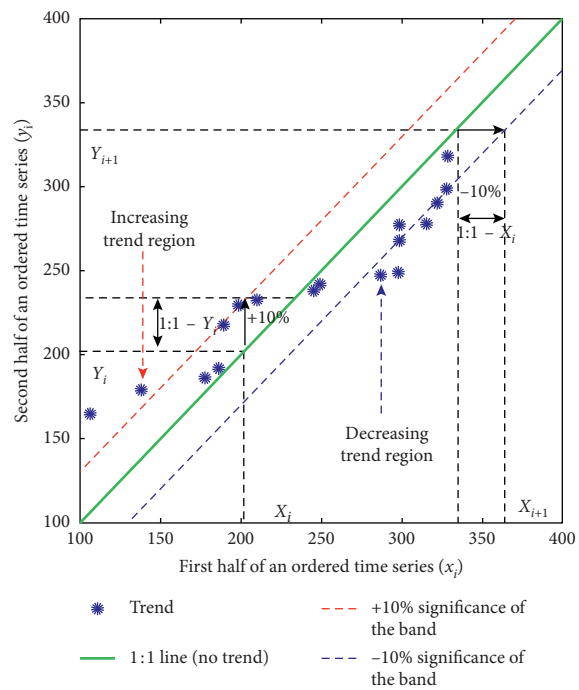

Figure 3: Paradigmatic of the ITA method.

$$\Phi = \frac{1}{n} \sum_{i=1}^{n} \frac{10\left(x_j - x_i\right)}{\mu}, \tag{8}$$

where Φ = trend indicator, n = number of observation on the subseries, x_i = data series in the first half subseries class, x_j = data series in the second half subseries part, and μ = mean of data series in the first half subseries part. A positive value of Φ indicates an increasing trend. However, a negative value of Φ indicates a decreasing trend. However, when the scatter points are closest around the 1 : 1 straight line, it implies the nonexistence of a significant trend.

(2) Mann–Kendall Trend Test. The Mann–Kendall (MK) trend test is a nonparametric test commonly employed to detect changing trends in a series of environmental data, climate data, or hydrological data [28, 31, 35–37]. The Mann–Kendall (MK) test method also shows upward and downward trends with statistical significance. The strength of the trend depends on the magnitude, sample size, and variations of data series. When the data point of later year is larger than the data point of the previous year, the MK statistics is increased by one otherwise the MK statistics

decreased by one. Thus, the MK statistics is the cumulative result of all the data values. The Mann–Kendall test statistics "S" is then equated as follows:

$$S = \sum_{i=1}^{n-1} \sum_{j=i+1}^{n} \operatorname{sgn}\left(x_j - x_i\right). \tag{9}$$

The trend test is applied to x_i data values $(i = 1, 2, \ldots, n-1)$ and x_j $(j = i+1, 2, \ldots, n)$. The data value of each x_i is used as a reference point to compare with the data value of x_j which is given as follows:

$$\operatorname{sgn}\left(x_j - x_i\right) = \begin{cases} +1, \text{if}\left(x_j - x_i\right) > 0, \\ 0, \text{ if}\left(x_j - x_i\right) = 0, \\ -1, \text{if}\left(x_j - x_i\right) < 0, \end{cases} \tag{10}$$

where x_j and x_i are the values in periods j and i. When the number of data series greater than or equal to ten $(n \geq 10)$, the MK test is then characterized by a normal distribution with the mean $E(S) = 0$ and variance $\operatorname{Var}(S)$ is equated as follows:

$$E(S) = 0, \tag{11}$$

$$\operatorname{Var}(S) = \frac{n(n-1)(2n+5) - \sum_{k=1}^{m} t_k\left(t_k - 1\right)\left(2t_k + 5\right)}{18}, \tag{12}$$

where m is the number of the tied groups in the time series and t_k is the number of ties in the kth tied group. The test statistics Z is as follows:

$$Z = \begin{cases} \dfrac{s-1}{\delta}, & \text{if } S > 0, \\ 0, & \text{if } S = 0, \\ \dfrac{s+1}{\delta}, & \text{if } S < 0. \end{cases} \tag{13}$$

When Z is greater than zero, it indicates an increasing trend and when Z is less than zero, it is a decreasing trend.

(3) Sen's Slope Estimator Test. Sen's Slope Estimator has been used extensively in meteorological time series and equally applicable where data gap exists [38]. The trend magnitude is calculated by slope estimator methods. The slope Q_i between two data points is given by the following equation:

$$Q_i = \frac{x_j - x_k}{j - k}, \quad \text{for } i = 1, 2, \ldots, N, \tag{14}$$

where x_j and x_k are data points at time j and $(j > k)$, respectively. When there is only single datum in each time, then $N = n(n-1)/2$; n is the number of time periods. However, if the number of data in each year is high, then $N < n(n-1)/2$; n is the total number of observations [39]. The N values of slope estimator are arranged from smallest to biggest. Then, the median of slope (β) is computed as follows:

$$\beta = \begin{cases} Q\left[\dfrac{N+1}{2}\right], & \text{when } N \text{ is odd}, \\ Q\left[\dfrac{(N/2) + Q(N+2)/2}{2}\right], & \text{when } N \text{ is even}. \end{cases} \tag{15}$$

The sign of β shows whether the trend is increasing or decreasing. When Q_i is positive, it means that there is an increasing or upward trend, while the negative value of Q_i reveals decreasing or downward trend in time series analysis. Similarly, zero value indicates no trend.

3. Results and Discussion

3.1. Classification of Land Cover Type and Change Detection. The results show a degree of land cover changes over a period of 13 years (2001–2013). During this period (2001–2013), grassland was the dominant vegetation type followed by cultivated land and bare land (Table 3; Figures 2 and 4). In the same period, it was observed that the forest land and water bodies were reduced (Table 3; Figures 2 and 4). The result in this study is consistent with that of the previous reports [6] and found that forest land cover was significantly diminished particularly in the northern part of the study region. The seven land cover classes identified in the study area were cultivated land, forest land, grassland, water body, wetland, bare land, and urban land (Figures 2 and 4; Table 3). The number of classified pixels increased for cultivated land (Cl), grassland (Gl), and wetland (We) but decreased for of forest land (Fl) and water body (Wl) (Figure 2). During the 13-year period, significant changes in the study area occurred particularly in forest land and water bodies, respectively, and the former decreased by 3429.62 km^2 (1.72%) while the latter decreased by 81.45 km^2 (0.04%), respectively. On the contrary, cultivated land, grassland, wetland, bare land, and urban land were increased by 535.34 km^2 (0.27%), 2779.33 km^2 (1.39%), 152.66 km^2 (0.08%), 43.08 km^2 (0.02%), and 0.65 km^2 (0.0003%), respectively (Table 3 and Figure 4). Cultivated land, grassland, wetland, bare land, and urban covers were slightly increased in area at the end of the study period compared to that of at the beginning of the study period. However, there were both increments and reductions in these land classes between the different observation points (Figure 4) and SAT.

Human activities associated with economic factors are commonly cited as a major stimulus for land cover change [24]. The increasing trend of land cover change observed in this study is associated mainly with economic forces. It was observed in the study that forest covers were mostly surrounded by farmlands, particularly in the catchment area and the increase in population density in the area clear forest lands to provide farmlands for food production [6].

Total forest cover in the study area reduced by half between 1957 and 2000 [6, 8]. In general, the result reported in this study is similar in accuracy of change of the listed previous studies (Figure 2).

As reported in the previous studies [23, 24, 26], the accuracy of individual classifications is very important to generate useful data for the land cover change study. There

Table 3: Changing present of land covers in 2001 and 2013.

No.	Land cover types	Initial area 2001		Final area 2013		Changing status	
		km^2	%	km^2	%	km^2	%
1	Bare land	12.28	0.01	55.36	0.03	43.08	0.02
2	Cultivated land	58249.08	29.18	58784.42	29.45	535.34	0.27
3	Forest land	6460.33	3.24	3030.72	1.52	(−3429.62)	−1.72
4	Grass land	131551.69	65.91	134331.01	67.30	2779.33	1.39
5	Urban	89.45	0.04	90.10	0.05	0.65	0.0003
6	Water	3141.27	1.57	3059.82	1.53	(−81.45)	−0.04
7	Wetland	88.08	0.04	240.74	0.12	152.66	0.08

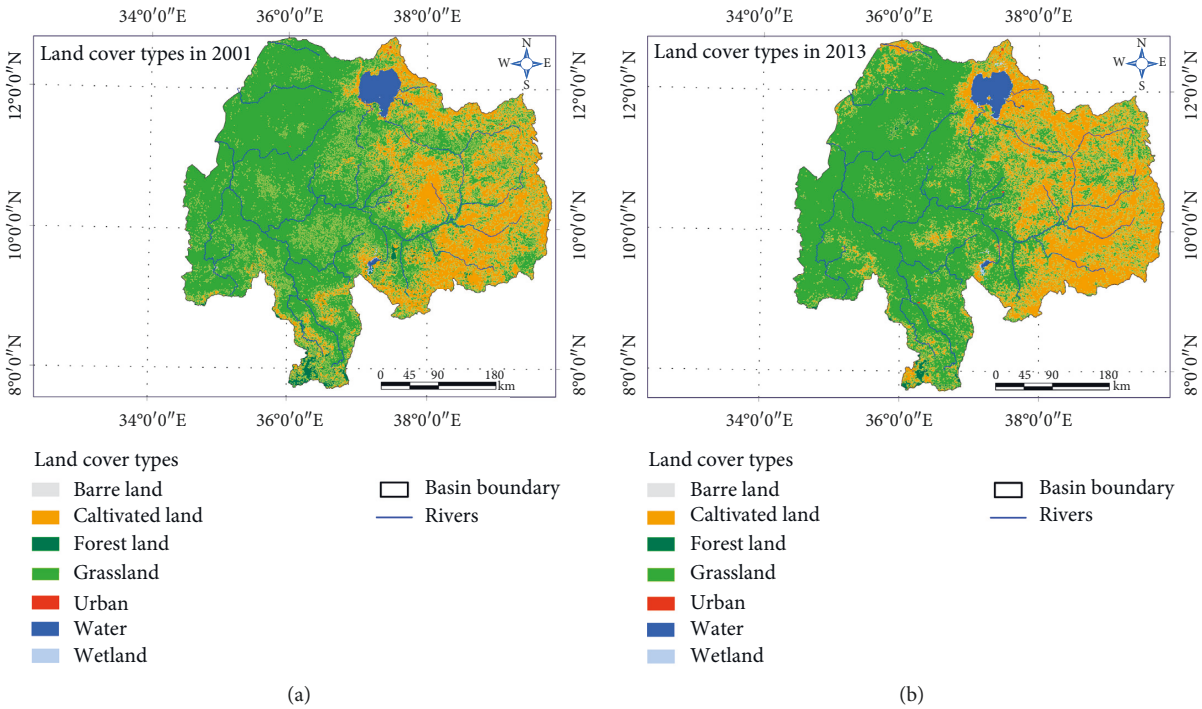

Figure 4: Classification of the changing land cover map of Abbay River Basin (2001 and 2013) Derived from Landsat TM/ETM+ images: (a) description of land cover in 2001 and (b) description of land cover and change in 2013.

are various ways of conducting change detection analysis. In this study, a land cover classification for the year 2001 and 2013 was produced, and the accuracy assessments were checked using 0.89 Kappa coefficient of the transformation matrix (Table 4). The statistical Kappa coefficient classification accuracy recommended value ranges from 0.18 to 0.99. Thus, the result in this study is considered almost in perfect agreement based on the Kappa Statistics. This implies that the change detection results could be used for further analysis as land cover transformation matrix and ArcGIS 10.4 were employed to analyze a comprehensive land use dynamics degree [40].

Following anthropogenic effects, climate change is the most important driving force that impacts land cover change and water resources. This study revealed the dynamic of changes in land cover particularly forest land and indirectly the impacts on the water resources system of the basin. As reported in [41], the catchment in the study area was converted to farmlands and human settlements from other land use (e.g., forest land) in various years. The land cover map of 2001–2013 in Table 4 shows that forest land cover of about 555.01 km^2 was converted into cultivated land, 2965.44 km^2 into grassland, 42.83 km^2 into the wetland, and 2.67 km^2 into bare land. Of the coverage of water resources, 50.43 km^2 was changed into wetland, 21.30 km^2 converted to bare land, 11.75 km^2 into forest land, and 5.05 km^2 converted to grassland. In general, during the 13-year period (2001–2013), cultivated land had increased by 535.34 km^2, the increase of grassland (2779.33 km^2), wetland (+152.66 km^2), bare land (+43.08 km^2), and urban (+0.65 km^2). However, forest land and water bodies were decreased by 3429.62 km^2 (1.72%) and 81.45 km^2 (0.04%), respectively. The individual class areas and change statistics for the two periods are summarized in Tables 3 and 4. The change indicates that there is a driving force that impacted a visible land cover change. Several researchers had warned the serious impacts of climate change and human activities on water resources and the ecosystem of the basin [14, 41, 42], and the results of this study are consistent with the findings of these studies.

Table 4: Comparison of the process change of land covers in 2001 and 2013.

		Land cover types (2001)							
	Types	Bl	Cl	Fl	Gl	Ur	Wa	Wl	Total
Land cover types (2013)	Bl	7.61	3.69	2.67	18.09	0.00	21.30	2.00	**55.36**
	Cl	0.00	55179.84	555.01	3041.43	4.37	0.07	3.72	**58784.42**
	Fl	0.00	74.02	2893.03	36.67	0.00	11.75	15.25	**3030.72**
	Gl	1.00	2953.95	2965.44	128386.35	2.08	5.05	17.15	**134331.01**
	Ur	0.00	3.68	0.03	4.38	82.00	0.00	0.00	**90.10**
	Wa	1.03	2.68	1.33	0.92	0.00	3052.68	1.18	**3059.82**
	Wl	2.64	31.22	42.83	63.84	1.00	50.43	48.78	**240.74**
	Total	**12.28**	**58249.08**	**6460.33**	**131551.69**	**89.45**	**3141.27**	**88.08**	

3.2. Measuring Vegetation (NDVI and EVI). Common values of the pixel varied between −1 and 1. The highest values of NDVI were >0.3, indicating rich or healthy vegetation. In this study, conversation of forest and grasslands into agricultural land was found to be the main cause of land cover change. The change had affected the hydro-ecological system of the region particularly due to the high requirement of irrigation water to support crop production. The maximum value of NDVI ranges from 0.99 to −0.19 in 2001, and the minimum value ranges from 0.99 to −0.20 in 2013. Significant land cover change occurs in the southern part of the studied area, while on the other sides, insignificant vegetation cover change was observed Figure 5. A vegetation cover is an important factor that could change the ecosystem and the hydrology pattern in the basin, thereby causing climate variability. Vegetation dynamics could change the global carbon and hydrology cycle as well as climate change [40]. The overlaps of the NDVI, EVI maps of 2001 and 2013, and climatic variations of the current weather show a high degree of climate change occurring across the basin.

3.3. Climate Trends in the Basin. In recent years, attention had been given to look the potential effects of climate change on the basin. In fact, some studies had shown that the water resources are critically sensitive to climate change [2, 3]. In a 36-year period (1980–2016), the temperature in the basin was increased by 0.5°C or 0.14°C per year. The minimum and the maximum recorded temperatures were 19.25°C and 17.00°C per year, respectively. In the study region, the observed temperature was increased from 1980 to 2016 ($y = 0.0039x + 19.349$) (Figure 6).

The global mean temperature had risen by about 0.85 from 1880 to 2012 and is expected to grow steadily. Global warming can change the region hydrology and inflows river ecosystem quickly. The temperature inland water bodies around the world had been rapidly warming since 1985 with an average rate between 0.045 ± 0.011°C and year-over-year with a maximum ret of 0.10 ± 0.01°C. In the current study, the temperature had raised by 0.5°C in 36 years, which fits well with the global rate of temperature change. There were differences in temperature changes among stations in the study area during the 36-years period 1980–2016.

The overall trends in average precipitation in the study area were increasing. Though the change was insignificant for this period, there was a change in precipitation for the last decade of this period that may affect the water supply system in the basin. Changes in average temperature and precipitation in the study area were observed during the 36-year (1980 to 2016) period, but the rates of change were different among stations in the study basin. It was observed that the mean annual average temperature increased while precipitation decreased in the whole basin during this period and climate change was found to have serious impacts in the study area (Figure 6). The result strongly supports our speculation climate change is one of the major driving forces that affects land cover change in the Abbay River Basin.

3.3.1. Analysis of Temperature. The ITA test shows an increasing trend in average condition. The trends of the average temperature for five stations are shown in Figure 7. The increasing trends of temperature were detected in Gondar station while decreasing trend was detected in Assosa station (Table 4).

The ITA results show that statistics are negative and positive values, most of them are significant. The ITA annual temperature shows an increasing trend in Assosa station ($\Phi = 2.63$), a statistically sharp decreasing trend in Bahir Dar station ($\Phi = -3.86$), a decreasing trend in Nedjo station ($\Phi = -1.78$), an increasing trend in Gondar station ($\Phi = 0.40$), in Motta station a statistically increasing trend was observed with ($\Phi = 0.30$), and finally a statistically significant increasing trend was observed in average condition (five stations) ($\Phi = 0.12$) (Table 5).

The MK trend annual temperature shows a decreasing trend in Assosa station ($Z = -2.61$), a statistically decreasing trend in Bahir Dar station ($Z = -2.63$), a statistically significant decreasing trend in Nedjo station ($Z = -3.53$), a significant increasing trend in Gondar station ($Z = 6.96$), a statistically significant increasing trend was observed in Motta station with ($Z = 4.58$), and, in general, a statistically significant increasing trend was observed in average condition (five stations) ($Z = 0.75$).

Annual temperature in the results of Sen's slope estimator test shows a sharply increasing trend observed in average condition ($Z = 0.75$). The ITA results (Figure 6) show that most points increase above the 1 : 1 line, an overall upward trend. However, the features of trends in annual mean temperature are quite distinct at each station. Figure 6 shows that the annual temperature significantly increased at the Gondar (Figure 7(c)) and Motta (Figure 7(e)), while at

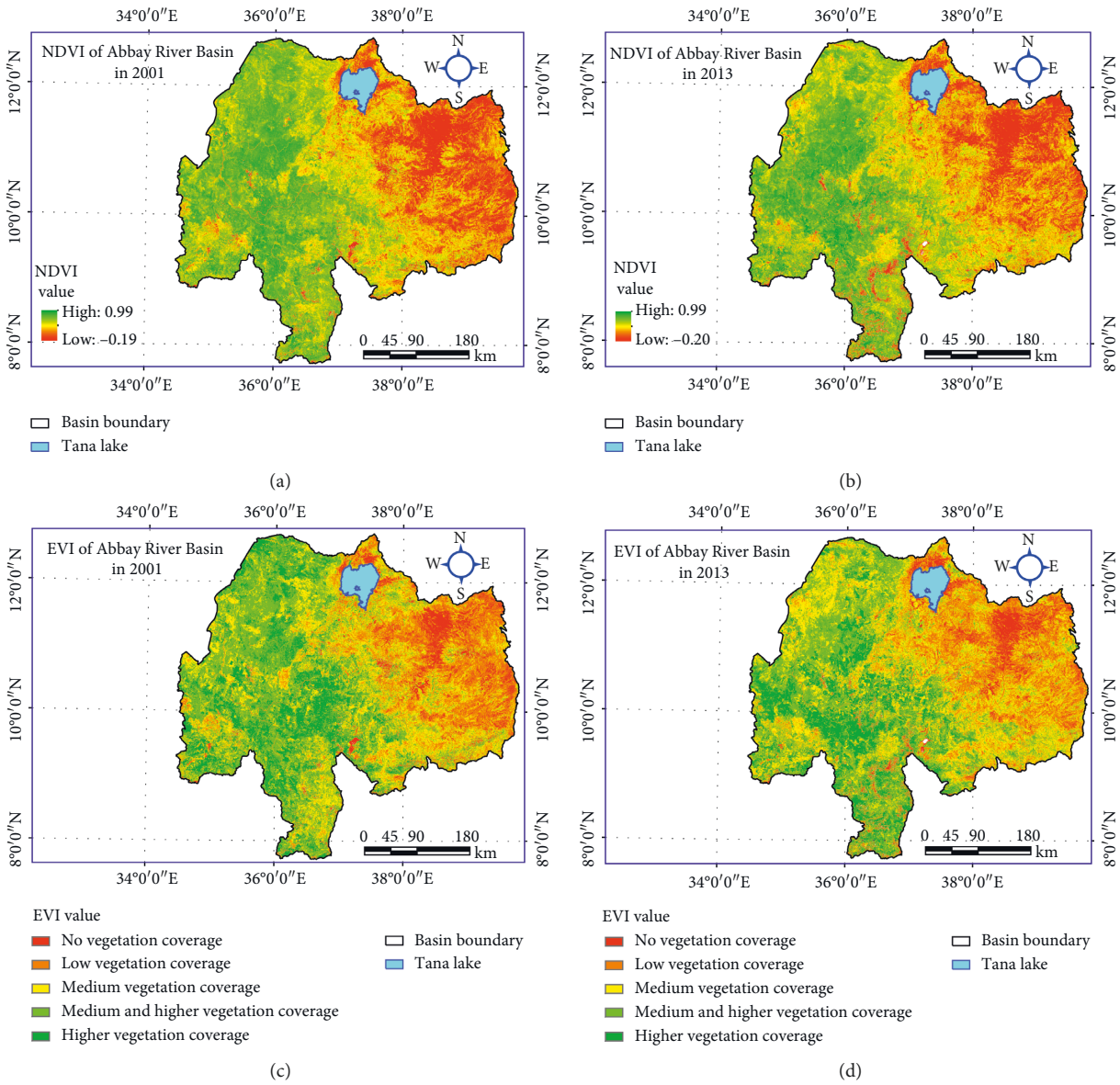

Figure 5: NDVI and EVA of Abbay River Basin in 2001 and 2013: (a) description of NDVI in 2001 and (b) description of NDVI in 2013; (c) description of EVI in 2001; and (d) description of EVI in 2013.

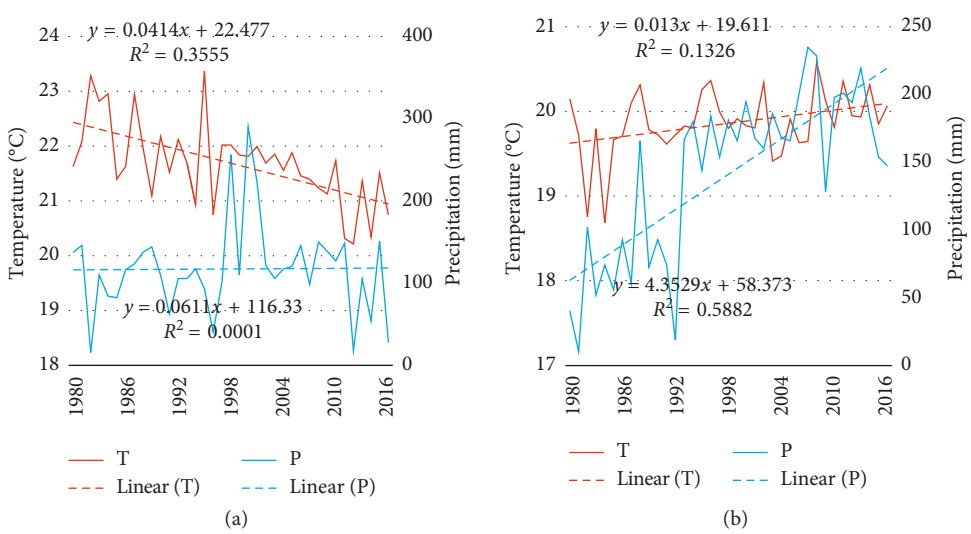

Figure 6: Continued.

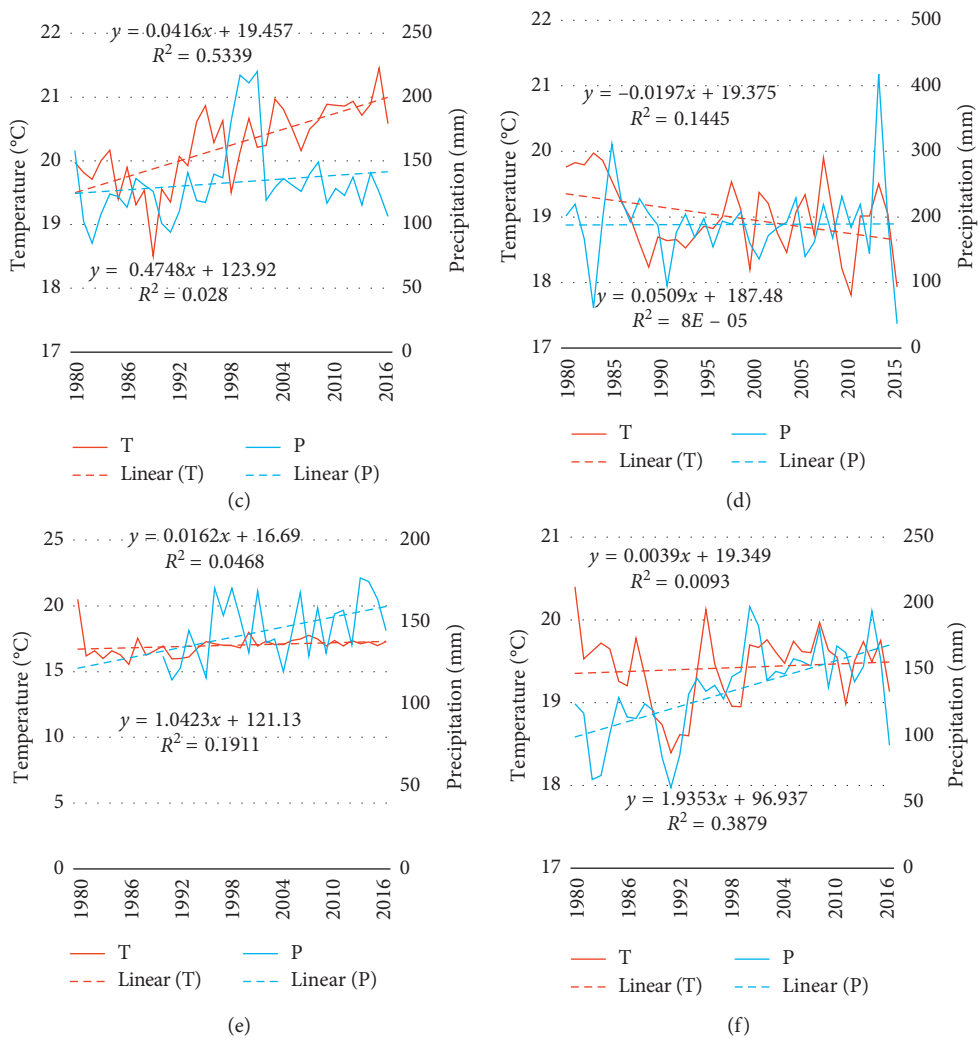

Figure 6: Description of the climate variability in Abbay River Basin. The temperature and precipitation trend for the period 1980–2016. The vertical column is temperature and horizontal column is precipitation change, and fluctuations line indicates annual values and breakdown lines indicate period running averages. (a) Asossa station. (b) Bahir Dar station. (c) Gondar station. (d) Nedjo station. (e) Motta station. (f) Average condition.

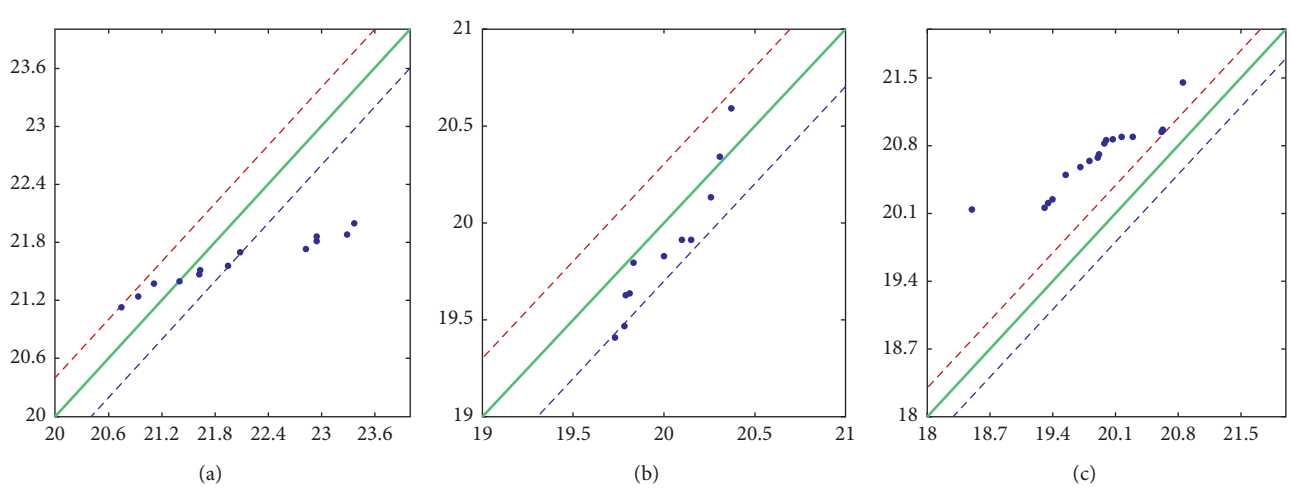

Figure 7: Continued.

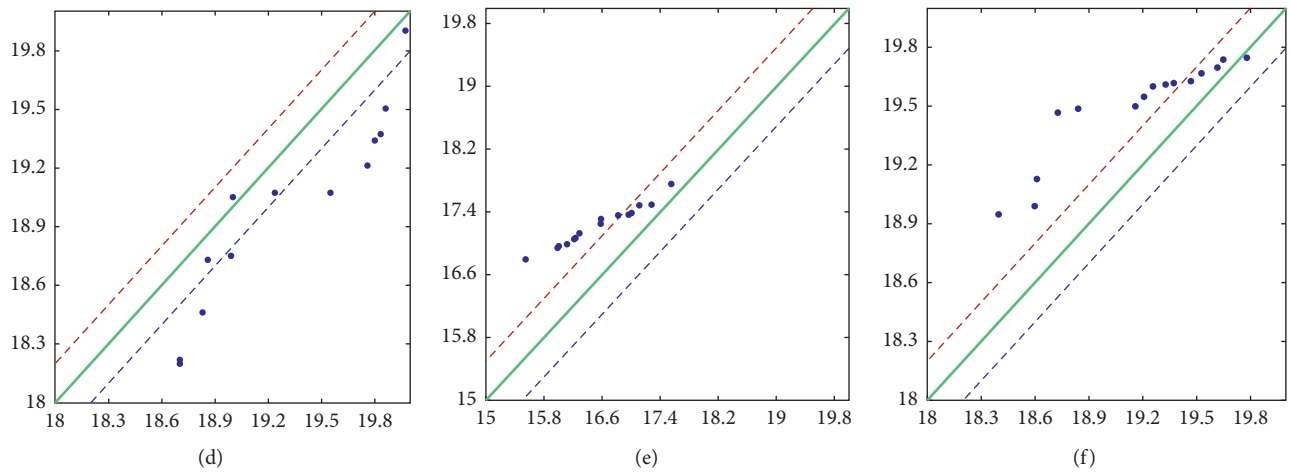

Figure 7: Results of ITA for annual temperature during 1986–2016. (a) Assosa station. (b) Bahir Dar station. (c) Gondar station. (d) Nedjo station. (e) Motta station. (f) Average condition.

Table 5: Trend test results of the annual average air temperature in the subbasins based on ITAM (Φ), MK (Z), and Sen's slope estimator test (β) analyses.

S/No.	Name of stations	Z (MK)	Φ	β
1	Assosa	−2.61**	2.63**	−0.03
2	Bahir Dar	−2.63**	−3.86***	−0.02
3	Nedjo	−3.53***	−1.78*	−0.03
4	Gondar	6.96***	0.40	0.04
5	Motta	4.58***	0.30	0.03
6	Average	0.75	0.12	0.00

*Trends at 0.1 significance level; **trends at 0.05 significance level; ***trends at 0.01 significance level.

the Assosa (Figure 7(a)), Bahir Dar (Figure 7(b)), and Nedjo (Figure 7(c)) stations, some points fall below the 1 : 1 line, some upward trend. But the trend of average annual temperature is increasing during 1978–2016 with respect to the 10% relative band.

3.3.2. Analysis of Precipitation. The trends of annual precipitation for five stations and average condition detected by the ITAM, MK, and Sen's slope estimator test are summarized in Table 6.

The ITA results showed that statistics are dominated by positive values, but most of them are insignificant. Five stations in average conditions were significant ($\Phi = 3.04$) A significant increasing trend was observed in Bahir Dar station ($\Phi = 28.91$) while the most decreasing trend was in the Nedjo station ($\Phi = 0.02$).

The MK results in annual precipitation showed a significant increasing trend in Motta station ($Z = 7.05$) while a significantly decreasing trend was observed in Nedjo station ($Z = -1.07$). A significant increasing trend was observed in average condition ($Z = 3.88$).

Sen's slope estimator test results of annual precipitation showed a significant increasing trend only in Bahir Dar station ($\beta = 5.71$) though other stations also showed positive values, with the exception of Nedjo station ($\beta = -0.46$) with a significant decreasing trend in Nedjo station ($\beta = -0.46$), and a significant increasing trend was observed in average condition ($\beta = 0.84$). The ITA results (Figure 8 and Table 6) show that the annual precipitation points fall between +10% to −10% lines, implying an overall downward trend at Nedjo station (Figure 8(d)), while it significantly increased at the Assosa (Figure 8(a)), Bahir Dar (Figure 8(b)), Gondar (Figure 8(c)), and Motta stations during 1986 to 2016 with respect to the 10% relative band (Figure 8).

3.4. Implication of Climate Change for Land Covers. As indicated in the previous sections of the paper, the temperature has increased by about 0.5°C during the period from 1980 to 2016 in the river basin. The biggest land cover change in the study area that has occurred is forest land cover, which had decreased pattern by 3429.62 km^2, and the water bodies were also decreased by 81.45 km^2. The changes were caused by climate variability, particularly increase in temperature as well as human activities in the region. Covers of cultivated land, grassland, bare land, wetland, and urban land in the study basin were increased from 2001 to 2013 as described above (Table 4). Water bodies were converted into wetland, forest land, and bare land by the area of 50.43 km^2, 11.75 km^2, and 21.30 km^2, respectively (Figure 4). The result of the study had indicated that land cover change is directly impacted by human activity. The vegetation covers in the river basin changed significantly in areas of intense human activities [43]. In the study area, deforestation had been taking place to some extent during the past decades, which was a major driving force for vegetation degradation. This consequently affects the climatic conditions of the study area. The effects of natural and human factors that affect land cover changes of the study area from 2001–2013 is described using a diagram shown in Figure 9.

4. Conclusions

In the study, the spatial and temporal land cover changes and vegetation evolution of the basin have been analyzed for the

Table 6: Trend test results of the mean precipitation in the subbasins based on ITAM (Φ), MK (Z), and Sen's slope estimator test (β) analysis.

S/No.	Name of stations	Z (MK)	Φ	β
1	Assosa	1.20*	5.87***	0.38
2	Bahir Dar	6.92***	28.91***	5.71***
3	Nedjo	−1.07*	0.02	−0.46***
4	Gondar	1.95*	1.88*	0.44
5	Motta	7.05***	14.82***	0.35
6	Average	3.88***	3.04***	0.84

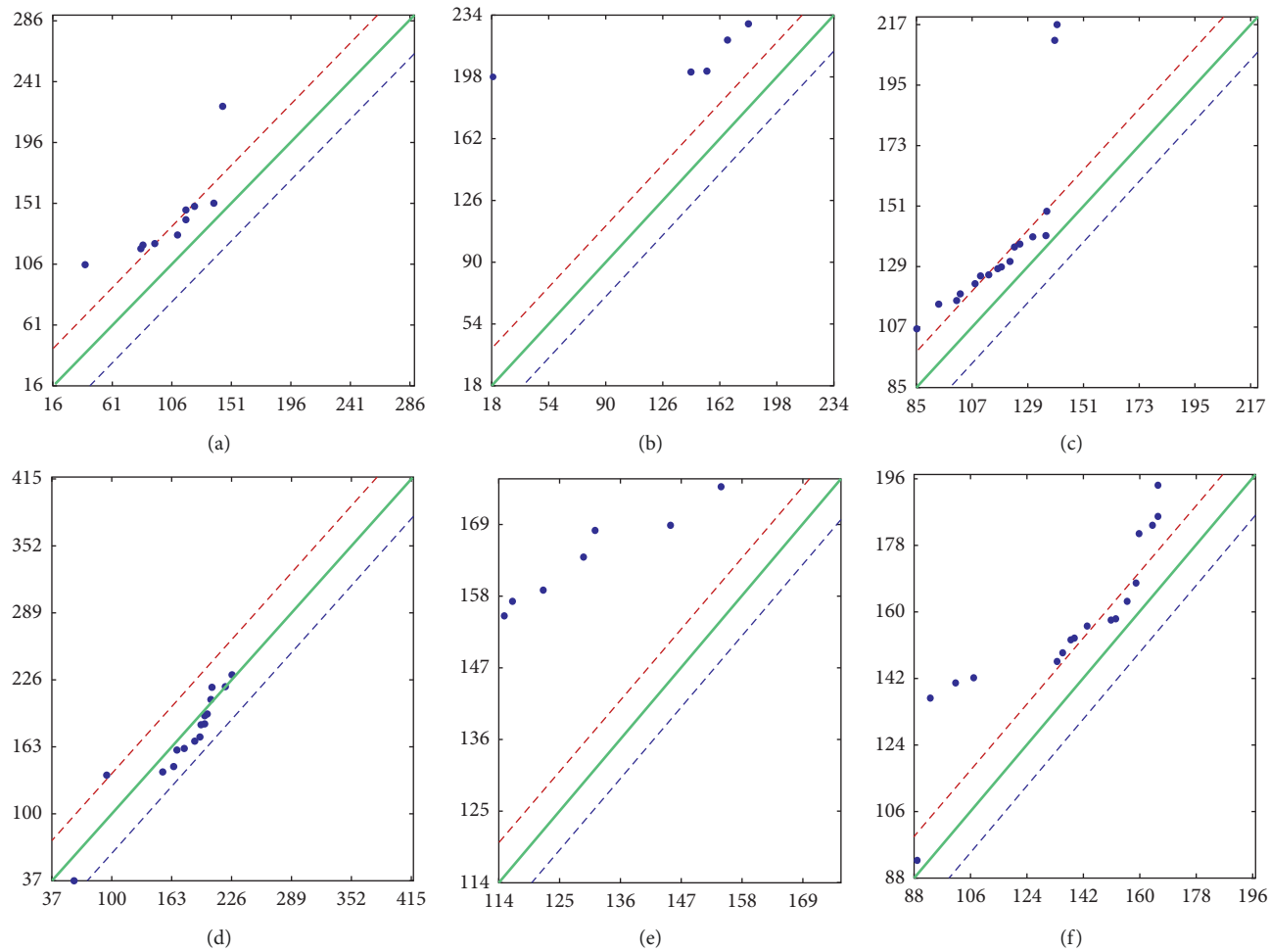

Figure 8: Results of ITA for annual precipitation during 1980–2016. (a) Assosa station. (b) Bahir Dar station. (c) Gondar station. (d) Nedjo station. (e) Motta station. (f) Average condition.

13-years period (2001 to 2013). The land cover changes that occurred in the study basin during the study period was deciphered using remote sensing, NDVI, EVI, and land classification methods and vegetation detection methods were employed to assess the change that comes in the study a period of 36 years (2001 to 2013). In the meantime, Mann–Kendall trend test, ITAM, and Sen's slope estimator test methods were used to analyze the variability of precipitation and temperature on annual basis in the study basin.

The result demonstrates that temperature has increased by 0.5°C while precipitation slightly changes in the river basin in a period spanning 1980 to 2016. The changes in climate change and particularly increment in air temperature was found as one of the driving forces for land cover change in the study area during this period. Analyses of the 13-years period (2001–2013) showed significant land cover changes in the study area. Land coverage of grassland, cultivated land, wetland, and urban and bare land showed a significant increase, whereas forest cover and water bodies decrease in the area. The changes in land cover were mainly caused by climate change and intense human socioeconomic activities in the region.

In the final analysis, land cover changes occurred in the Abbay River Basin during this time was statistically significant, and anthropogenic effects (human activity)

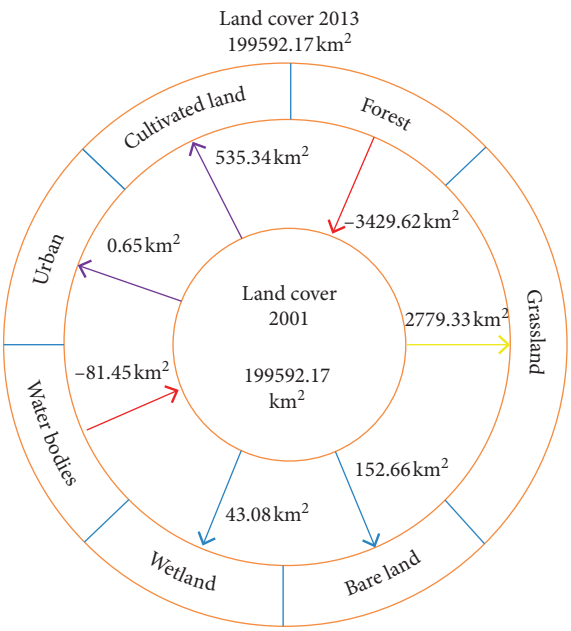

Figure 9: Diagram of natural, human, and climate impacts of land cover change of Abbey river basin in 2001–2013. Note: the arrows indicate a direction of gains and losses. The purple arrow indicates the impact of human activity which leads to the intensification of cultivation land and urbanization, the red arrow indicates the impact of the rise of temperature on the forest and water ecosystem, the yellow arrow indicates the impact of human and natural factor that has an influence on the natural ecosystem, and blue arrow indicates natural and other factors that have an impact on the ecosystem (Table 4).

and global and local climate were the major factors affecting, causing the shifts in land coverage profile. Thus, further research is warranted to study the potential influences of the land cover changes on hydro-ecological processes in the river basin that will have important implications to design sustainable development policies in the river basin.

Data Availability

The data used to support the findings of this study are available from the first author upon request.

Conflicts of Interest

The authors declare no conflicts of interest.

Authors' Contributions

A. A. and Y. D. were responsible for conceptualization; H. W. was involved in methodology; D. B., O. Y., and H. W. were responsible for software; A. G., M. G., and T. Q. were involved in validation; M. T. K. performed formal analysis; T. Q. investigated the study; A. G. was responsible for resources; M. G. was responsible for data source; A. A. wrote, reviewed, and edited the original draft; A. G. and D. B. were involved in visualization; Y. D. and X. S. supervised the study; H. W. was involved in project administration; T. Q. was responsible for funding acquisition.

Acknowledgments

The authors would like to thank the China Institute of Water Resources and Hydropower Research for financing this research and Donghua University. This research was funded by the National Key Research and Development Project (Grant no. 2016YFA0601503), China.

References

[1] J. Feng, D. Yan, C. Li, F. Yu, and C. Zhang, "Assessing the impact of climatic factors on potential evapotranspiration in droughts in North China," *Quaternary International*, vol. 336, pp. 6–12, 2014.

[2] D. Conway, "A water balance model of the upper blue Nile in Ethiopia," *Hydrological Sciences Journal*, vol. 42, no. 2, pp. 265–286, 1997.

[3] D. N. Yates and K. M. Strzepek, "Modeling the Nile basin under climatic change," *Journal of Hydrologic Engineering*, vol. 3, no. 2, pp. 98–108, 1998.

[4] R. A. Wurbs, R. S. Muttiah, and F. Felden, "Incorporation of climate change in water availability modeling," *Journal of Hydrologic Engineering*, vol. 10, no. 5, pp. 375–385, 2005.

[5] J. J. Lawler, D. J. Lewis, E. Nelson et al., "Projected land-use change impacts on ecosystem services in the United States," *Proceedings of the National Academy of Sciences*, vol. 111, no. 20, pp. 7492–7497, 2014.

[6] S. G. Gebrehiwot, W. Bewket, A. I. Gärdenäs, and K. Bishop, "Forest cover change over four decades in the blue Nile basin, Ethiopia: comparison of three watersheds," *Regional Environmental Change*, vol. 14, no. 1, pp. 253–266, 2014.

[7] D. E. Pozen, "The mosaic theory, national security, and the freedom of information act," *The Yale Yellow Journal*, vol. 155, 2005.

[8] M. Bekele, "Forest property rights, the role of the state, and intitutional exigency the Ethiopian experience," Doctoral thesis, Swedish University of Agricultural Science, Uppsala, Sweden, 2003.

[9] R. S. DeFries, T. Rudel, M. Uriarte, and M. Hansen, "Deforestation driven by urban population growth and agricultural trade in the twenty-first century," *Nature Geoscience*, vol. 3, no. 3, pp. 178–181, 2010.

[10] G. Li, F. Zhang, Y. Jing, Y. Liu, and G. Sun, "Response of evapotranspiration to changes in land use and land cover and climate in China during 2001–2013," *Science of The Total Environment*, vol. 596-597, pp. 256–265, 2017.

[11] E. Haile and M. Assefa, "The impact of land use change on the hydrology of the Angereb watershed, Ethiopia," *International Journal of Water Sciences*, vol. 1, p. 1, 2012.

[12] G. T. Eshete, "Biodiversity and livelihoods in southwestern Ethiopia: forest loss and prospects for conservation in shade coffee agroecosystems," UC Santa Cruz, Santa Cruz, CA, USA, Doctoral dissertation, 2013.

[13] N. Haregeweyn, A. Tsunekawa, M. Tsubo et al., "Analyzing the hydrologic effects of region-wide land and water development interventions: a case study of the upper blue Nile basin," *Regional Environmental Change*, vol. 16, no. 4, pp. 951–966, 2016.

[14] M. K. Emily Schmidt, "Urbanization and spatial connectivity in Ethiopia: urban growth analysis using GIS," International

Food Policy Research Institute, Washington, DC, USA, ESSP2 Discussion Paper 003, 2009.

[15] J. Kearney, "Food consumption trends and drivers," *Philosophical Transactions of the Royal Society B: Biological Sciences*, vol. 365, no. 1554, pp. 2793–2807, 2010.

[16] M. Blumstein and J. R. Thompson, "Land-use impacts on the quantity and configuration of ecosystem service provisioning in Massachusetts, USA," *Journal of Applied Ecology*, vol. 52, no. 4, pp. 1009–1019, 2015.

[17] A. D. Yilma and S. B. Awulachew, "Characterization and atlas of the blue Nile basin and its sub basins," *Atlas*, 2009.

[18] S. Tekleab, Y. Mohamed, and S. Uhlenbrook, "Hydro-climatic trends in the abay/upper blue Nile basin, Ethiopia," *Physics and Chemistry of the Earth, Parts A/B/C*, vol. 61-62, pp. 32–42, 2013.

[19] U. Kim and J. J. Kaluarachchi, "Climate change impacts on water resources in the upper blue Nile river basin, Ethiopia1," *JAWRA Journal of the American Water Resources Association*, vol. 45, no. 6, pp. 1361–1378, 2009.

[20] T. Abate and A. Angassa, "Conversion of savanna rangelands to bush dominated landscape in Borana, Southern Ethiopia," *Ecological Processes*, vol. 5, no. 1, p. 6, 2016.

[21] B. Dorjsuren, D. Yan, H. Wang et al., "Observed trends of climate and land cover changes in Lake Baikal basin," *Environmental Earth Sciences*, vol. 77, no. 20, p. 725, 2018.

[22] M. Gebreyes, "Assessing the effectiveness of planned adaptation interventions in reducing local level vulnerability. Adapting to climate change in the water sector," Working Paper 18, 2010.

[23] A. O. Owojori, "Landsat image-based lulc changes of San Antonio, Texas using advanced atmospheric correction and object-oriented image analysis approaches," *Remote Sensing Image Processing and Analysis (ES 6973)*, 2005.

[24] A. Butt, R. Shabbir, S. S. Ahmad, and N. Aziz, "Land use change mapping and analysis using remote sensing and GIS: a case study of simly watershed, Islamabad, Pakistan," *The Egyptian Journal of Remote Sensing and Space Science*, vol. 18, no. 2, pp. 251–259, 2015.

[25] R. Manandhar, I. O. A. Odeh, and T. Ancev, "Improving the accuracy of land use and land cover classification of Landsat data using post-classification enhancement," *Remote Sensing*, vol. 1, no. 3, pp. 330–344, 2009.

[26] K. Gwet, "Kappa statistic is not satisfactory for assessing the extent of agreement between raters," *Statistical Methods For Inter-Rater Reliability Assessment*, no. 1, 2002.

[27] S. N. Goward, B. Markham, D. G. Dye, W. Dulaney, and J. Yang, "Normalized difference vegetation index measurements from the advanced very high resolution radiometer," *Remote Sensing of Environment*, vol. 35, no. 2-3, pp. 257–277, 1991.

[28] S. Yue and C. Wang, "The Mann-Kendall test modified by effective sample size to detect trend in serially correlated hydrological series," *Water Resources Management*, vol. 18, no. 3, pp. 201–218, 2004.

[29] J. W. Rouse, H. R. Haas, J. A. Scheel, and D. W. Deering, "Monitoring vegetation systems in the great plains with ERTS NASA," in *Proceedings of the Goddard Space Flight Center 3d ERTS-1 Symposium*, vol. 1, pp. 309–317, Washington, DC, USA, January 1974.

[30] Z. Şen, "Trend identification simulation and application," *Journal of Hydrologic Engineering*, vol. 19, no. 3, pp. 635–642, 2014.

[31] L. Cui, L. Wang, Z. Lai, Q. Tian, W. Liu, and J. Li, "Innovative trend analysis of annual and seasonal air temperature and rainfall in the Yangtze river basin, China during 1960–2015," *Journal of Atmospheric and Solar-Terrestrial Physics*, vol. 164, pp. 48–59, 2017.

[32] O. Kisi, "An innovative method for trend analysis of monthly pan evaporations," *Journal of Hydrology*, vol. 527, pp. 1123–1129, 2015.

[33] Z. Şen, "Innovative trend analysis methodology," *Journal of Hydrologic Engineering*, vol. 17, no. 9, pp. 1042–1046, 2012.

[34] B. Dorjsuren, D. Yan, H. Wang et al., "Observed trends of climate and river discharge in Mongolia's Selenga sub-basin of the lake Baikal basin," *Water*, vol. 10, no. 10, p. 1436, 2018.

[35] H. B. Mann, "Nonparametric tests against trend," *Econometrica*, vol. 13, no. 3, pp. 245–259, 1945.

[36] M. Gedefaw, H. Wang, D. Yan et al., "Trend analysis of climatic and hydrological variables in the Awash river basin, Ethiopia," *Water*, vol. 10, no. 11, p. 1554, 2018.

[37] M. Gedefaw, D. Yan, H. Wang et al., "Innovative trend analysis of annual and seasonal rainfall variability in Amhara regional state, Ethiopia," *Atmosphere*, vol. 9, no. 9, p. 326, 2018.

[38] Atta-ur-Rahman and M. Dawood, "Spatio-statistical analysis of temperature fluctuation using Mann–Kendall and Sen's slope approach," *Climate Dynamics*, vol. 48, no. 3-4, pp. 783–797, 2017.

[39] A. A. Akinsanola and K. O. Ogunjobi, "Recent homogeneity analysis and long-term spatio-temporal rainfall trends in Nigeria," *Theoretical and Applied Climatology*, vol. 128, no. 1-2, pp. 275–289, 2017.

[40] F. Liu, T. Qin, A. Girma et al., "Dynamics of land-use and vegetation change using NDVI and transfer matrix: a case study of the Huaihe river basin," *Polish Journal of Environmental Studies*, vol. 28, no. 1, pp. 213–223, 2018.

[41] Y. Arsano and I. Tamrat, "Ethiopia and the Eastern Nile basin," *Aquatic Sciences*, vol. 67, no. 1, pp. 15–27, 2005.

[42] V. S. Seleshi Bekele Awulachew and D. P. David Molden, *The Nile River Basin Water, Agriculture, Governance And Livelihoods*, Routledge, New York, NY, USA, 2012.

[43] D. H. Yan, H. Wang, H. H. Li et al., "Quantitative analysis on the environmental impact of large-scale water transfer project on water resource area in a changing environment," *Hydrology and Earth System Sciences*, vol. 16, no. 8, pp. 2685–2702, 2012.

Hindawi
Advances in Meteorology
Volume 2019, Article ID 7525479, 11 pages
https://doi.org/10.1155/2019/7525479

Research Article

Spatiotemporal Evolution of Atmospheric Ammonia Columns over the Indo-Gangetic Plain by Exploiting Satellite Observations

Aimon Tanvir,[1] Muhammad Fahim Khokhar,[1] Zeeshan Javed,[2] Osama Sandhu,[1] Tehreem Mustansar,[1] and Asadullah Shoaib[1]

[1]*Institute of Environmental Sciences and Engineering, National University of Sciences and Technology, Islamabad 44000, Pakistan*
[2]*School of Earth and Space Sciences, University of Science and Technology of China, Hefei 230026, China*

Correspondence should be addressed to Muhammad Fahim Khokhar; fahim.khokhar@iese.nust.edu.pk and Zeeshan Javed; zeeshan@mail.ustc.edu.cn

Received 21 March 2019; Accepted 13 June 2019; Published 1 July 2019

Guest Editor: Salman Tariq

This study was aimed at presenting a continuous and spatially coherent picture of ammonia (NH_3) distribution over the Indo-Gangetic Plain (IGP) by exploiting satellite observations. Atmospheric columns of ammonia were mapped over South Asia by using TES observations on board NASA's Aura satellite. Monthly mean data were used to identify emission sources of atmospheric ammonia across the South Asian region. Data were analysed to explore temporal trends, seasonal cycles, and hot spots of atmospheric ammonia within the study area. The results show that the IGP region has the most ammonia concentrations in terms of column densities, and hence this region has been identified as an ammonia hot spot. This is attributed majorly to extensive agricultural activity. Time series showed a slight increase in ammonia column densities over the study area from 2004 to 2011. Different seasonal cycles were identified across the IGP region with maximum NH_3 columns observed during the month of July in most of the subregions. Seasonality in an ammonia column is driven by different cropping patterns and meteorological conditions in the IGP subregions. Global emission inventories of atmospheric ammonia were largely overestimating as compared to satellite observations.

1. Introduction

Ammonia (NH_3) is a highly reactive and soluble alkaline gas [1] in the atmosphere having a short lifetime of 1 day [2, 3] and plays an important role in several environmental processes and their consequent impacts. In terrestrial ecosystems, excess nitrogen causes soil acidification and loss of plant diversity [4], whereas in aquatic systems, it is responsible for eutrophication and algal blooms [5]. In the atmosphere, ammonia combines with other gases and causes the formation of fine particulates which are hazardous to human health [6]. Reactions with other pollutants like oxides of sulphur lead to the formation of fine particulates [7]. Reactions with primary pollutants, like oxides of nitrogen and sulphur as well as HCl, cause the formation of ammonium ions (NH_4^+). The ammonium ions consequently form the sulphates and nitrates, a major component of atmospheric aerosols [3, 8].

Large uncertainties exist in atmospheric emissions, chemistry, transport, and deposition of nitrogen compounds such as ammonia [9]. Agriculture sector is considered as the greatest source contributing to global atmospheric ammonia [10]. However, the influence of agriculture activities fluctuates greatly at smaller spatial scales. It has been estimated that about 57% of global atmospheric ammonia is released from livestock and crops [11], whereas the estimates during the year 2008 showed that about 49.3 Tg was emitted in the atmosphere, out of which 81% was related to agriculture including agricultural soils, manure management, and agricultural burning. Vegetation fires have been attributed to

the second most important source contributing to 16% of the total emissions [9]. Relative contribution and importance of these sources can vary on both local and regional scales.

Anthropogenic activities are the primary source for causing disruptions in the natural nitrogen cycle [8, 12] by enhancing ammonium deposition instead of nitrates. Mainly, the production of food and energy to meet the growing needs of the ever-increasing population leads to the disturbance of natural cycles of carbon and nitrogen. The deposition of ammonia and ammonium ions, either dry or wet, plays a significant part to impart adverse effects to sensitive ecosystems [12–14].

Ammonia regions with enhanced levels of fine particulate matter have been associated statistically with increased number of humans suffering pulmonary and cardiac diseases [15]. These fine particles also cause radiative force in the atmosphere [16] as well as reduce the visibility.

A single nitrogen atom (reactive nitrogen) while moving through the steps of its biogeochemical cycle can have a sequence of negative impacts [17]. These multiple effects can be observed in the atmosphere as well as in terrestrial, freshwater, and marine ecosystems with implications on human health as well and are termed as "Nitrogen Cascade".

Using observation from the tropospheric emission spectrometer (TES aboard Aura satellite), Beer et al. [18] gave the first account of boundary layer ammonia. The infrared atmospheric sounder interferometer (IASI), like TES, also retrieves ammonia in nadir viewing. For its retrieval, the IASI uses the spectrum which falls in the thermal infrared region. A clear picture of ammonia concentration over the globe has been obtained by the excellent coverage provided by the IASI instrument, along with simple measurements which are obtained by converting brightness temperature difference to total column measurements [10]. The TES has less spatial coverage compared to other satellite-based instruments like AIRS or IASI, but it has a higher spectral resolution of 0.1 per·cm. This property, in combination with a higher signal-to-noise ratio (600 : 1) of the TES instrument, provides sufficient sensitivity towards the boundary layer ammonia [9, 11]. An additional feature of the TES is the sun-synchronous orbit and has the ability to provide optimum conditions for high thermal contrast ultimately increasing the sensitivity towards ammonia [18]. Furthermore, high spectral resolution allows the selection of microwindows (spectral regions) with minimum interference from other atmospheric absorbers, thus reducing the systemic errors in the retrievals.

Despite all this, the knowledge about atmospheric abundances of ammonia and its spatial and seasonal variability is very limited. To account for variability in ammonia on spatial and temporal scales is mandatory in order to quantify its emissions, concentrations, and deposition [9]. It will also improve understanding about the fine particulate matter in the atmosphere.

The present paper describes the spatial and temporal distribution of ammonia over the South Asian region during the time period of 2004–2011. South Asia is home to 25% of the world's population. The continent is famous for its fertile plains hosting extensive agricultural activities. Owing to the growing population and urbanization, South Asia is undergoing transformations in almost all the sectors of development. Agriculture sector is the backbone of this region. The primary objective was to explore the spatio-temporal patterns of ammonia columns over the study region and to identify the ammonia hot spots. This study also investigates the contribution of various ammonia sources and tries to interpret the role of agricultural activities and meteorological parameters in observed ammonia columns.

2. Materials and Methods

The data used in the present study were acquired from the tropospheric emission spectrometer (TES) aboard NASA's Aura satellite. The TES has the capacity to measure a wide variety of atmospheric pollutants such as CO, ozone, water vapours, ammonia, and methanol [11, 19, 20], along with the standard products that are retrieved operationally.

The instrument has the capability to measure in both limb (side view) and nadir (straight down) viewing. It has an altitude coverage of 0 to 34 km with higher spectral resolution from 5.3 to 15.4 μm. It scans over a swath of 5.3×8.5 km with rectangular pixel size of 0.53×5.3 km and allows for the detection of localized sources. The satellite revolves in a sun-synchronous orbit at an altitude of about 705 km and possesses a good signal-to-noise ratio of 600 : 1 [11]. One of the species that can additionally be retrieved is ammonia [9]. For the current study, level 2 data were obtained on a monthly basis from September 2004 to December 2011 and were subjected to further processing.

The satellite data in raw form were subjected to various processing steps as shown in the methodology flow chart (Figure 1). The data were available with global coverage; however, ammonia total columns were extracted over the South Asian region by using ArcGIS tools. Finally, monthly mean maps were generated over South Asia and each country and various regions like the Indo-Gangetic Plain and provinces of Pakistan. Maps were generated using ArcMap 10.3.1. These were monthly maps with extractions over South Asia, provinces of Pakistan, and IGP regions. Furthermore, seasonal mean for Rabi and Kharif cropping periods in addition to annual and long-year maps were generated. Spatiotemporal analysis was performed, and the results are represented graphically and statistically in the following sections.

The fertilizer use data for various months and seasons were obtained from the National Fertilizer Development Centre, Pakistan. These data were linked to the emissions of ammonia in Pakistan. The emissions were also correlated with temperature and precipitation trends in the region.

3. Results and Discussion

3.1. Spatial Distribution of Ammonia across South Asia. South Asia is famous for its fertile plains hosting extensive agricultural activities. Owing to the growing population and urbanization, South Asia is undergoing transformations in almost all the sectors of development. Spatial distribution of

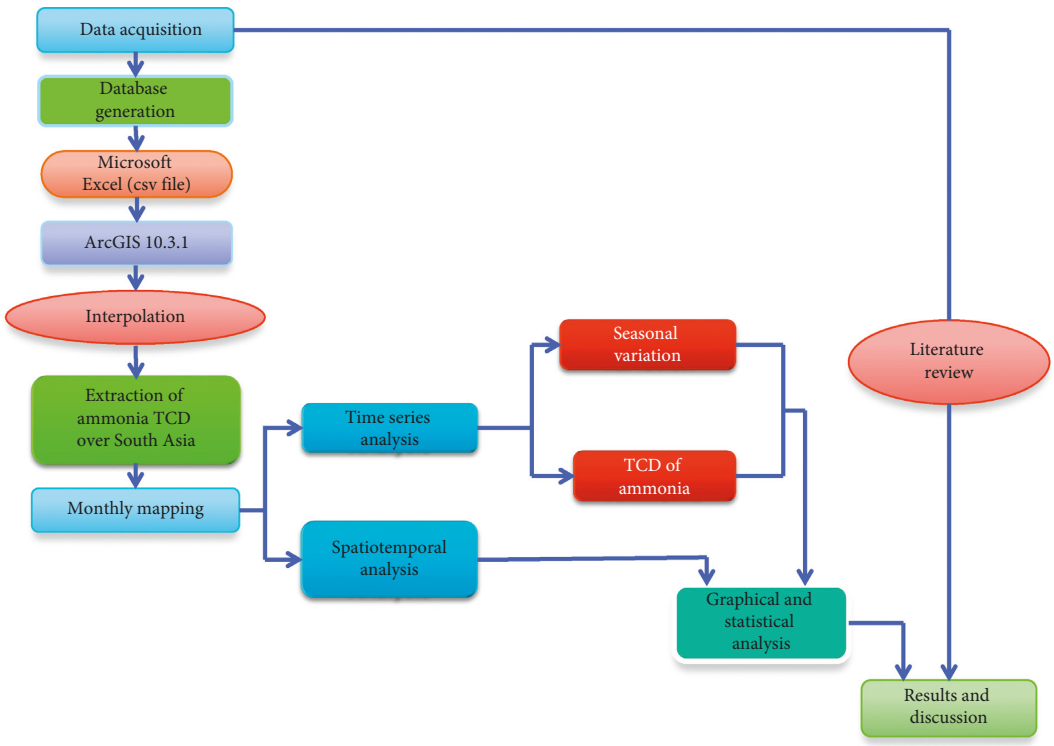

Figure 1: Methodology flow chart exhibiting the datasets, procedure, and tools used in this study.

ammonia column densities across South Asia averaged over the period of year 2004–2011 is presented in Figure 2. It is evident that the ammonia columns are higher in the area marked by red polygons. The area marked by red polygons basically consists of plains of the Indus and Ganges river basins. This area is generally known as the Indo-Gangetic Plain (IGP). The plain extends from the Arabian Sea to the Bay of Bengal and from the Himalayan foothills to the Indian peninsula. The region covers a total of 21% of the geographic area of India, 14% of the territory of Nepal, 24% of the area of Pakistan, and 100% of the area of Bangladesh. The IGP region is prominent as the world's largest food basket and hosts extensive agriculture activities. The main causes of NH3 emissions are the production and use of ammonia-based fertilizers [6]. Enhanced NH_3 columns over the IGP region are in compliance with the speculated ammonia emissions of the agriculture sector [6, 12].

3.2. Temporal Analysis. Temporal analysis of ammonia columns from South Asia is presented in Figure 3. Monthly means of ammonia columns retrieved from TES observations over South Asia during the time period of September 2004 to September 2011 were used. An overall relative change of 6% is observed during the study period. Time series has exhibited certain seasonality in the observed ammonia columns with maximum during the summer months. The values have been observed to rise during the months of June-July and December every year, although the anomalies do exist sometimes. This can be attributed to fertilizer intake for rice crop in summer and wheat crops during the months of December-January.

3.3. Trends in Ammonia Columns over IGP Regions. Climate in the IGP ranges from warm temperate to subtropical. The region is characterized by winter season which is cool and dry, while summer that is warm and humid. The IGP has been subdivided into six major subregions shown in Figure 4 depending upon the physiography and bioclimate [21]. Trans-Gangetic Plain (transects 1A and 1B) occupy large areas of Pakistan and Punjab and Haryana (transect 2) in India. Transects 3 and 4 comprise areas in Uttar Pradesh, Bihar, and Nepal. Lower parts of the Gangetic Plain in West Bengal, India, and parts of Bangladesh constitute transect 5 [22].

It has been observed that the general trend in ammonia column densities for the regions 1A, 1B, 2, and 3 is more or less the same with peaks observed during June-July. While for the regions 4 and 5, the trend is different from the others with peaks during the months of January and February, respectively. The time series for all these regions has been depicted in Figure 5. This dissimilarity can be attributed due to difference in crop seasons across the Indo-Gangetic Plain.

3.4. Analysis of Crop Seasons. Two distinct crop seasons exist in the IGP: Rabi and Kharif. The ammonia columns show prominent difference during these two seasons. This has been depicted by the time series presented in Figure 6.

It shows that the trend of ammonia columns increases during Kharif months in the IGP with the exception of the last two regions (Zone 4 and Zone 5) with a few exceptions (IGP-3 in 2005 and IGP-5 in 2010). Further analyses revealed that IGP subregions 1a, 1b, 2, and 3 host almost similar cropping seasons (with an offset of about few days

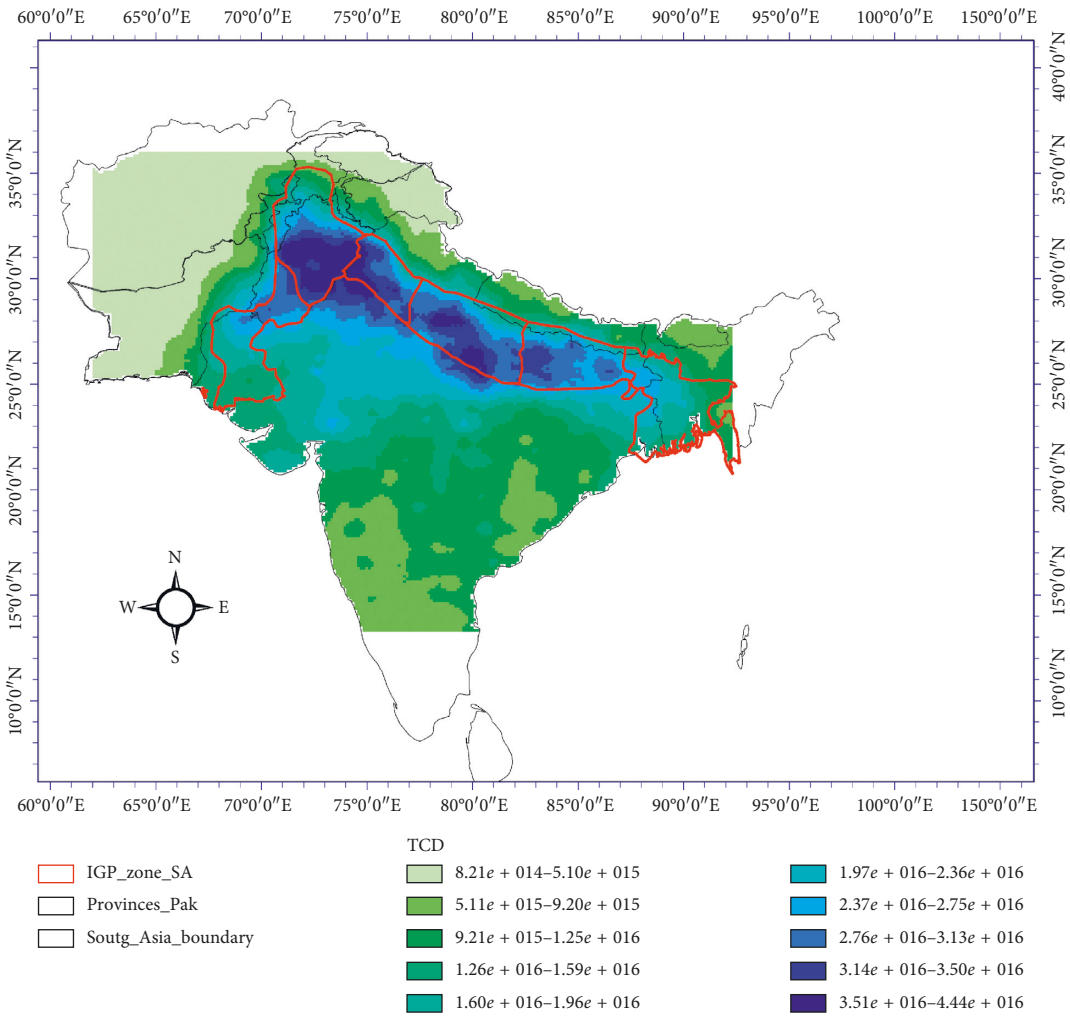

Figure 2: Average map of NH_3 columns (molecules/cm^2) for years 2004–2011 over South Asia. Red polygons indicate the subregions of the Indo-Gangetic Plain (IGP).

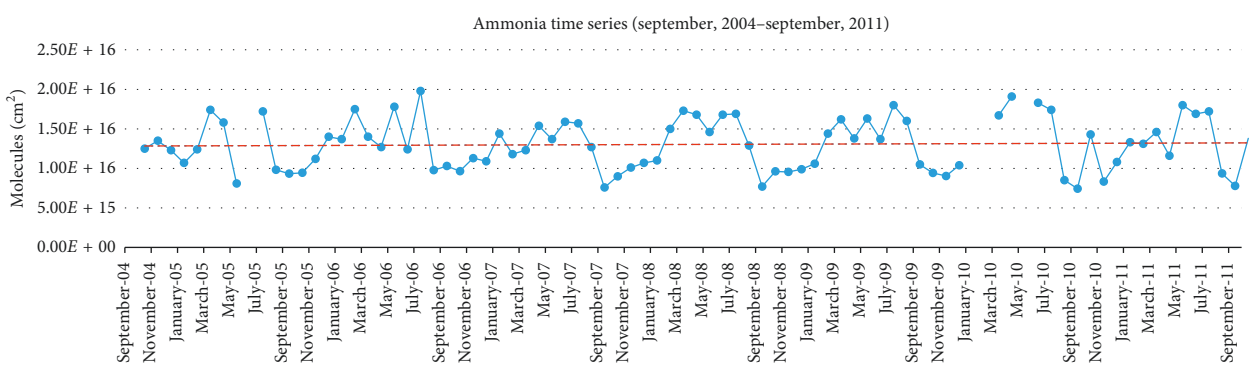

Figure 3: Time series of ammonia columns (molecules/cm^2) over South Asia showing high peak over the month of July and a slight rise from 2004 to 2011.

from east to west), climate, and precipitation patterns as compared to subregions 4 and 5. The precipitation pattern as observed in IGP subregions 2 to 5 (India and Bangladesh) has been depicted in Figure 7 [23].

It exhibited maximum precipitation during Kharif season in IGP subregions 4 and 5 as compared to subregions 2 and 3. It can be speculated that due to heavy rains with consequent stagnant water and humid conditions during Kharif season, comparatively limited agriculture activities are happening as compared with other subregions in the IGP. It was further supported by the SPOT vegetation data presented in Figure 8. It depicts the level of agriculture

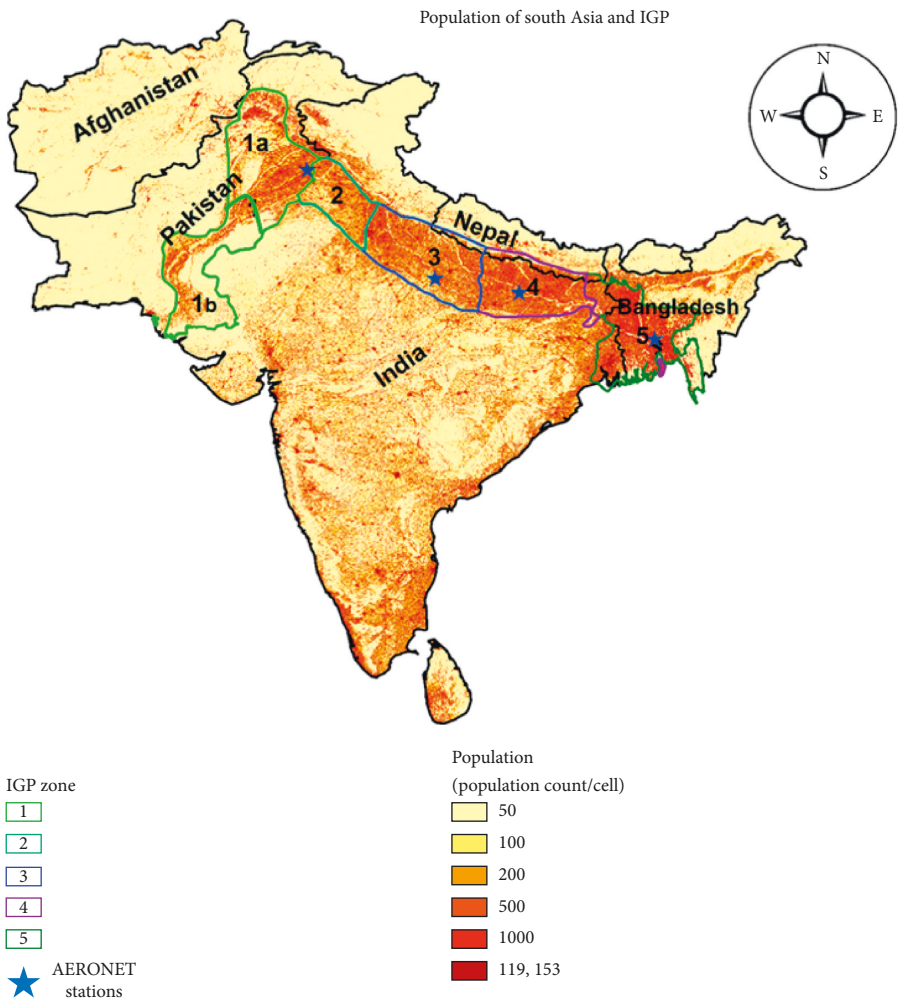

Figure 4: Six major subregions of the IGP based on population density, adopted from Khokhar and Yasmin, 2018.

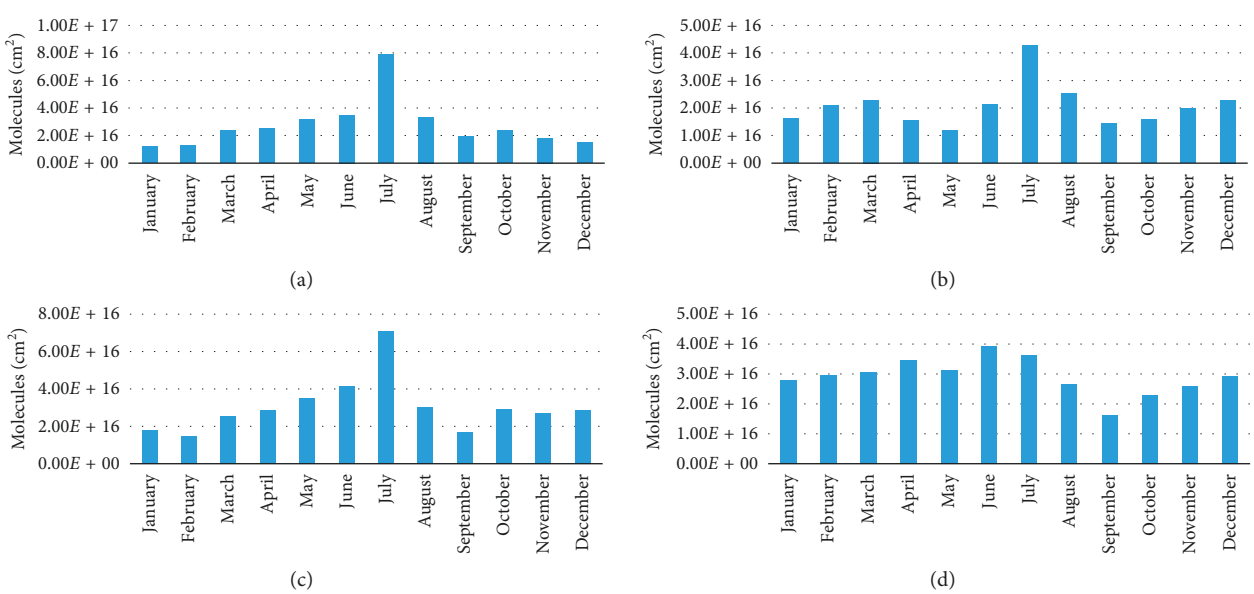

Figure 5: Continued.

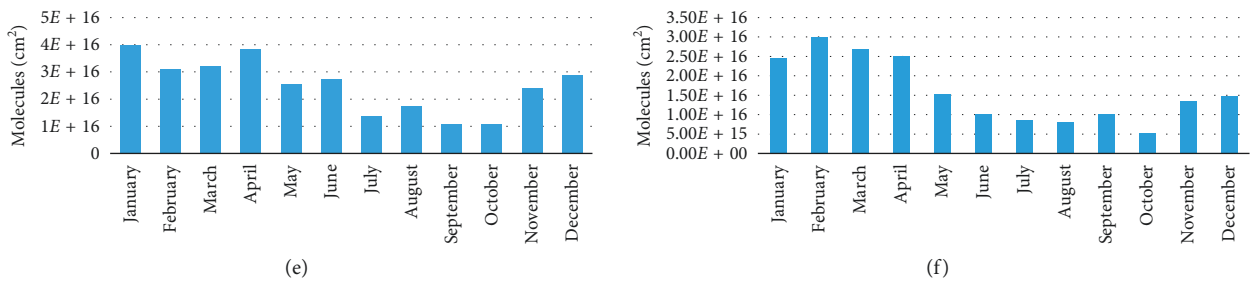

Figure 5: Seasonal variations of ammonia columns (molecules/cm^2) over different regions of the study area. The trend over IGP-4 and IGP-5 shows discrepancy from the observed normal for the other regions. (a) IGP-1A. (b) IGP-1B. (c) IGP-2. (d) IGP-3. (e) IGP-4. (f) IGP-5.

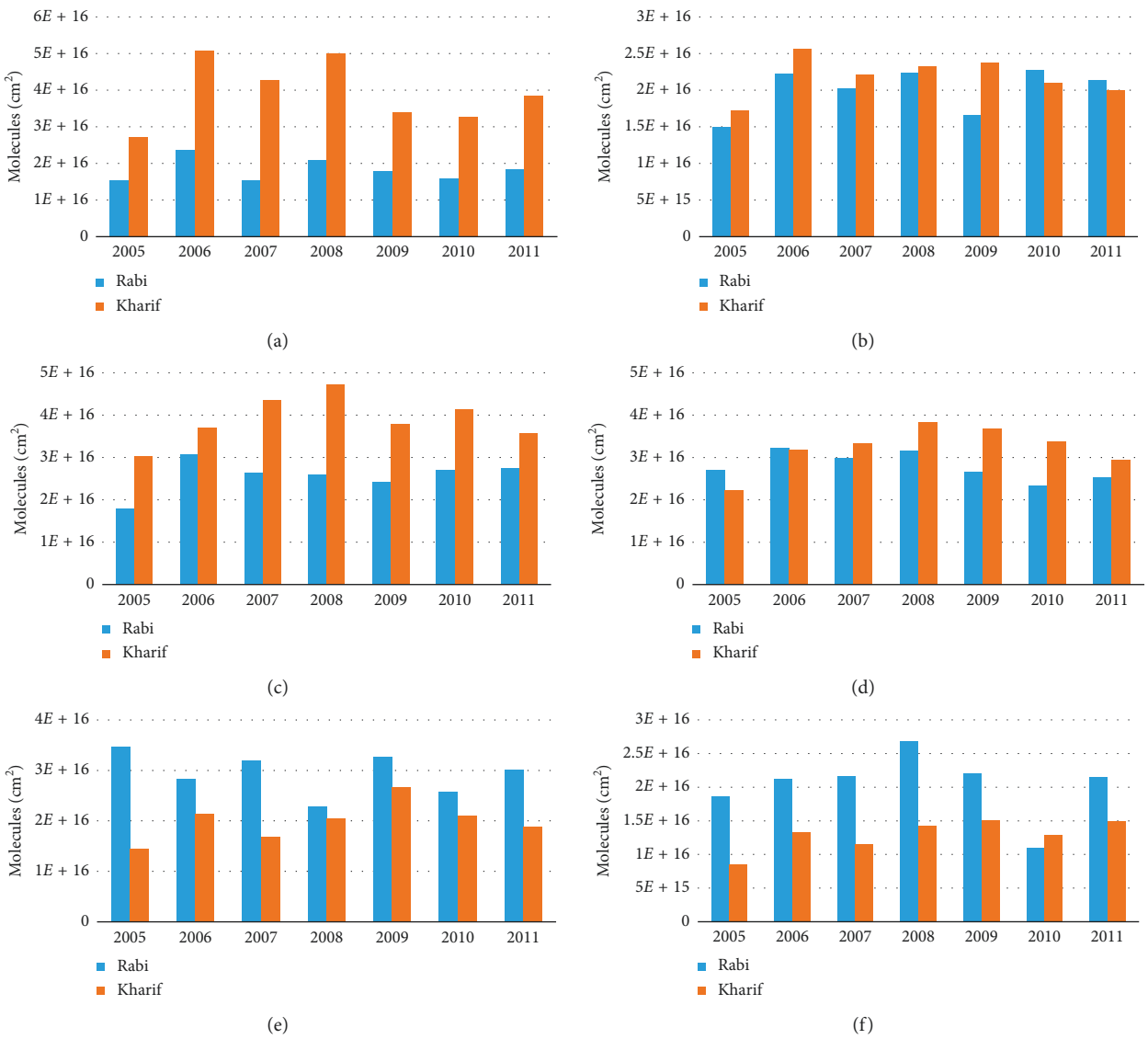

Figure 6: Rabi versus Kharif columns (molecules/cm^2) for the IGP regions plotted side by side shows that Kharif emissions are generally higher compared to Rabi emissions for the first four regions and are lower in case of IGP-4 and IGP-5. (a) IGP-1A. (b) IGP-1B. (c) IGP-2. (d) IGP-3. (e) IGP-4. (f) IGP-5.

activities (no/low agriculture: pink; areas with medium agriculture: yellow; areas with extensive agriculture: green) within the study region for both Kharif (Figure 8(a)) and Rabi (Figure 8(b)) seasons in the IGP. It is evident from Figure 8 that subregions 4 and 5 host very low agriculture activities during Kharif season as compared to other regions

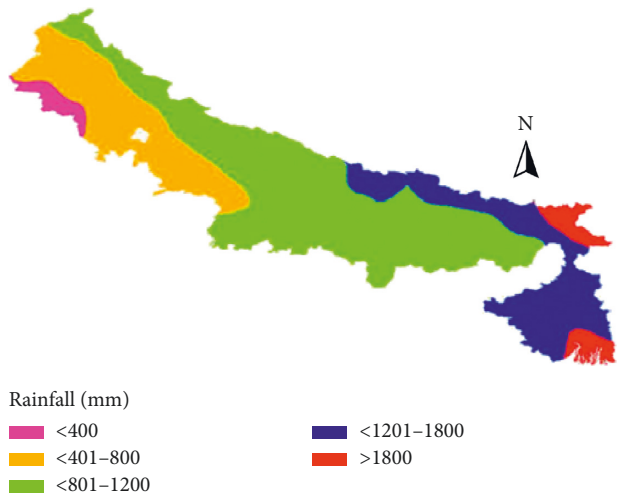

Figure 7: Precipitation over the IGP: the colours depict the level of monsoon rains (Kharif) over the Indian and Bangladeshi parts of the IGP as adopted from Koshal (2014).

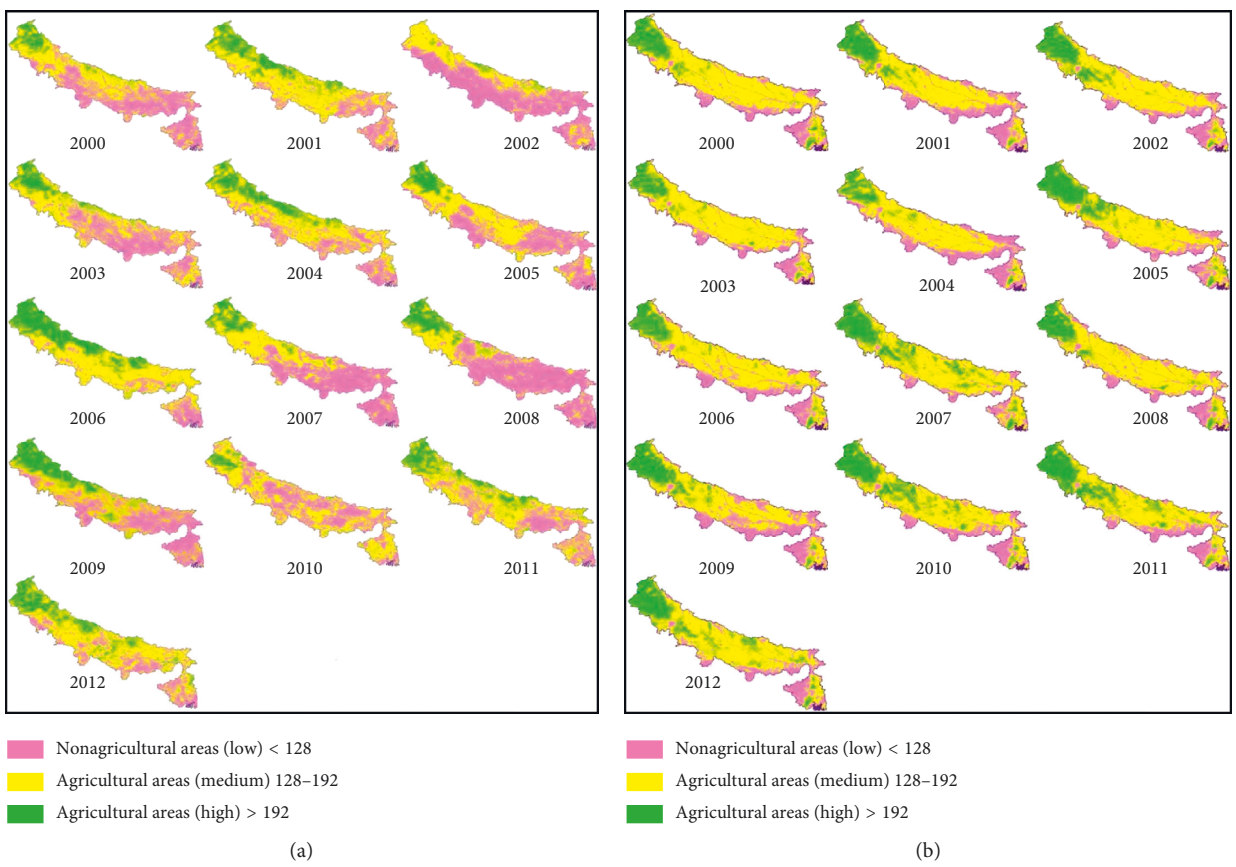

Figure 8: SPOT vegetation over the IGP for Kharif (a) and Rabi (b) as adopted from Koshal, 2014.

of the IGP. The corresponding decline in ammonia emissions during these months as depicted in Figure 6 for these regions validates the hypothesis adopted for this study that ammonia emissions in this region predominantly come from agriculture.

It justifies the different trends obtained for subregions 4 and 5. Also, there were some exceptions observed for subregion 3 during the year 2005. It was further investigated by comparing vegetation during both seasons in the year 2005. It revealed that more agriculture activity was carried out in Rabi in 2005 than that in Kharif season in subregion 3. Similarly, during the year 2010, in subregion 5, anomalous high vegetation was observed during the Kharif season than that during Rabi season as shown in Figure 8. Reason behind

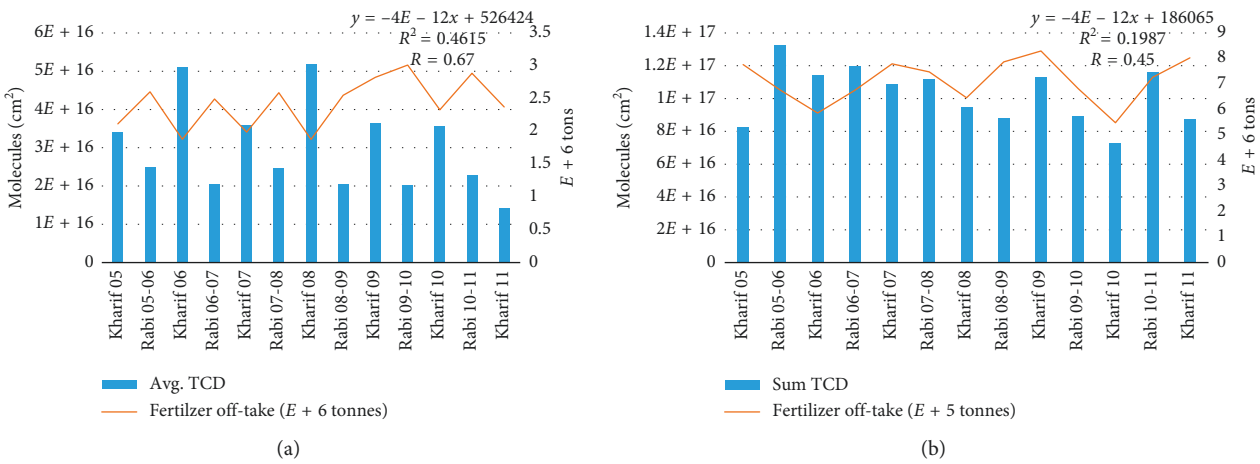

Figure 9: Total column density of ammonia (molecules/cm^2) versus total fertilizer offtake (tons) as obtained from the National Fertilizer Development Centre, Pakistan, for the provinces majorly falling under the IGP. (a) Punjab. (b) Sindh.

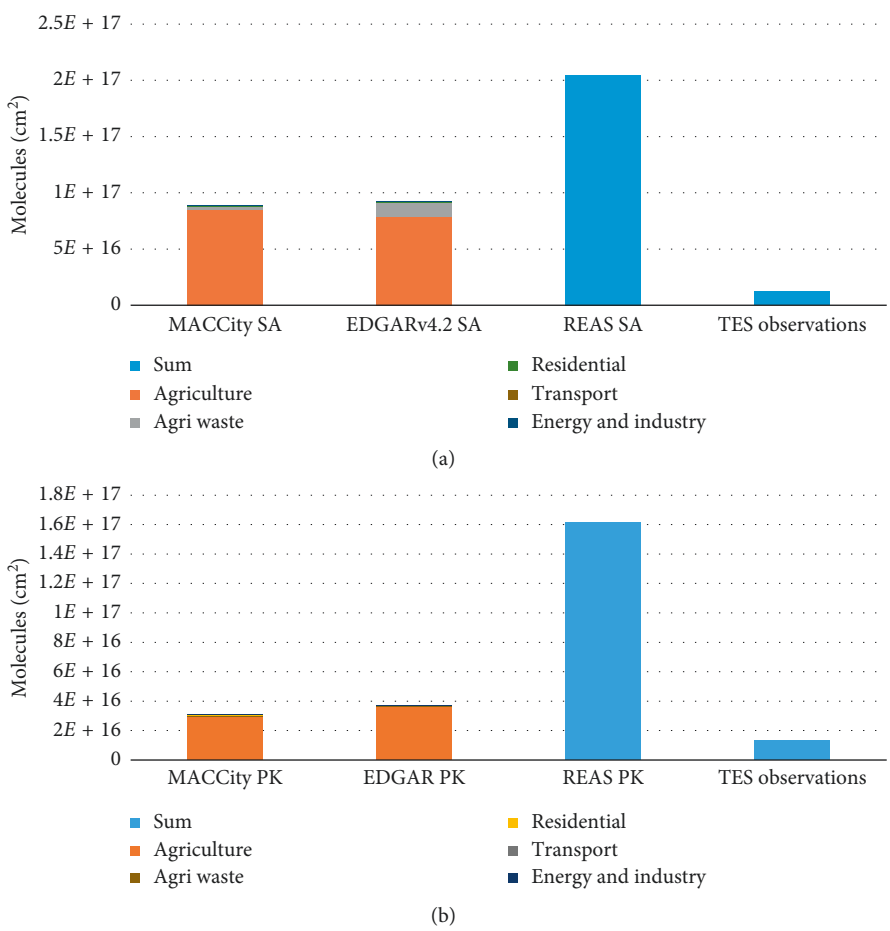

Figure 10: Continued.

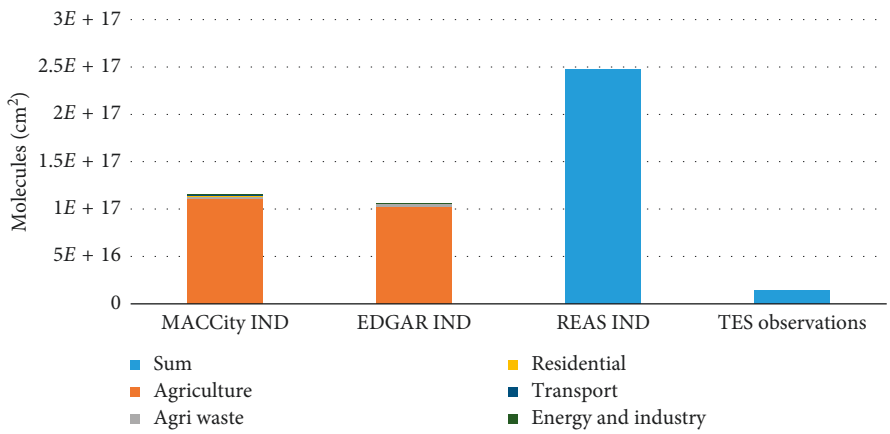

(c)

Figure 10: Calculated values for ammonia column densities (molecules/cm^2) from the regional and global inventories (MACCity, EDGAR, and REAS) against observed values from the TES instrument on the Aura satellite over (a) South Asia, (b) Pakistan, and (c) India.

such an anomaly is not clear yet; however, it can be attributed to relatively less rains during 2010 in subregion 5.

4. Fertilizer Offtake and Regional Ammonia Columns

One of the major factors involved in ammonia emissions is the use of ammonia-based fertilizers [24]. The data obtained from the National Fertilizer Development Centre, Pakistan, have been statistically analysed over the agriculture-intensive areas of Punjab and Sindh provinces (subregions 1a and 1b, respectively). The comparison between fertilizer intake and atmospheric ammonia columns is depicted in Figure 9.

These illustrations show that ammonia columns and fertilizer offtake are reasonably correlated. At times, the NH_3 column density happens to increase with increasing fertilizers, while the reverse also occurs at other points. It is not possible to look for exact correlations between these two datasets as they are not harmonious in space and time. First, the satellite observations from a single point on the globe are taken every sixteen days which is not consistent with the fertilizer offtake data obtained from the National Fertilizer Development Centre. Furthermore, ammonia has a short life span of about 2–10 days [2] which makes it difficult to be traced by TES observations with such high precision levels.

4.1. Monitored vs. Calculated Ammonia Columns. There has been observed a wide difference between the amounts of ammonia column densities as measured by TES and that of calculated using the data from the global emission inventories. The satellite largely underestimates the ammonia emissions. The most probable reason for this difference is that ammonia has a lifetime of about 5 days, while the satellite observes it after every 16 days, leaving majority of the emissions undetected. REAS observations are overestimated as compared to MACCity and EDGAR v4.0 exhibiting relatively less difference with TES observations. REAS does not give any source contribution for the emissions and just gives an idea of total ammonia emissions. This might have caused ambiguities in its results. Furthermore, REAS is a regional inventory, and all the emission inventories differ from each other. For instance, EDGAR overestimates the emissions from agriculture wastes. The comparison of these inventories with the satellite has been shown in Figure 10 for (a) South Asia, (b) Pakistan, and (c) India.

5. Conclusions

Extensive agricultural activity with more use of synthetic fertilizers is one of the pronounced causes of ammonia emissions in the atmosphere. The time series generated for the various regions of the study area clearly depicted that the ammonia column density is higher over the agriculture-intensive areas of South Asia, commonly termed as the Indo-Gangetic Plain. The results show a 6% in overall ammonia columns over the study region with pronounced seasonality, which is maximum during the month of July every year, with few exceptions over some regions (IGP-4, 5). Analyses for different crop seasons showed higher Kharif emissions than Rabi emissions for some agricultural regions (IGP-1,2,3) while they were opposite for the others (IGP-4,5) owing to varying trends in agricultural practices, precipitation, and humidity, which account for ammonia volatilization. The observed ammonia columns from the TES-Aura have also been compared with global emission inventories. The comparison has clearly indicated that satellite observations are underestimated as compared to ammonia emissions given by global emission inventories. It can be explained by the fact that ammonia owing to a short lifetime of few days is not fully observed by the TES observations with a revisit time of 16 days. Also, satellite observations averaged over larger areas due to coarse spatial resolution. Furthermore, satellite observations are largely impacted by the aerosol- and cloud-shielding effect [25, 26]. The correlation with fertilizer offtake data obtained from the National Fertilizer Development

Centre, Pakistan, yielded moderately reasonable correlation with satellite ammonia columns over the agriculture-intensive provinces of Punjab and Sindh in Pakistan. The results have provided with a substantial evidence for ammonia emissions related to agricultural activity in the study area for the observed time period. However, there is strong need to validate satellite observation of ammonia columns with ground-based ammonia measurements on a regular basis.

Data Availability

The data used to support the findings of this study are available from the corresponding author upon request.

Conflicts of Interest

The authors declare that there are no conflicts of interest regarding the publication of this paper.

Acknowledgments

This work was carried out as postgraduate research work at the NUST, Islamabad, Pakistan. The authors gratefully acknowledge the TES L2 data product, courtesy of the online Data Pool at the Atmospheric Science Data Center at NASA and the National Fertilizer Development Centre, Islamabad, Pakistan. The funding for this research work was provided by the NUST postgraduate research grant.

References

[1] N. Anderson, R. Strader, and C. Davidson, "Airborne reduced nitrogen: ammonia emissions from agriculture and other sources," *Environment International*, vol. 29, no. 2-3, pp. 277–286, 2003.

[2] P. Hobbs, *Introduction to Atmospheric Chemistry*, Cambridge University Press, Cambridge, UK, 2006.

[3] R. W. Pinder, A. B. Gilliland, and R. L. Dennis, "Environmental impact of atmospheric NH_3 emissions under present and future conditions in the eastern United States," *Geophysical Research Letters*, vol. 35, no. 12, 2008.

[4] J. G. M. Roelofs, A. J. Kempers, A. L. F. M. Houdijk, and J. Jansen, "The effect of air-borne ammonium sulphate on*Pinus nigra* var. *maritima* in the Netherlands," *Plant and Soil*, vol. 84, no. 1, pp. 45–56, 1985.

[5] R. Bobbink, D. Boxman, E. Fremstad, G. Heil, A. Houdijk, and J. Roelofs, "Critical loads for nitrogen eutrophication of terrestrial and wetland ecosystems based upon changes in vegetation and fauna [alpine heathlands, deposition]," *Critical Loads for Nitrogen*, vol. 41, pp. 111–159, 1992.

[6] S. N. Behera, M. Sharma, V. P. Aneja, and R. Balasubramanian, "Ammonia in the atmosphere: a review on emission sources, atmospheric chemistry and deposition on terrestrial bodies," *Environmental Science and Pollution Research*, vol. 20, no. 11, pp. 8092–8131, 2013.

[7] Y. Zhou, Y. Zhang, D. Tian, and Y. Mu, "Impact of dicyandiamide on emissions of nitrous oxide, nitric oxide and ammonia from agricultural field in the north China plain," *Journal of Environmental Sciences*, vol. 40, pp. 20–27, 2015.

[8] J. H. Seinfeld, "ES&T books: atmospheric chemistry and physics of air pollution," *Environmental Science & Technology*, vol. 20, no. 9, p. 863, 1986.

[9] M. Van Damme, L. Clarisse, C. L. Heald et al., "Global distributions, time series and error characterization of atmospheric ammonia (NH_3) from IASI satellite observations," *Atmospheric Chemistry and Physics*, vol. 14, no. 6, pp. 2905–2922, 2014.

[10] A. H. W. Beusen, A. F. Bouwman, P. S. C. Heuberger, G. Van Drecht, and K. W. Van Der Hoek, "Bottom-up uncertainty estimates of global ammonia emissions from global agricultural production systems," *Atmospheric Environment*, vol. 42, no. 24, pp. 6067–6077, 2008.

[11] M. A. Sutton, S. Reis, S. N. Riddick et al., "Towards a climate-dependent paradigm of ammonia emission and deposition," *Philosophical Transactions of the Royal Society B: Biological Sciences*, vol. 368, no. 1621, article 20130166, 2013.

[12] W. A. H. Asman, M. A. Sutton, and J. K. Schjorring, "Ammonia: emission, atmospheric transport and deposition," *New Phytologist*, vol. 139, no. 1, pp. 27–48, 1998.

[13] K. B. Beem, S. Raja, F. M. Schwandner et al., "Deposition of reactive nitrogen during the rocky mountain airborne nitrogen and sulfur (RoMANS) study," *Environmental Pollution*, vol. 158, no. 3, pp. 862–872, 2010.

[14] F. Paulot, D. J. Jacob, and D. K. Henze, "Sources and processes contributing to nitrogen deposition: an adjoint model analysis applied to biodiversity hotspots worldwide," *Environmental Science & Technology*, vol. 47, no. 7, pp. 3226–3233, 2013.

[15] C. A. Pope III, "Epidemiology of fine particulate air pollution and human health: biologic mechanisms and who's at risk?," *Environmental Health Perspectives*, vol. 108, no. 4, pp. 713–723, 2000.

[16] J. P. Martin and H. D. Chapman, "Volatilization of ammonia from surface-fertilized soils," *Soil Science*, vol. 71, no. 1, pp. 25–34, 1951.

[17] J.-W. Erisman, A. W. M. Vermetten, W. A. H. Asman, A. Waijers-Ijpelaan, and J. Slanina, "Vertical distribution of gases and aerosols: the behaviour of ammonia and related components in the lower atmosphere," *Atmospheric Environment (1967)*, vol. 22, no. 6, pp. 1153–1160, 1988.

[18] R. Beer, M. W. Shephard, S. S. Kulawik et al., "First satellite observations of lower tropospheric ammonia and methanol," *Geophysical Research Letters*, vol. 35, no. 9, 2008.

[19] L. Clarisse, C. Clerbaux, F. Dentener, D. Hurtmans, and P.-F. Coheur, "Global ammonia distribution derived from infrared satellite observations," *Nature Geoscience*, vol. 2, no. 7, pp. 479–483, 2009.

[20] R. Beer, "TES on the aura mission: scientific objectives, measurements, and analysis overview," *IEEE Transactions on Geoscience and Remote Sensing*, vol. 44, no. 5, pp. 1102–1105, 2006.

[21] M. W. Shephard, K. E. Cady-Pereira, M. Luo et al., "TES ammonia retrieval strategy and global observations of the spatial and seasonal variability of ammonia," *Atmospheric Chemistry and Physics*, vol. 11, no. 20, pp. 10743–10763, 2011.

[22] L. Clarisse, M. W. Shephard, F. Dentener et al., "Satellite monitoring of ammonia: a case study of the San Joaquin valley," *Journal of Geophysical Research: Atmospheres*, vol. 115, no. D13, 2010.

[23] A. K. Koshal, "Changing current scenario of rice-wheat system in Indo-Gangetic plain region of India," *International Journal of Scientific and Research Publications*, vol. 4, no. 3, pp. 1–13, 2014.

[24] H. M. Worden, M. N. Deeter, C. Frankenberg et al., "Decadal record of satellite carbon monoxide observations," *Atmospheric Chemistry and Physics*, vol. 13, no. 2, pp. 837–850, 2013.

[25] R. S. Narang and S. M. Virmani, "Rice-wheat cropping systems of the Indo-Gangetic plain of India," No. REP-8944, CIMMYT, Texcoco, Mexico, 2001.

[26] H. Pathak, J. K. Ladha, P. K. Aggarwal et al., "Trends of climatic potential and on-farm yields of rice and wheat in the Indo-Gangetic plains," *Field Crops Research*, vol. 80, no. 3, pp. 223–234, 2003.